Dissertation
submitted to the
Combined Faculties for Natural Science and Mathematics
of the Ruperto-Carola University of Heidelberg, Germany
for the degree of
Doctor of Natural Sciences

Put forward by
Diplom-Physikerin: Nadine Walter
Born in: Rodewisch

Oral examination: 05.02.2010

A Cell Mechanical Study on Adherent and Suspended Pancreatic Cancer Cells using AFM and Microfluidics

Referees: Prof. Dr. Joachim Spatz
Prof. Dr. Heinz Horner

A Cell Mechanical Study on Adherent and Suspended Pancreatic Cancer Cells using AFM and Microfluidics

Cell mechanical responses are important in the context of physiologically relevant deformations and stresses that cells have to sustain inside the body. The cell material response to quasistatic and localized deformations, similar to those during active cell migration, is studied in the first part of this thesis. Living adherent pancreatic cells and their extracted subcellular keratin network were probed using Atomic Force Microscopy (AFM) indentation testing in order to determine if there is a significant mechanical contribution of the keratin network to living cell mechanics. It was found that the extracted keratin network elastic modulus was only 2 to 5% of the living cell elastic modulus. No correlation of elastic moduli and keratin mesh densities was detected for living cells, whereas a huge cell-to-cell variation in the elastic moduli was present. Deformations mimicking those a cell may be subjected to during passive transport in the blood vessel system were studied in the second part of this thesis. Here, the dynamics of the same cells, but in a suspended state, was observed at high deformation rates and on a whole cell level during their transit through a microfluidic channel restriction. A novel cantilever-based method (microflap) was incorporated in the microrestrictions of a flow cell chip. For the first time, the cell mechanical response was assessed directly, and indepent of applied flow and frictional resistance, while the cell was squeezed through a microchannel restriction. Using the approximation of a uniformly loaded cantilever, the total force and the pressure exerted on the microflap by the cell can be calculated from the flap deflections.

Messung von mechanischen Eigenschaften von Pancreaskrebszellen im adhärenten und nicht adhärenten Zustand unter Benutzung von RKM und Mikrofluidik

Im Körper müssen lebende Zellen physiologischen Deformationen und Kräften widerstehen. Beispiele hierfür sind die aktive Zellmigration im Gewebe und der passive Zelltransport im Gefäßsystem. Zellmechanische Eigenschaften sind bei diesen Prozessen bestimmend. Im ersten Teil der vorliegenden Arbeit werden die mechanischen Eigenschaften von lebenden adhärenten Pancreaskrebszellen und von deren extrahierten Keratinnetzwerken bei quasistatischer und lokaler Deformation mit Hilfe des Rasterkraftmikroskops (RKM) untersucht, was der Deformationsdynamik aktiver Zellmigration nahekommt. Das Ziel war es, den Einfluß des Keratinnetzwerkes auf die gesamte Zellmechanik zu testen. Die Ergebnisse zeigen, dass der Elastizitätsmodul des Keratinnetzwerkes nur etwa 2 bis 5% dessen der lebenden Zellen beträgt. Weiterhin konnte keine Korrelation zwischen Keratinnetzwerkdichte und Elastizität bei lebenden Zellen nachgewiesen werden, wohingegen eine erhebliche Variation der Elastizitätsmodule zwischen den Zellen auftrat. In einem zweiten Teil wird die Deformationsdynamik derselben Zellen, jedoch nun in einem nicht adhärenten Zustand, bei schneller und globaler Deformation betrachtet. Dies ähnelt der Deformationsdynamik von Zellen z.B. im Blutkreislauf. Die Deformation von nicht adhärenten runden Zellen wurde in Mikrokanälen untersucht. Hierfür wurde ein biegbarer Mikrobalken als Deformationssensor in eine Mikroverengung eines Mikrofluidik Aufbaus eingearbeitet. Mit dieser neuen Herangehensweise ist es möglich den Deformationswiderstand von Zellen direkt und ohne Einfluss von Reibungs- oder Druckkraft zu messen, während die Zellen durch eine Mikroverengung gedrückt werden. Unter der Annahme, dass die Zellen einen gleichverteilten Druck auf die Fläche des Kraftsensors ausüben, können die gesamte Kraft und der Druck aus der Auslenkung des Mikrobalkens berechnet werden.

Contents

Preface

Inside the body living cells have to sustain physiologically relevant deformations and stresses. Thus, in the field of cell mechanics, it is aimed to measure material constants or, in general, to describe the cell and its subcellular components with a material model [Ana06]. It is sought to understand to what extent individual cellular components contribute to the overall cell responses and under which circumstances. Of recent interest are alterations of cellular components due to diseases, which change cell mechanics [Sur07]. The knowledge of how alterations are contributing can first help to understand disease conditions and, second, might provide a tool for disease diagnostics. Zooming in on this very general picture of cell mechanics, the main focus of this thesis is the mechanical response of pancreatic cancer cells in connection with deformations during cancer metastasis.

This thesis is divided into three main parts with its subchapters. Each subchapter has an introduction in order to position the contents within the whole framework of this thesis. Part I introduces the basic knowledge on living cells in general and on the pancreatic cancer cell system that was studied here as well as how cells might be deformed during the process of cancer metastasis. In Part II indentation testing on living adherent cells and their extracted subcellular keratin intermediate filament networks using Atomic Force Microscopy (AFM) is presented and the applied methodology with the theoretical background is introduced. The role of the keratin intermediate filament network density (see figure 1) inside pancreatic cancer cells was studied, as it was suggested to be involved in controlling cell mechanics and thus cell migration during cancer metastasis. Additionally, the mechanics of intermediate filaments and intermediate filament networks, in general, is not yet completely understood, in contrast to the better studied actin network. In Part III of this thesis cell mechanical testing with the help of microfluidics is described. A novel method for assessing cell mechanics of suspended cells in microchannel restrictions is presented (see figure 2). The behavior of suspended pancreatic cells is investigated due to the fact that tumor cells, that circulate in the vessel system, are less well examined than in the adherent state. A conclusion section summarizes the results of this thesis and gives an outlook for further projects arising from this work.

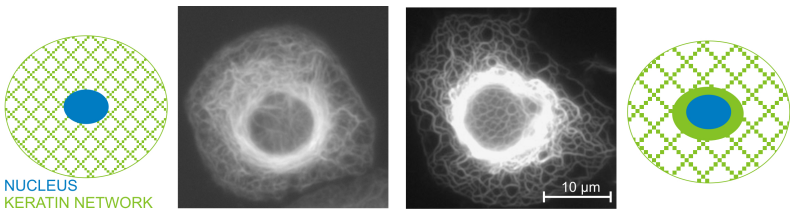

Figure 1: Part II - Indenting Adherent Cells with the Atomic Force Microscope.

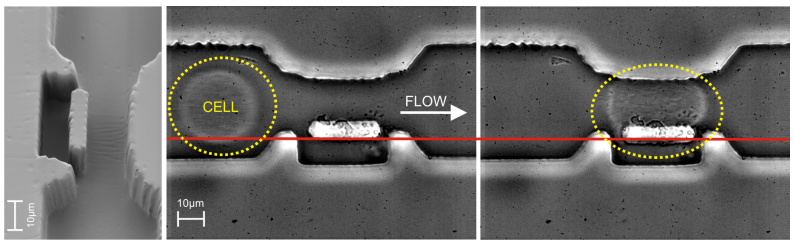

Figure 2: Part III - Compression of Suspended Cells inside Microchannels.

Part I

Living Cells and Cell Mechanics

Chapter 1

Biological Cells as a Material

1.1 Introduction

In this chapter, a basic introduction to living cells and their substructures is presented. A brief overview on subcelluar network and cell mechanical properties is given, including material models and probing techniques. An emphasis is given to the intermediate filaments, as the mechanical properties of the keratin intermediate filament network of pancreatic cancer cells and its contribution to whole cell mechanics are the interest of this thesis.

1.2 The Cell and its Substructures

1.2.1 Eukaryotic Cells

A cell is the smallest living unit of all life. It can reproduce itself and react to its environment. Together with the extracellular matrix, cells form tissues, organs and whole organisms, where functional diversity and highly complex control mechanisms are required on the cell and subcellular level. [Alb02]

All eukaryotic cell types of animals and humans have a similar heterogenous structure, but

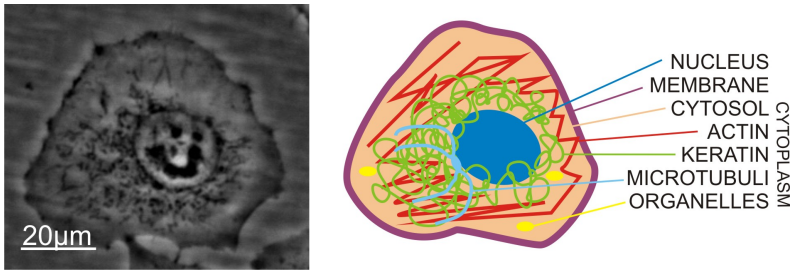

Figure 1.1: Phase contrast image of a living pancreatic cancer cell and a sketch of the cell with its subcellular components. The cell consists of the enclosing membrane, the nuclues containing the genetic information and the cytoplasm which has a variety of functions from energy metabolism to being the mechanical backbone.

differ in amount and composition of subcomponents based on cell function. Cell components can be summarized as nucleus, membrane and cytoplasm. The term cytoplasm comprises the cytoskeleton, the aqueous cytosol , the cell organelles and a pool of solute proteins (see figure 1.1). [Alb02]

The cell membrane, a 4 nm thick lipid bilayer, encloses all the cell contents, while the nucleus contains and protects the genetic information. The nucleus has approximately $1/3$ of the cells linear dimension, where cells can vary from 20 to 100 μm in size. Specialized cell organelles are responsible for different tasks as, for example, mitochondria for energy metabolism and ribosomes for protein synthesis. [Alb02]

The cytoskeleton is the filamentous system inside the cell and it is the main mechanical apparatus for processes such as cell migration, organelle transport, cell divison and maintaining the cell shape. The cytoskeleton is composed of different types of interwined biopolymers and their accessory proteins, which serve as a connection for intra and extracellular signalling. Every eukaryotic cell posseses an actin and a microtuble network. Microtubules are involved in directed intracellular transportation, organelle positioning, and, during cell divison, microtubules form the mitotic spindle. Actin filaments are important force transducers during cell migration. [Alb02]

A third type of fiber, the intermediate filaments, comprise a group of different filament types (e.g. keratin, vimentin, desmin), which are cell-type specific. Much less is known about intermediate filament assembly and function. Unlike actin fibers and microtubuli, intermediate filaments are non polar structures and thus there is no motor protein transport along them. The main interest of this work is the keratin intermediate filament network inside pancreatic cancer cells (see chapter 2.2). This type of intermediate filament is mainly found in epithelial cell lines and has structural as well as regulatory functions which are not yet completely understood. [Mag07, Alb02]

1.2.2 Adherent vs. Suspended Cells

Other than in the tissue of the body, where the cells are embedded in a 3D environment, in a biology lab, cells are cultured in 2D. Adherent cells then attach and spread onto the flat surface of a cell culture flask. The shape of the cytoskeleton of the cells in the adhesive state is triggered through external signals such as surface ligands and surface hardness. When adherent cells detach from a surface they round up and float in the surrounding medium. In this unnatural suspended state, their cytoskeleton is less pronounced (see figure 1.2). For example, the actin cortex of the cell is still present, but the actin stress fibers are only seen in the adherent state. In general, the cytoskeleton structure of suspended cells has been not studied very intensively so far. The main reason for this is probably, that important cell functions and regulation processes, such as cell division, are triggered, among other signals, through surface specific attachment and thus studied in the adherent state. However, for e.g. metastasizing tumor cells, the suspended cell mechanical behavior is of interest (see section 2.3).

Other cell types have no physiological need to adhere in the body as, for example, blood cells. These cell types are so-called suspension or circulating cells.

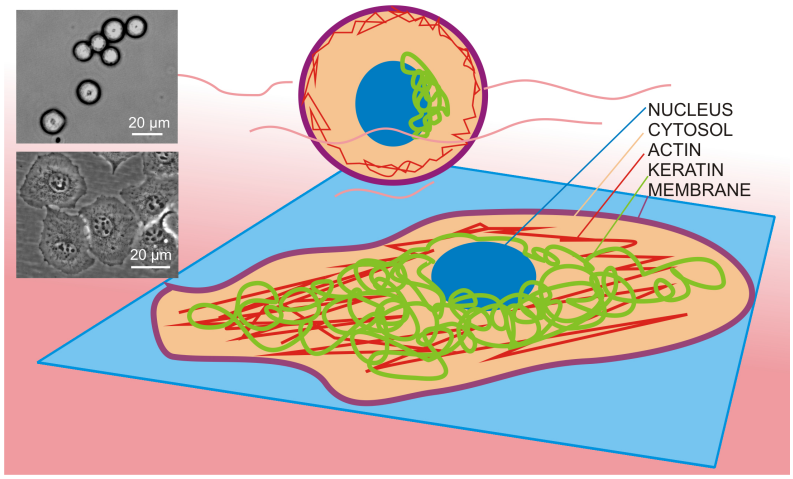

Figure 1.2: Sketch of a suspended vs. an adherent cell and phase contrast images of adherent and suspended pancreatic cancer cells. Cell shape and cytoskeletal morphology differ between suspended and adherent cells.

1.3 Cell- and Subcellular Network Materials Properties

1.3.1 From Single Fibers to Networks

The material response of a cell originates from cellular substructures, which is mainly the cytoskeleton [Kas07]. The fiber networks inside the cell are made up of cross-linked and bundled single fibers of actin, microtubuli and intermediate filaments. Associated proteins connect fibers of the same or different type, as e.g. the cytolinker plectin and the keratin bunbdling protein filaggrin. [Mag07, Fu98, Oma04]

Single fiber properties such as thickness and bending stiffness (B)[1] of actin, microtubuli and intermediate filaments are known. Microtubules are the thickest and straightest fibers inside the cell, with a diameter of 25 nm and a bending stiffness of 2.6 x10^{-23} N/m^2. Actin filaments have a diameter of 8 nm and a bending stiffness of 7 x10^{-26} N/m^2. Intermediate filaments have a diameter of about 10 nm and the lowest bending stiffness of only 4 to 12 x10^{-27} N/m^2. [Sur07]

Fiber network properties arise from single fiber properties as well as their structural assembly. As direct in vivo measurements of network properties are corrupted by other cellular structures, properties of biomimetic filament suspensions have been investigated. Actin networks have a higher rigidity than intermediate filaments, but fluidize at high strains [Jan91]. In contrast, intermediate filaments networks exhibit strain hardening at high tensile strain without rupture [Jan91, Kre07]. The reason for this different behaviour is hypothesized to be the structural difference of the monomer and dimer assembly of actin and also microtubule formation and the weak, non-covalent, coiled-coil dimers assembly of intermediate filaments, that might allow sliding of intermediate filament fibers. For keratin intermediate filament suspensions, it was found that the bulk elasticity is dependent on polymer concentration as well as polymer size, which is in agreement with semiflexible polymer physics. The keratin network exhibited only a weak time

[1] B = EI$_A$. The bending stiffness (B [Nm^2]) is defined as the product of elastic modulus (E) and geometrical moment of inertia (I$_A$). It describes the resistance of the fibers to bend if a torque is applied.

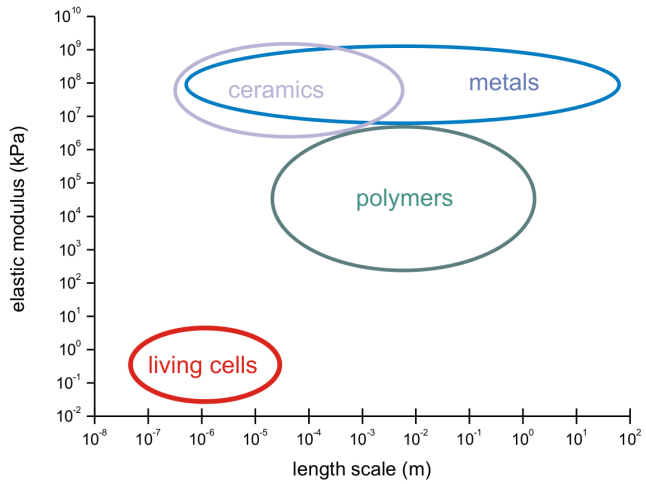

Figure 1.3: Elastic moduli and length scales of different materials. Adopted from [Bao03]. Living cells are very soft and small compared to most engineered materials.

dependency. [Yam03]

Further, the storage modulus of the in-situ keratin intermediate filament network extracted from alveolar epithelial cells has been measured with microrheological particle tracking. It was also shown, that the storage modulus increased with network density. Measurements at 1Hz yielded storage modulus values ranging from 95 to 335 dyn/cm^2, which translates into an elastic modulus of 30 to 110 Pa assuming a Poisson ratio of 0.5. The materials response was found to be again mainly elastic. [Siv08]

1.3.2 Living Cell Material Properties

A simple and first approximation is to see the cell as a linear elastic material with a characteristic elastic modulus [Cro07, Li08]. Compared to engineered materials of every day life, cells are very soft and small. While metals have an elastic modulus of 1x10^9 kPa and polymers 1x10^5 kPa, cells are in the range of 1 kPa (see figure 1.3).

Several other material models are used to characterize the cell mechanical behavior. A variety of linear viscoelastic models describe the cell as combination of springs and dashpots in order to account for elastic and viscous contributions [Dar07]. However, it has also been shown that cells obey a power law [Des05], suggesting a distribution of relaxation times and not only one characteristic time as for the linear viscoelstic models. Further, the cell can be described from the microstructural point of view, as a poroelastic material [Gal08, Ros08], an open cell foam network or a presstressed cable network [Ana06]. And, obviously, the cell can be also seen as a composite of different materials, instead of one material. However, analytical solutions are not available for all models and available testing methods. Furthermore, cells show outstanding behaviors such as fluidization upon mechanical stretching, which is due to actin fluidization [Tre07]. Thus the question arises, if the cell mechanical response can be discribed with just one universal model. It might be rather an assembly of behaviors due to the cellular substructures and the physiological

condition.

As a cell is a highly complex object, it is difficult to determine which subcellular component mainly contributes to the overall mechanical response in living cells. In order to sort out the relative importance of each, either specific drugs have been applied that disassemble or prevent the assembly of a fiber type; or genetic alteration have been introduced in cells. It has been shown that drug assisted disruption of actin stress fibers clearly softens the cell and also that actin fibers can be distinguished mechanically when scanning the living cell [Rot00, Cos06]. Further, vimentin deficient fibroblast showed a signifant mechanical difference to wildtype fibroblasts [Wan00].

Other interesting findings are disease connected alteration in the cytoskeleton, showing mechanically differences accordingly. For example, there are several publications that show a decrease in mechanical stability for cancerous cells in the adherent as well as in the suspended state [Sur07, Li08, Cro07, Guc05, Hou09]. In most cases, this has been found to be also associated with the actin filament network. Further, intermediate filament mutations are known to lead to functional disorders [Fu98].

1.3.3 Cell Mechanics Probing Techniques

As already discussed a cell is a very soft and small object compared to most engineered materials. Testing methods in a sufficient force and spacial resolution are therefore necessary. There are a variety of cell mechanical testing methods [VanV03, Bao03], that can be divided into local and global, as well as being suitable for adherent or suspended and suspension (circulating) cells (see figure 1.4). Additionally, theoretical models need to be available to extract meaningful information as material constants from the experimental techniques. For completeness, every probing technique introduces artifacts, which distort the results. Further, the physiological relevance in terms of timescales and length scales should be addressed correctly.

In this thesis, the Atomic Force Microscope (AFM) is applied for local adherent cell indentation testing (see Part II). Further, microchannel restrictions are applied and a novel direct method for suspended cell mechanics testing inside a microchannel restriction is developed (see Part III).

The AFM is a versatile tool because the cantilever force sensor as well as tip size can be adjusted for spacial and force resolution requirements. It can be used for compression as well as stretching and shearing tests. Further, it is a commercially available device and thus profiting from accumulated research and development compared to other mainly custom built biomechanics testing equipment. Thus, a vast variety of applications for the AFM in the field of cell and subcellular biophysics has appeared. It is used for e.g. manipulating and quantifying DNA unfolding, single cell detachment from surfaces or other cells, as well as a nanoindentation device for cells, bacteria or viruses. [But05]

Microchannel restrictions (see figure 1.4) are a tool for studying cell deformation and mimicking blood vessels. Thus, preferrably, blood cells were investigated. Further, indirect mechanical comparative studies are performed by comparing channel transit and deformation times of blood and also of noncirculating cells [Hou09, Ros08b, Gab09, Sur05].

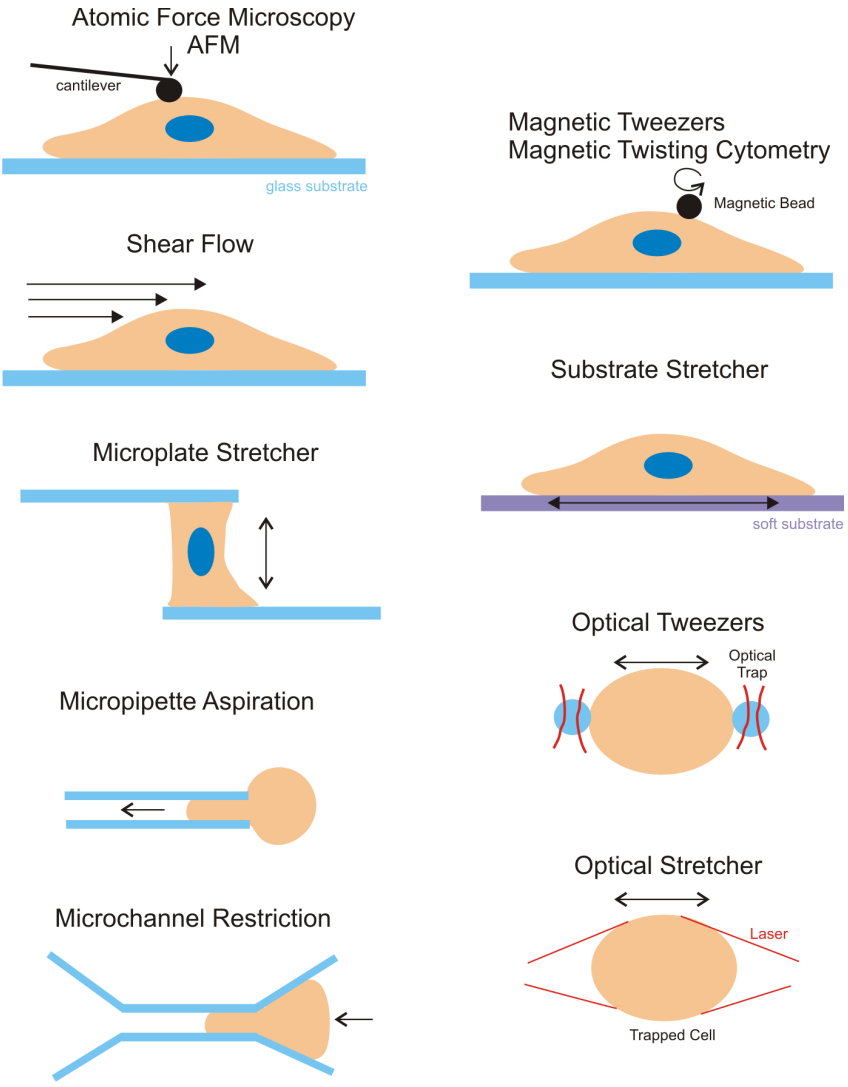

Figure 1.4: Sketch of cell probing methods. Adopted from [Sur07].

Chapter 2

Pancreatic Cancer Cells and Metastasis

2.1 Introduction

In this chapter, the cell system of pancreatic cancer cells (Panc-1) used in this thesis is introduced. Special emphasis is given on their keratin intermediate filament network, as its impact on the local cell mechanics is of interest in this thesis. The hypothesis that facilitated cell migration is connected to a lower resistance to deformation originating from a sparse keratin network, is presented. Further, the process of cancer metastasis is described and it is discussed how the altered mechanical properties of the cell might facilitate this process in connection with active migration and passive transportation of the cell.

2.2 Pancreatic Cancer Cells and their Keratin Intermediate Filament Network

Pancreatic cancer cells (Panc-1) are epithelial cells from a pancreatic tumor [Lie75]. These cells have a large spreading area and a well-developed keratin intermediate filament network and thus serve as a model system to study keratin regulation and reorganisation mechanisms.

Actin filaments and microtubuli are present in all eukaryotic cells. In simple epithelia, as in Panc-1 cells, keratin filament networks are found additionally. Keratin 8 (K8) and keratin 18 (K18), a TypI and a TypII keratin respectively, are expressed specifically and aggregate as a heteropolymer. The smallest structural unit of keratin filaments are polar coiled-coil dimers from K8 and K18 strands that form a keratin chain. Protofilaments are made up of two antiparallel chains, two protofilaments then form a protofibril and finally 3 to 4 protofibrils constitute a keratin fiber of 10 nm diameter (see figure 2.1). The keratin fibers bundle and crosslink further and form an almost homogenous network throughout the cell [Fu98]. Hereby, kertin bundling proteins, as e.g. fillagrins, organize keratin filaments in macrofibrillar arrays [Oma04]. The exact mechanisms of the intermediate filament network assembly dynamics, in general, are still controversial [Mag07, Vik92, Win04].

However, it has been shown that the keratin network structure is reorganized by treatment with the bioactive lipid Sphingosylphosphorylcholin (SPC). The keratin fibers rearrange from an al-

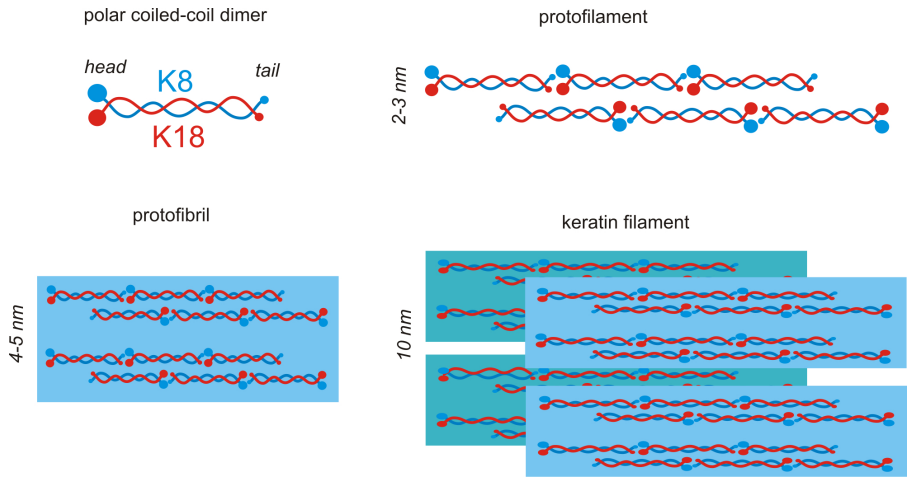

Figure 2.1: Structure of keratin intermediate filaments in epithelial cells. Polar coiled-coil dimers from K8 and K18 monomers form a chain, protofilaments are made up of two antiparallel chains, two protofilaments again form a protofibril and finally 3 to 4 protofibrils constitute a keratin fiber of 10 nm diameter.

most homogenous distribution to a dense network around the nucleus and a sparse network in the cell periphery. Additionally, the SPC treatment induced an enhanced cell migration behavior. Further, a mechanical softening effect of the a Panc-1 cell after SPC treatment was observed in a microplate stretching experiment on a whole cell level. It was concluded from this series of experiments that the keratin network determines the main cell mechanical resistance to deformation. [Bei04, Mic04]

Further work on the Panc-1 cell system did clarify the underlying mechanisms of the keratin network reorganisation. The main mechanism for posttranslational keratin regulation is phosphorylation. It was found that a phosphorylation of the K8-Ser^{431} site at the K8 strand of the keratin coiled-coil dimer is sufficient for keratin reorganisation. A transient transfection, which mimicks the SPC keratin phenotype (named K8SE/K8WT) and fluorescently labels the keratin network, has been developed as depicted in figure 2.2. Furthermore, it was shown that such keratin altered Panc-1 cells migrate faster in a 2D cell culture environment as well as they have an enhanced ability to go through a porous membrane in a Boyden chamber assay. [Bus08]

The interest of this thesis lies in the localized cell- and keratin mechanical properties. The new developed transient transfection with fluorescently labelled keratin networks inside living cells allows for colocalisation of mechanical properties and keratin network density. It is sought to clarify the mechanical importance of the keratin network density inside Panc-1 cells during slow deformation as in cell migration.

2.3 The Process of Tumor Metastasis and the Importance of Cell Mechanics

The stage of tumor metastasis in cancer patients mainly determines their possibility for cure. A highly spread tumor invades healthy tissue until functionality of important vital organs are no longer intact. In general, cancer metastasis is a highly complex process and not yet fully

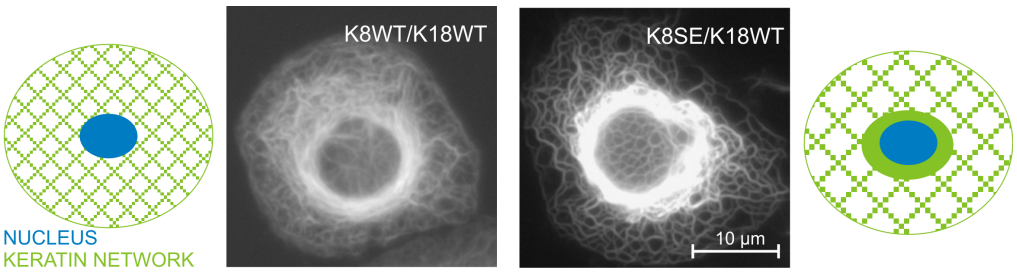

Figure 2.2: Fluorescence labelled keratin intermediate filament network inside Panc-1 cells and sketch thereof. K8SE/K18WT names the SPC treatment mimicking transfected Panc-1 cells, where the keratin network is dense around the nucleus and less dense in the cell periphery. K8WT/K18WT names the wildtype reference transfected Panc-1 cells with a homogenous keratin network throughout the cell.

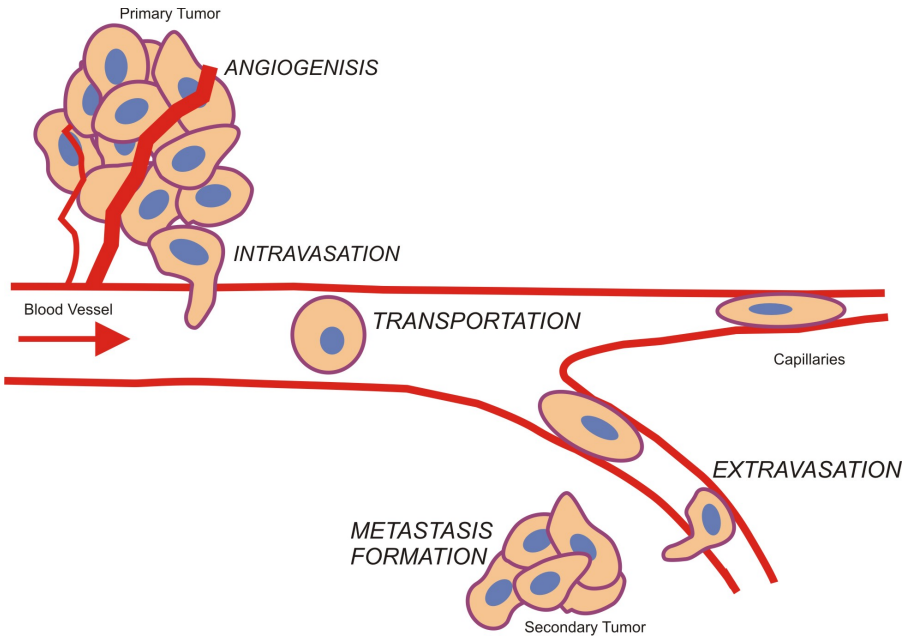

Figure 2.3: Sketch of the cancer metastasis process inside the body. The cells need to deform during active migration from the primary tumor into the vessel system. After passive transportation, the cells get stuck in narrow capillaries. From there, cells migrate into the tissue to form secondary tumors.

understood. Here, only the aspect of cell mechanical responses in connection with metastasis are focussed on.

In tumor metastasis (see figure 2.3), cancerous cells of the primary tumor migrate through the surrounding tissue in an abnormal and aggressive way by actively dissolving extracellular matrix (intravasation) until they reach vessels of the blood or lymphatic system. Through the transport and circulation systems, which are primarily responsible for transporting nutrients and oxygen via blood cells, the tumor cells are shipped throughout the body. Further, it is thought that the cells then get stuck in small capillaries. In vivo capillaries are 5-10 μm wide [Ros08b], which is smaller than the diameter of most suspended cells. From there the cells migrate into the tissue (extravasation) and grow secondary tumors in an uncontrolled manner and even induce growth of new blood vessels for nutrient supply (angiogenesis). [Woo97, Kum09, Gas08]

Material responses play a role in the metastasis process when cells are deformed. Active cell deformations occur during migration through tissue and, second, when cells are squeezed as they are passively transported through narrow vessels.

Part II

Indenting Adherent Cells with the Atomic Force Microscope

Chapter 3

The Atomic Force Microscope (AFM) as an Indentation Tool

3.1 Introduction

In this chapter, the Atomic Force Microscope (AFM) as a tool for indentation testing is presented. The AFM is used in this thesis to locally deform living cells, while recording the applied force and deformation in order to draw conclusions about the cell material properties. In materials science, this is referred to as indentation testing. Submicrometer spacial resolution and piconewton force sensitivity make the AFM a suitable tool for probing living cells. Conventional material indentation testing is performed on a macroscopic length scale (mm-cm) with coarser force resolution (nN-mN) and can not be applied to such small and soft biological objects.

In the following sections, the necessary background knowledge on the AFM basic working principle and the used set-up is given. Data acquisition and processing into force-indentation curves is presented. Indentation parameters are discussed. Height measurements with AFM and force-relaxation curves are introduced.

3.2 AFM Principle and Set-up

The AFM was invented in the 1980's by Binnig and Quate [Bin86]. It is based on detecting pN to μN interaction forces on a nm scale contact area via a cantilever spring. Thus, sensing the surface at high spatial resolution is possible. The preceeding Scanning Tunneling Microscope (STM) [Bin82] measured tunnel currents on surfaces with high spatial resolution but had the limitation of being only suitable for conductive materials. The AFM, as well as the STM, can overcome optical resolution limits and, therefore, are widely used for imaging surface topograhies, e.g., for resolving nm scale objcects or even single atoms.

The force sensor in an AFM system is a micrometer scale beam, the cantilever. For small deflections, the cantilever behaves as a linear spring. Thus, with a known cantilever spring constant, an absolute force can be measured (see equation 3.3). Attached to the cantilever is a tip which is directly interacting with the surface. The spatial resolution of the AFM is dependent on tip size and the resulting contact area, height and force resolution are dependent on the cantilever

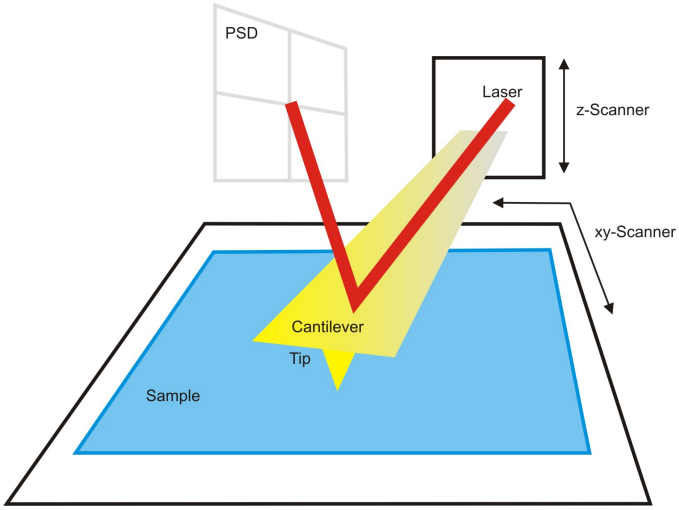

Figure 3.1: Schematics of the AFM set-up. The cantilever serves as the force senor. A laser and a position sensitive diode (PSD) is used for monitoring cantilever deflections. In-plane and vertical scanners are actuated by piezo elements.

spring constant and thermal, acoustic or vibrational noise levels. In the AFM device[1] used for this work , deflection sensing is solved with a laser that reflects off the cantilever back side and is detected with a position-sensitive diode (PSD). There, the change in reflection angle is assessed via a voltage change. For absolute force measurements the system detection sensitivity (see equation 3.2) needs to be calibrated. The cantilever is actuated in the vertical direction (z-scanner, 18 μm range) with a piezoelectric element. A nanopositioning sensor detects the exact piezo movement and corrects for piezo hysteresis and nonlinearities in closed loop mode. The in-plane movement of the the xy-scanners (90x90 μm range) is incorporated in the base plate and decoupled from the vertical scanner. A sketch of the AFM set-up is shown in figure 3.1.

During acquisition of a force-distance curve, the vertical movement and deflection of the cantilever is recorded in non contact and contact regime. In the case of a surface topography scan, a feedback loop adjusts the vertical displacement while the cantilever is moved over the surface in xy direction in contact or non-contact mode, where the vertical movement contains the height information.

Some additional features of the equipment enable work with living cells. A fluid cell with a heater[2] is used, which allows for a liquid environment and a controlled temperature. The AFM sits on an optical microscope[3], equipped with a camera[4] for performing fluorescence and bright-field imaging. A coarse xy-positioning system enables movement of the sample within a 3x3 mm area, while the xy-scanner can be controlled manually with nanometer precision.

[1] MFP-3D-BIO, Asylum Research
[2] Bio Heater Closed Fluid Cell, Asylum Research
[3] X71,Olympus
[4] AxioCam Mrm, Zeiss

3.3 Force Indentation Curves

3.3.1 Data Conversion to Force Indentation Curves

Each recorded force distance curve consists of an approach and a retract part. The cantilever is driven towards the surface with a constant velocity until it is in contact with the surface. It further deflects while the sample is indented until a trigger force is reached. In the retraction part, the cantilever is actuated in reverse. Optionally, a dwell time at the maximum force can be introduced, to measure force relaxation behavior (see section 4.4). In the following, only the approach data will be used and transferred from raw data into force-indentation curves (see figure 3.2). Force-indentation curves are later used for material model fitting (see chapters 4 and 5).

Cantilever deflection voltage (U[N/m^2]), and the z-scanner vertical movement (Z[m]) are recorded. In order to calibrate the optical detection system and to convert U to the real deflection (D[m])(see equation 3.1), the system detection sensitivity (S[m/V]), needs to be determined.

$$D = S \cdot U \tag{3.1}$$

For this, a force-distance curve is acquired on a hard reference substrate. At contact, the vertical movement and the cantilever deflection are equal quantities because of no sample deformation. Hence, the inverse slope in the linear regime of the U-Z curve at contact, is equal to S (see equation 3.2).

$$S = \left[\frac{dU}{dZ}\right]^{-1}_{contact} \tag{3.2}$$

The sensitivity is checked several times during the course of experiments under the exact experimental conditions. The sensitivity is dependent on several parameters, as for example the refractive index of the used medium [Liu08], and can change over time. Further, it is verified, that the sensitivity is constant up to the maximum used cantilever deflection. System compliance, resulting in a non linear sensitivity, introduces artifacts. All force curves are further corrected for the virtual deflection. The virtual deflection occurs because the piezo movement is coupled to deflection detection[5]. However, this is a linear dependency, which is corrected with a linear fit to the approach curve in the non-contact regime (see figure 3.2). The point of contact, also called approach point, on the surface, where the indentation is defined as zero, is chosen manually during the otherwise automated curve correction procedure by a customized Matlab routine (The Mathworks Inc.). Finally, with a known cantilever spring constant (K[N/m]) (see section 3.3.2) and the cantilever deflection, the force (F[N]), that the cantilever exerts on the sample at contact is calculated by using Hooke's Law (see equation 3.3).

$$F = K \cdot D \tag{3.3}$$

The indentation depth (I[m]), into a soft sample is given by the difference of vertical movement and cantilever deflection (see equation 3.4).

$$I = Z - D \tag{3.4}$$

3.3.2 Cantilever Properties and Spring Constant Calibration

The cantilever properties as the spring constant, the resonant frequency, cantilever shape and tip geometry have to be carefully chosen for sufficient force resolution and performance.

[5] information from Asylum Research

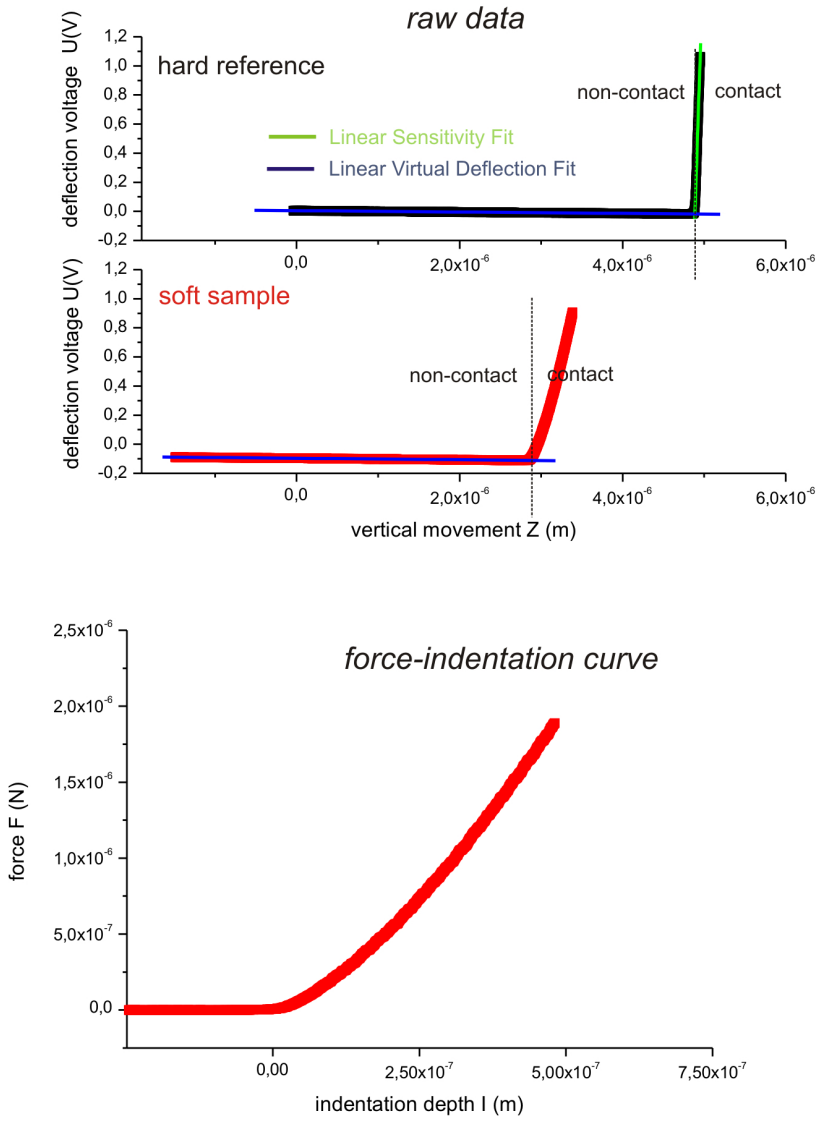

Figure 3.2: Conversion from raw data to a force indentation curve. The raw data of a force-distance curve on a hard reference surface are used for extracting the system detection sensitivity. After correcting the sample force-distance curves for virtual deflection and choosing the contact point, the data are transformed into force-indentation curves (see equautions 3.1 to 3.4).

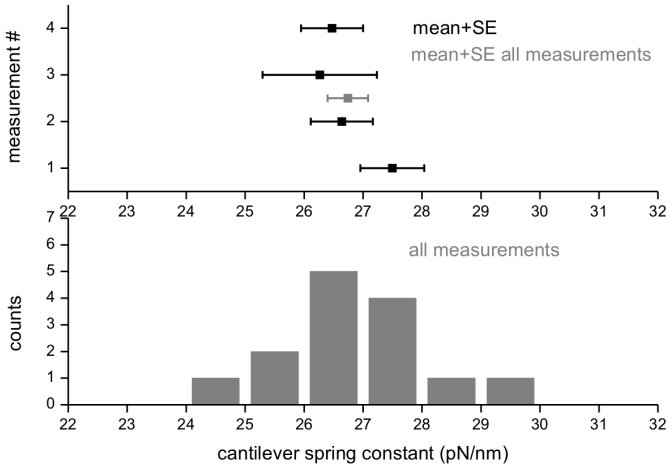

Figure 3.3: Cantilever calibration data and SEM images of utilized cantilevers. (a)Spring constant measurements of a v-shaped cantilever using the thermal noise method during four days of consecutive experiments.

In this thesis, soft tipless v-shaped cantilevers[6] (see figure 3.4 a) with a nominal spring constant of 0.02 N/m and a resonant frequency of 10 kHz are used for indenting living cells (see chapter 5). Tipless cantilevers further allow easy attachment of spheres to the cantilever end for a spherical indenter geometry. For Polydimethylsiloxane (PDMS) indentation testing (see chapter 4), rectangular cantilevers[7](see figure 3.4 b) with and without a tip, with spring constants ranging from 2 to 30 N/m and resonant frequencies from 100 to 300 kHz, are employed .

Spring constant calibrations of all cantilevers are performed with the AFM built-in thermal noise method [Hut93,But95,Pro09b]. The thermally driven deflection of the free cantilever is recorded at room temperature in air. Via the equipartition theorem, the first flexural mode of the cantilever and the cantilever spring constant are related. The AFM manufacturer[8] expects the absolute uncertainties of this method to be less than 20%.

Figure 3.3 shows four independent spring constant measurements of the same v-shaped cantilever during four days of consecutive experiments as well as a histogram of all measurements. A normal distribution with a standard error of 2% and no systematic deviation is observed. Thus, errors for cantilever spring constants, determined by thermal noise method, are estimated by the standard error and a 5% systematic deviation from the cantilever tilt [Hei04,Hut05]. However, controversial opinions on v- shaped cantilever calibration with the thermal noise method are found in literature. It has been reported that v-shaped cantilevers suffer a systematic deviation compared to rectangular cantilevers [Sta01], while others reported good suitability for the thermal noise method [Lev02]. Experimental proof is difficult due to high deviations between different cantilever calibration methods [Bur02]. Hence, only when employing the same type of cantilever and calibration method, the standard error can be applied.

In the case of high resonant frequencies, the thermal noise method is not applicable and a ref-

[6]PNP-TR-TL-Au, Nano and More GmbH
[7]TL-FM,Nano and More GmbH; ACTA, JPK Instruments
[8]Asylum Research

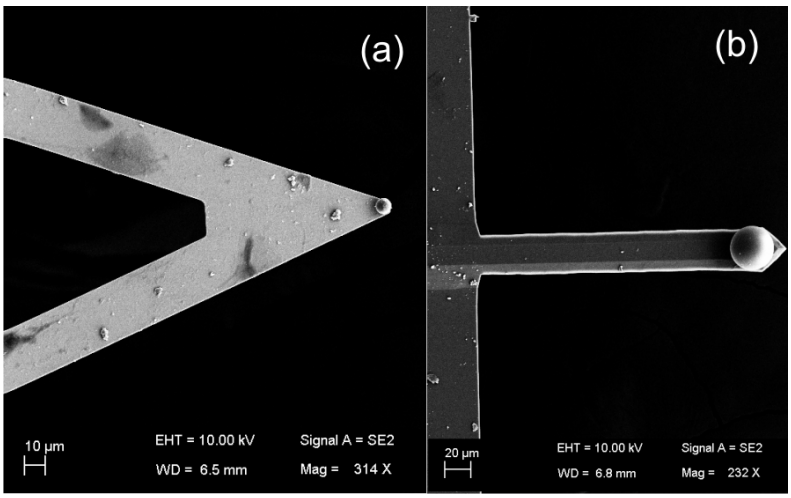

Figure 3.4: SEM images of utilized cantilevers. (a) SEM image of v-shaped cantilever with attached glass sphere. (b) SEM image of rectangular cantilever with attached glass sphere.

erence cantilever was used for calibration. Here, a cantilever with a known spring constant deflects the cantilever with an unknown spring constant [Tor96, Pro09]. Errors of this method are estimated to be 20%.

3.3.3 Local Height Measurement

The knowledge of sample height is needed in order to account for substrate effects during indentation testing (see chapter 4). Height changes of the sample are assessed by comparing the contact point on the surface with the preceding indentation contact points at other indentation sites. Thus, cell heights and inclination angles between adjacent indentation points are measurable during indentation testing.

The uncertainty of finding the correct approach point on the surface due to soft samples and high noise introduces height errors. Additionally, height drift occurs during the course of taking several force curves in a row. Reasons for that are thermal gradients due to a 37°C environment during cell experiments and piezo heating, that cause thermal expansion over time. However, the thermal height drift over time is corrected to the first order with a linear function from reference approaches before and after sample indentation.

3.4 Indentation Parameters

Indentation parameters are (i) indenter shape and (ii) vertical driving velocity. Deviation in shape or velocity can introduce artifacts and corrupt the real material response.

In this thesis, spherical indenters are used exclusively . Glass spheres of different sizes[9] are attached to the end of tipless cantilevers utilizing UV curing glue[10]. This is performed by dipping the cantilever end into glue and subsequently pressing the cantilever onto the sphere. Spherical

[9] Borosilicate glass spheres 8 μm from SPI supplies; Glass spheres 0-50 μm Worf Glasskugeln
[10] Loctite 3211, Henkel Technologies

indenters are perfectly symmetric, robust to damage and the radius can be easily measured through high magnification light microscopy and the Scanning Electron Microscope (SEM) (see figure 3.4 (a) and (b)) compared to other shapes as, e.g., sharp pyramidal indenters. In addition, spherical indenters induce less sample strain, which can be crucial for soft linear elastic samples and large indentations in order to stay in the linear elastic material regime. Further, since the cantilever is mounted at an angle with respect to the surface, there is a danger of pointed tips scratching the surface rather than, or in addition to, indenting it.

If the sample material response is time dependent, the vertical indenter velocity or loading rate needs to be consistent. The driving velocity (see equation 3.5) of the z-scanner can be set to a constant value in closed loop mode for the used device. This is contrary to a publication that observed the inconsistancy of the driving speeds in several commercially available AFMs including the MFP-3D [Sem06].

$$\frac{dZ}{dt} = const. \tag{3.5}$$

However, the actual indentation velocity (see equations 3.6 to 3.7) is not constant and smaller than the driving velocity, considering equation 3.4 and a positive deflection.

$$\frac{dI}{dt} = \frac{d(Z-D)}{dt} = \frac{dZ}{dt} - \frac{dD}{dt} \leq \frac{dZ}{dt} \tag{3.6}$$

$$\frac{dI}{dt} \neq const. \tag{3.7}$$

A constant indentation speed is not practicable, because of a small trigger force that needs to be set, which is complicated for high noise and soft samples such as cells. Thus, in this thesis, constant driving velocities are applied. For quasistatic indentation tests, a driving velocity of 0.2 μm/s, and for fast indentation 5 μm/s is employed.

3.5 Force Relaxation Curves

By introducing a dwell time when the indenter reaches its maximum force during fast indentation testing, force relaxation phenomena for time-dependent material responses are observed. While the indenter rests at a constant vertical position, the force-time dependence is observed (see figure 3.5). However, it must be noted that the indentation process takes a certain time, whereas relaxtion theory usually assumes an instantanious steplike deformation. Thus, relaxation events on the timescale of indentation and shorter can not be observed.

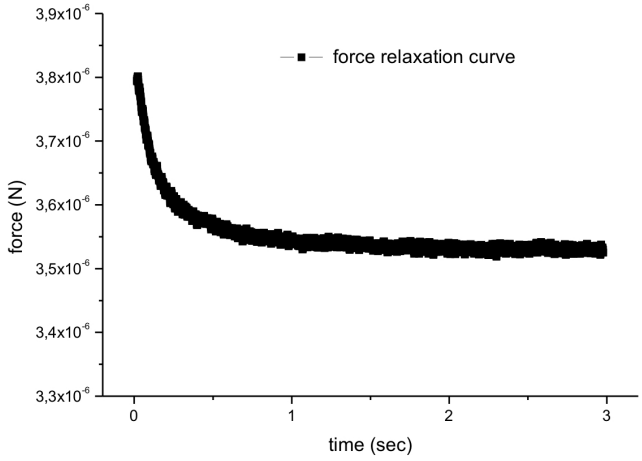

Figure 3.5: Example of a force relaxation curve. The cantilever is dwelled at a constant vertical position and the force relaxation behavior of the material is recorded.

Chapter 4

Indenting Elastic PDMS Thin Layers

4.1 Introduction

After introducing the AFM as an indentation tool in chapter 3, the following chapter presents spherical indentation on the elastic model material Polydimethylsiloxane (PDMS). It will be shown experimentally that substrate effects, if not accounted for with the appropriate theoretical model, introduce stiffening artifacts for thin layered materials. The confirmation of the thin layer corrected elastic material model is the basis for living cell indentation testing in chapter 5. The cell is then approximated as an elastic thin layer on a stiff substrate. Further, AFM performance and the reproducibility of indentation testing is proved with the PDMS model system. This is not possible during living cell indentation because active material reorganization over time is present.

Living cells are not exactly flat nor purely elastic as assumed by the theoretical models. Adherent cells spread on a surface and have a maximum height of 5 to 15 μm over the nucleus region, which decreases to only several hundred nanometers towards the cell edge. Further, cells, as well as PDMS, show a time dependent material response. Artifacts of 3D curvature as well as sample inclination and material time dependencies during indentation are discussed briefly in the last section of this chapter.

The chapter will start with introducing the PDMS materials properties and sample preparation. Subsequently the Hertz model and the thin layer corrected Hertz model for spherical indentation are explained and finally the results on indentation testing on bulk and thin layer PDMS are presented.

4.2 PDMS as Elastic Model Material

4.2.1 Properties of PDMS

Polydimethylsiloxane (PDMS) is reported to a have a mainly elastic material response. It is used here as a model material for indentation testing. PDMS is a silicon rubber that is often used in research for casting of micromachines and microfluidic devices [Sia03] as in Part III of this thesis. It is colorless, flexible, non toxic, gas permeable, has a low chemical reactivity, is hydrophobic by its nature but can be made hydrophillic by plasma activation. Preparation is easily done by mixing the viscous PDMS base and the crosslinking agent. After curing at a certain temperature

and for a sufficient time, the crosslinking process ends and the PDMS is a stable and mainly elastic material.

The main factor determining materials properties is the ratio of PDMS base to crosslinker [Car05]. Although crosslink density is proportional to the elastic modulus for polymer networks in rubber elastic theory, it has been shown that the elastic modulus decreases for PDMS as the PDMS to crosslinker ratio overtakes a certain limit [Kha09]. Elastic moduli ranging from 0.5 to 3 MPa [Kha09,Deu09] as well as time dependent responses are reported in literature. Other factors influencing the materials properties are curing temperature and curing time. Changes of PDMS properties over a longer time span, are usually referred to as aging effects or environmental effects.

Important to note is, that for the same PDMS polymer, from the same distributor and with same mixing concentration, values for the elastic moduli differ in literature. The reason for that - besides rate dependencies, simple concentration errors, curing time differences - are the methods of testing and the applied theoretical background [Car05, Kha09].

4.2.2 Bulk Samples and Thin Layer Microshape Preparation

Bulk Samples

For bulk PDMS[1] indentation testing, 15:1 and 10:1 base to crosslinker weight ratios are used, which corresponds to approximately 6% and 9% of crosslinker, respectively. The polymer samples are cured at 80°C for two hours in a plastic petri dish and used within 48 hours. The PDMS samples are perfectly flat due to gravity during curing and have a height of at least 2 mm, which is large compared to a maximum indentation depth of about 800 nm. Thus, the PDMS can be considered as a flat bulk sample. Shortly before the testing, the thick PDMS sheets are plasma[2] treated in order to make the surface hydrophillic. The indentation measurements were conducted in deionized water at room temperature, which is estimated to vary only about +/-2°C in the course of testing.

Thin Layer Microshapes

Thin PDMS layers are produced on the micrometer scale and termed microshapes. A single thin hair fiber with a diameter of approximately 50 to 100 μm is dipped in PDMS (15:1) and subsequently the PDMS is printed in arbitrary patterns on a glass slide by sliding the fiber over the surface. This results in a random PDMS structure of several microns height as shown in figure 4.1. The thin layers were fluorescently labeled with fluoresceine[3] for better visualisation with the microscope. For this, the fluoresceine was dissolved in isopropanol and subsequently a small amount ($\leq$1%) was mixed into the PDMS. As a control, bulk samples were produced from the same batch. Further treatment, is done as discribed for the bulk samples.

[1] Sylgard 184 Elastomer Kit, Dow Corning
[2] TePla 100E PS, PVA TePla AG(0.1 mbar O_2, 100 mW, 5 s)
[3] Fluoresceine, Sigma-Aldrich

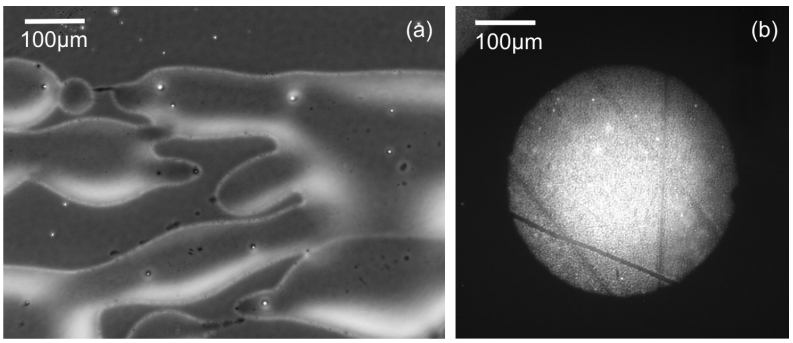

Figure 4.1: PDMS microshapes. (a) Phase contrast images of thin layers made of PDMS. (b) Image of fluoresceine labelled round shaped thin PDMS layer.

4.3 Elastic Theory and Fitting for Spherical Indentation Testing

4.3.1 The Hertz Elastic Model for Spherical Indentation

In the following, the Hertz model for the contact of a sphere with a flat substrate is presented [Her81, Sne65, Lan05]. In this particular case, the indenter sphere is not deformed during indentation and the Poisson ratio for the indented material is 0.5 as for an incompressible material. The Hertz model is only valid for linear elastic materials at small strains, no adhesion forces and an infinitely thick sample. However, for samples with finite thickness, it is commonly accepted to use the Hertz model up to an indentation depth of 10% of the specimen height without the occurance of major artifacts due to substrate influences.

The force-indentation depth relation (see equation 4.1) is linear dependent on the elastic modulus (E), as the elastic modulus is assumed to be homogenous througout the material. The square root dependency of the force on the radius (R) of the spherical indenter, as well as the exponent $\frac{3}{2}$ for the indentation depth arise due to the geometry of the spherical indenter. Further, the geometric contact radius (a_{Hertz}) (see equation 4.2), can be expressed in terms of force, radius and elastic modulus. The contact radius is helpful to estimate the contact area between indenter and sample. A sketch depicting all parameters for the Hertz model is shown in figure 4.2.

$$F_{Hertz} = \frac{16}{9} E R^{\frac{1}{2}} I^{\frac{3}{2}} \tag{4.1}$$

$$a_{Hertz} = [RI]^{\frac{1}{2}} = \left[\frac{9FR}{16E}\right]^{\frac{1}{3}} \tag{4.2}$$

4.3.2 The Thin Layer Corrected Hertz Model

A simple analytical correction to the Hertz model for spherical indentation of layers with finite thickness has been published by Dimitriades et al. [Dim02]. This solution is easy to implement in contrast to previous works, where the geometric nonlinearities of the thin layer problem required extensive computations or were only assessed qualitatively. The corrected Hertz model is based on simplifying the exact intergral equatios for the thin layer problem in order to arrive to a simple analytical expression for surface bonded thin elastic layers [Dim02]. For the Thin Layer

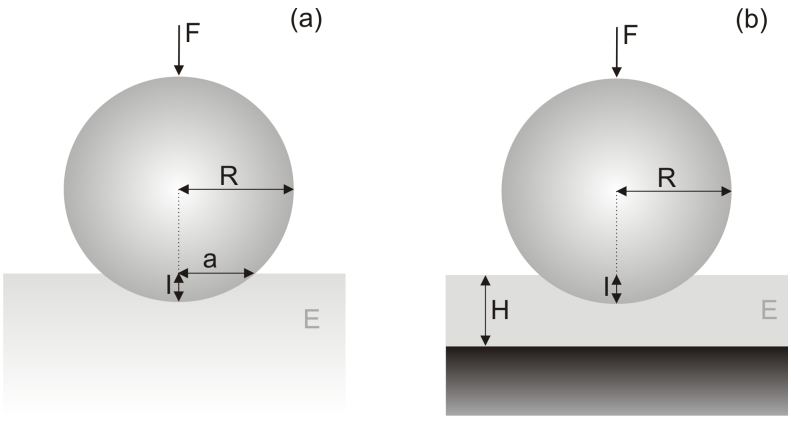

Figure 4.2: Sketch of parameters and boundary conditions in (a) the Hertz model and (b) the thin layer corrected (TLC) model for spherical indentation.

Corrected (TLC) model, the Hertz function is corrected with a polynomial of α, which is again a function of indentation depth (I), indenter radius (R), and specimen height (H) (see equations 4.3 and 4.4). For an infinite specimen height, the TLC model converges to the Hertz model. An incompressible material and undeformed indenter are assumed.

$$F_{TLC} = F_{Hertz}\left[1 + 1.333\alpha + 1.283\alpha^2 + 0.769\alpha^3 + 0.0975\alpha^4\right] \tag{4.3}$$

$$\alpha = \frac{[RI]^{\frac{1}{2}}}{H} \tag{4.4}$$

The ratio of the Hertz elastic modulus and TLC elastic modulus (see equation 4.5) gives an estimate of the substrate influence on the elastic modulus. The ratio is independent of the elastic modulus and only dependent on α (see equation 4.5).

$$\frac{E_{Hertz}}{E_{TLC}} = \left[1 + 1.333\alpha + 1.283\alpha^2 + 0.769\alpha^3 + 0.0975\alpha^4\right] \tag{4.5}$$

Even for the commonly accepted indentation depth of 10% of the specimen height, an error of approximately 50% is expected if a constant radius and height as for the later experiments (R=4 μm, H =2 and 4 μm) is assumed as shown in figure 4.3. The reason for this is the influence of the indenter radius and not only indentation depth in α.

The thin layer correction of the Hertz model has been experimentally applied for thin layer gels [Dim02, Eng04] and living cells [Dar07].

4.3.3 Model Fitting

Fitting the model to the data is done with a custom written Matlab routine (The MathWorks Inc.) by minimizing the sum of squared residuals (χ^2) (see equation 4.6), commonly referred to as least squares method. F_{model} describes the force-indentation relation using the indentation depth (I_{data}), as independent variable. Th elastic modulus (E) and the approach point onto the surface (I_0) are the two optimized parameters. The fitted parameter, I_0, corrects the previous manually chosen approach point (see section 3.3.1). For the TLC model, the sample height (H) input is needed. For judging the goodness of the fits, the residual (r) (see equation 4.7) is calculated and

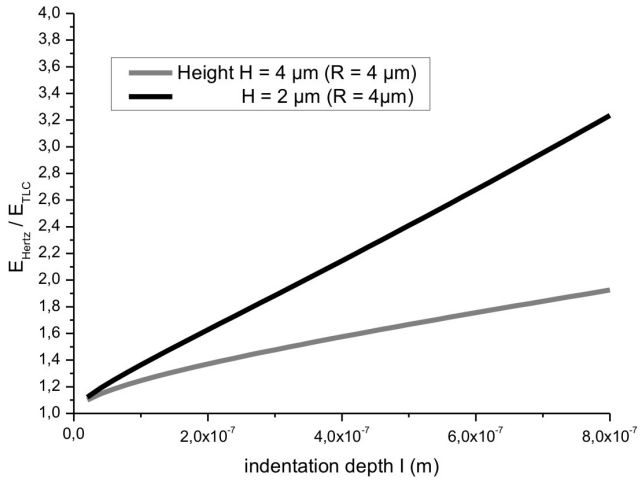

Figure 4.3: Ratio of Hertz elastic modulus to TLC model elastic modulus for experimental parameters as a function of indentation depth. The ratio gives an estimation for error due to the underlying substrate.

the distribution of residulas is checked for normality. Errors due to the AFM data are estimated with fits to the worst case data and give a minimum and maximum elastic modulus, E_{min} and E_{max}.

$$\chi^2(E, I_0) = \left(\sum_i \left[F_{model}(I_{data,i}; E, I_0) - F_{data,i} \right]^2 \right) \tag{4.6}$$

$$r_i = F_{model,i}\left(E^*, I_0^*\right) - F_{data,i} \tag{4.7}$$

4.3.4 The Viscoelastic Standard Linear Solid

The term viscoelasticity is sometimes used as an umbrella term for a time-dependent material response. Here, linear viscoelasticity is assumed and the standard linear solid model is presented. It is used to quantify the time dependent material response of PDMS. The standard linear solid model assumes the material to behave as a Hookean spring in parallel with another spring and a Newtonian dashpot in series (see figure 4.4).

By using the elastic-viscoelastic correspondence principle and replacing the time independent elastic modulus in the Hertz (or the TLC) model with a time dependent elastic modulus via a Laplace Transform [Lak99], a description for the force relaxation curve for a spherical indenter (see equation 4.8) is obtained [Gal08, Mat06]. An equlibrium modulus (E_∞), an instantaneous modulus (E_0), the elastic fraction (F_E), the dashpot associated viscosity (η) and a characteristic time (τ) can be extracted (see equations 4.8 to 4.11). In particular, the equilibrium modulus repesents the elastic modulus for slow quasistatic indentations, the elastic fraction gives a measure for how close the material behavior is to a purely elastic material.

$$F(t) = F_{model}(E_\infty, I_{max}) + F_{model}(E_D, I_{max}) exp(-\frac{1}{\tau}t) \tag{4.8}$$

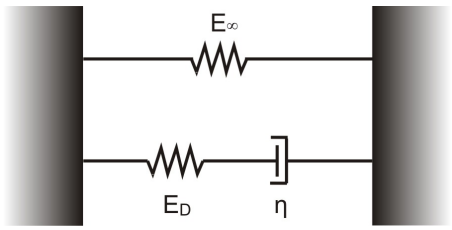

Figure 4.4: Schematic illustration of the Standard Linear Solid viscoelastic model.

$$E_0 = E_\infty + E_D \tag{4.9}$$

$$F_E = \frac{E_\infty}{E_0}; \tag{4.10}$$

$$\eta = \tau E_D \tag{4.11}$$

4.4 Spherical Indentation on bulk PDMS

The resulting force-indentation curves for indenting[4] bulk PDMS samples of a 10:1 and a 15:1 base to crosslinker mixing ratio are shown in figure 4.5. Clearly, the 10:1 sample responds with a much higher resistance to deformation than the 15:1 sample. As expected for a bulk elastic PDMS sample, the Hertz model fits the data (see figure 4.5).

Elastic moduli of 1.8x10^6 Pa and 0.8x10^6 Pa (+/-20%) are determined for the PDMS samples as shown in figure 4.6. In order to check for depth effects on the elastic modulus, data intervals for fitting were extended accordingly. No significant depth effects are present. Further, different indenter radius sizes were used in order to impose different surface strains at equivalent indentation depths. No significant strain effects are detectable (see figure 4.7). The high variation of the elastic moduli for small indentation depths is due to a bigger influence of approach point error and is no real material effect.

For completeness, force indentation curves needed to be corrected for AFM cantilever system deformation (D_{AFM}) which is dependent on force and is revealed by non linearities in the reference force distance curve. The origin of this is an intrinsic deformation of the mechanical parts of the AFM and the indenter at high loads. If the AFM system deformation (D_{AFM}) is not accounted for, an apparent softening with depth is detected. The indentation depth (see equation 4.12) is corrected with the AFM deformation (D_{AFM}) in dependence of detected cantilever bending and thus force. For this, the apparent corrected sensitivity S_{cor} is used (see equation 4.13), which is well discribed as a linear function as shown by the data in figure 4.8.

$$I = Z - D - D_{AFM} = Z - US_{cor} \tag{4.12}$$

$$S_{cor} = [c_1 + c_2 Z]^{-1};\ c_1 = [\frac{dU}{dZ}(z=0)];\ c_2 = [\frac{d^2U}{dZ^2}(z)] \tag{4.13}$$

[4]The samples were indented with an indenter driving velocity of 1 μm/s and an indenter radius of 4μm unless otherwise noted. Raw data to force-indentation curve conversion and cantilever calibration is to be found in section 3.3.

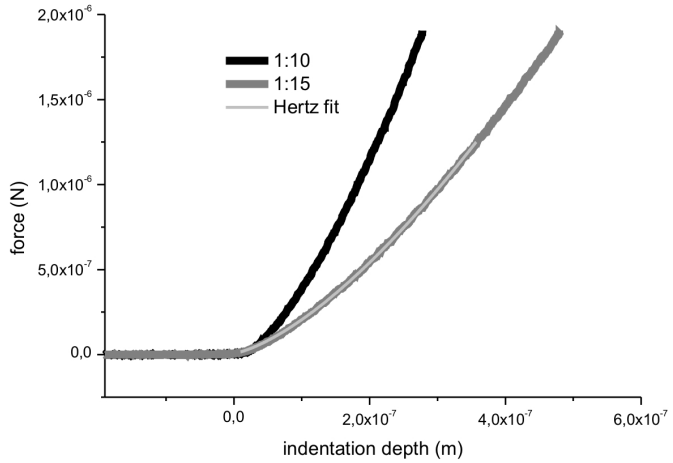

Figure 4.5: Force indentation curves of a 10:1 and a 15:1 bulk PDMS sample. The 15:1 sample is more compliant due to less crosslinking agent. The Hertz model fits the bulk data as expected.

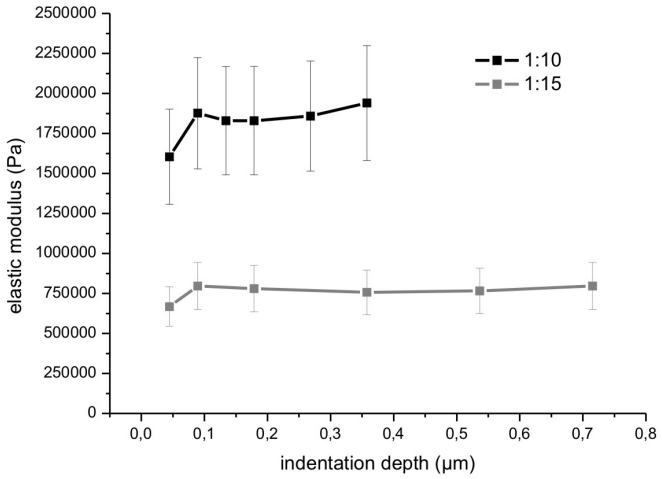

Figure 4.6: Elastic moduli of 10:1 and 15:1 PDMS samples as a function of indentation depth. The Hertz model fitting limits were extended accordingly. No depth effects are observed.

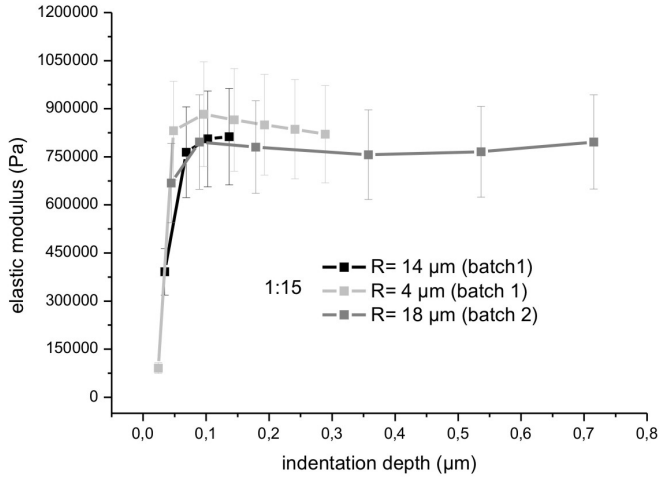

Figure 4.7: Elastic moduli for two different 15:1 PDMS batches and different radii. The different radii impose different indenter surface strains at the same indentation depth. No strain effects are observed in the measurement error limits.

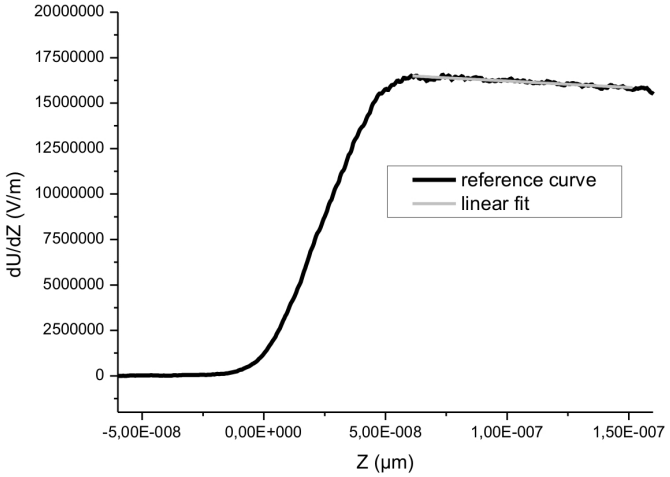

Figure 4.8: First derivative of a reference force indentation curve on a hard surface. A constant sensitivity plateau is expected for no AFM deformation. In the case of high load, AFM deformation is present as shown in here.

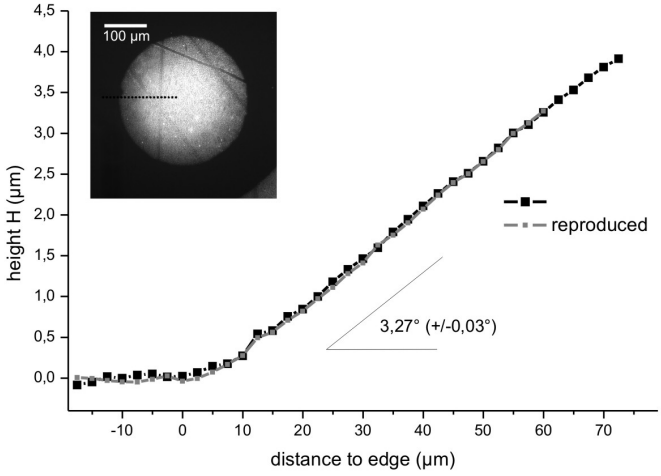

Figure 4.9: Height profiles and fluorescently labelled PDMS thin layer . The indentation profile path is indicated with black dot in the inset.

4.5 Spherical Indentation on Thin PMDS Layers

In order to be able to fit the TLC model, the layer height needs to be determined. The reproducibility of height measurements with AFM could be confirmed for the PDMS thin layers. Figure 4.9 shows the fluorescently labelled microshape as well as the measured heights and angles along a pointwise indentation[5] profile from the edge towards the center. Heights and inclination angle are excactly reproducable within the stepsize of 2.5 μm between the indentation spots. The fitting routine estimates the errors of the approach point, and thus height, to only several nanometers.

The elastic modulus of the PDMS thin layer is evaluated with the Hertz elastic model and the TLC model. As a first comparison, force indentation curves from a bulk sample and a thin layer at 2 μm height already show that the thin layer appears stiffer (see figure 4.10). This is solely an effect of the underlying substrate, which will be proved in the following.

To investigate the extent of the substrate effect as a function of indentation depth and layer height on the elastic modulus calculation seperately, two approaches were taken. First, an elastic profile over the PDMS thin layer, which varies in height from layer edge towards the middle, is fitted using the Hertz and the TLC model. The maximum indentation depth is kept constant. Figure 4.11 shows a clear increase of elastic modulus for the Hertz model towards smaller sample heights, while the TLC model reveals a fairly constant elastic modulus. Second, for one point on the sample with a height of 2 μm, different indentation depths are evaluated. Figure 4.12 shows the strongly increasing substrate influence for the Hertz elastic modulus with increasing indentation depth. A less significant variation with increasing indentation depth is seen for the TLC model.

To summarize, the effect of a stiff underlying substrate dominates the indentation response of compliant thin layers. The Hertz model increasingly overestimates the elastic modulus when the

[5]The sample was indented with an indenter driving velocity of 1 μm/s and an indenter radius of 4μm. Raw data to force-indentation curve conversion and cantilever calibration is to be found in section 3.3.

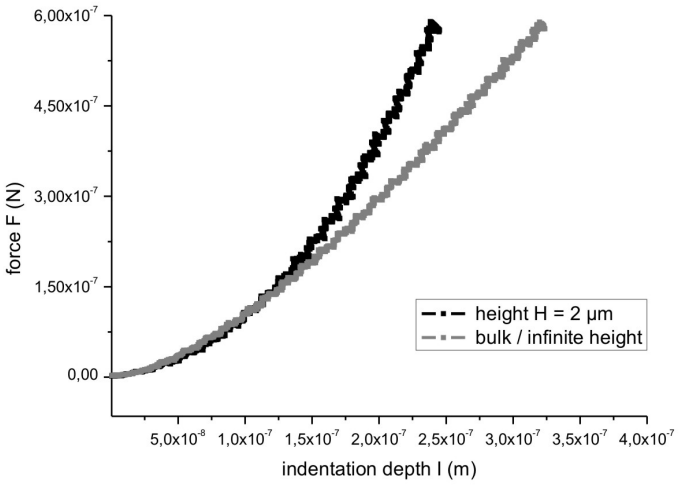

Figure 4.10: Force indentation curves taken on a thin layer and on a bulk 15:1 PDMS sample. The thin layer has a higher resistance to deformation. This is solely a substrate effect.

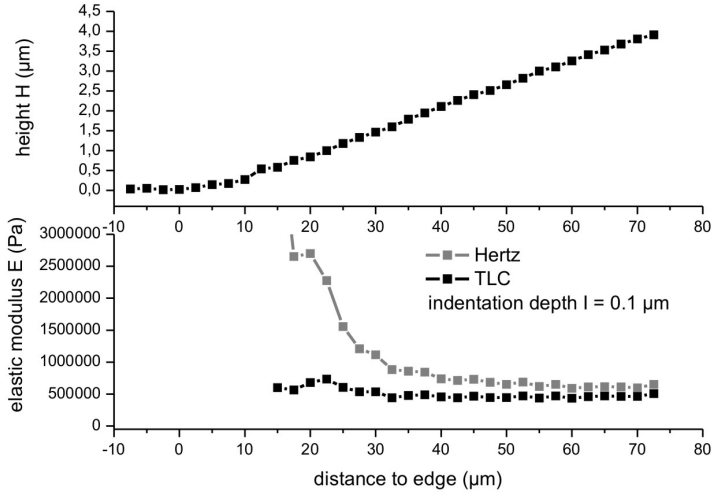

Figure 4.11: Height and elastic modulus profile for Hertz model and TLC model at constant indentation depth. The Hertz elastic modulus increases towards smaller heights, while the TLC elastic modulus corrects for substrate effects and reveals a constant elastic modulus.

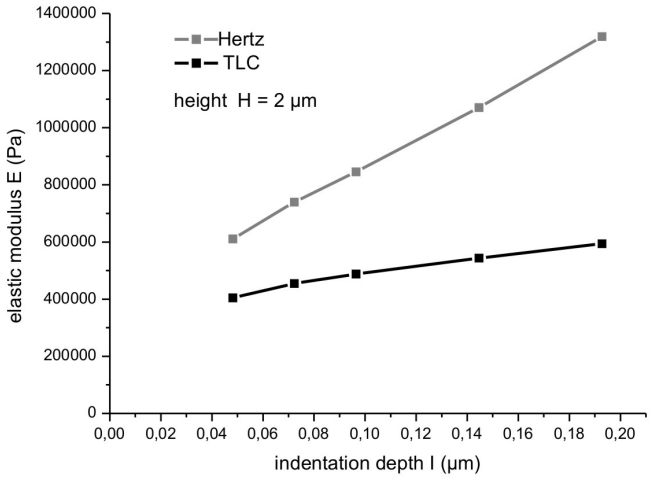

Figure 4.12: Hertz and TLC model elastic modulus plotted against the maximum indentation depth at a constant layer height. The Hertz elastic modulus increases twofold towards a larger indentation depth, while the TLC elastic modulus corrects for substrate effects and reveals a more constant elastic modulus.

compliant layer becomes thinner, while the TLC model corrects for substrate effects and obtains a constant elastic modulus.

However, for the direct comparison with the bulk case, a bulk sample from the same batch of PDMS as the thin layer was investigated. Surprisingly, the microshape is 30% more compliant than the bulk. This phenomenon was reproduced a second time. It is assumed to be a small scale effect and need to be investigated further.

4.6 Artifacts in Indentation Testing

4.6.1 Time Dependent Material Responses

Although PDMS is as a first approximation elastic, its materials response also displays time dependencies. To investigate the extent of this, the elastic modulus is determined on bulk PDMS at different indenter driving velocities (see figure 4.13(a)), which are then referred to as effective elastic moduli. An increase in effective modulus with driving velocity is observed. Still, time dependencies are small and in the range of experimental errors.

Further, force relaxation is observed (see figure 4.13 (b) and (c)) while dwelling the cantilever at maximum indentation depth for different driving velocities and evaluated with the theoretical model of a standard viscoelastic linear solid (see section 4.3.4) for the fastest, steplike, indentation. For a bulk 15:1 PDMS sample, the elastic fraction is determined to be 97%. This confirms that the PDMS response is mainly elastic. The corresponding equilibrium elastic modulus is plotted in figure 4.13 (a) for a velocity equal to zero. However, from the quality of the fit (see figure 4.13(c)), it is obvious that the standard linear solid is just a rough approximation to the PDMS time-dependent behavior. A double logarithmic plot (see 4.13(d)) suggests a more power

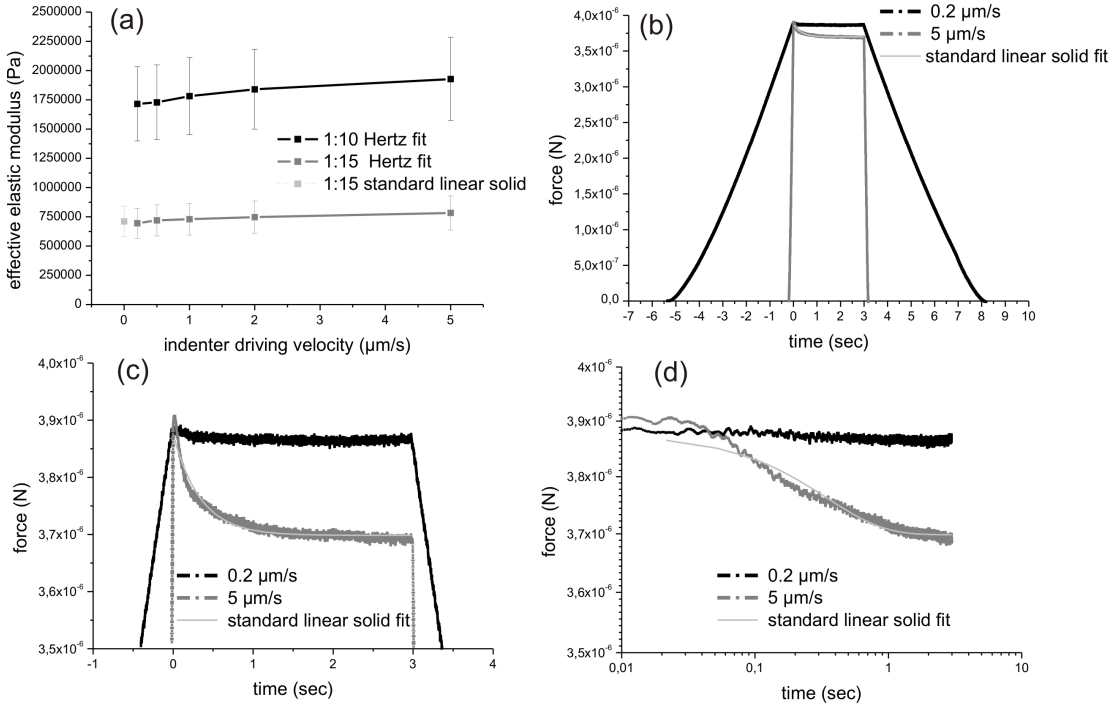

Figure 4.13: Time dependent behavior of bulk PDMS. (a) Effective elastic moduli of 10:1 and 15:1 bulk PDMS samples as a function of indenter driving velocity. (b) and (c) Force relaxtion curves of a 15:1 bulk PDMS sample and standard linear solid fit for fast indentations. (d) Log-log plot of same force relaxation curves as in c and d revealing a power law behavior.

law like behavior.

4.6.2 Curvature and Sample Inclination

Considering a sample with a positive 3D curvature (see figure 4.14), as e.g. a living cell, the contact area is systematically overestimated, when assuming the Hertz model for a flat surface. In turn, the elastic modulus is underestimated (see equation 4.2). However, for the thin layer PDMS microshape the curvature is estimated to be negligable.

Additionally, at inclinations of a curved sample, shear forces appear and eventually cause sliding of the tip that again alters the force indentation response. In order to observe this effect in a qualitative way, indentation testing was performed on PDMS inclinations and apparent elastic moduli were fitted. A clear decrease for higher inclination angles suggests the occurrence of indenter sliding (see figure 4.15 a). If sliding occurs, the elastic modulus will be underestimated. Production of a PDMS inclination was simply achieved by tilting the PDMS container prior to and during crosslinking.

To directly observe indenter sliding, the inclinations were indented with the cantilever long axis turned 90° with respect to the inclination in order to record sliding in the lateral signal, which is detecting cantilever torsion. Figure 4.15 b shows the constant plateau and later decrease in

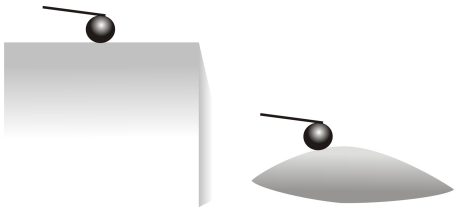

Figure 4.14: Sketch of an ideally flat sample vs. a curves cell like sample.

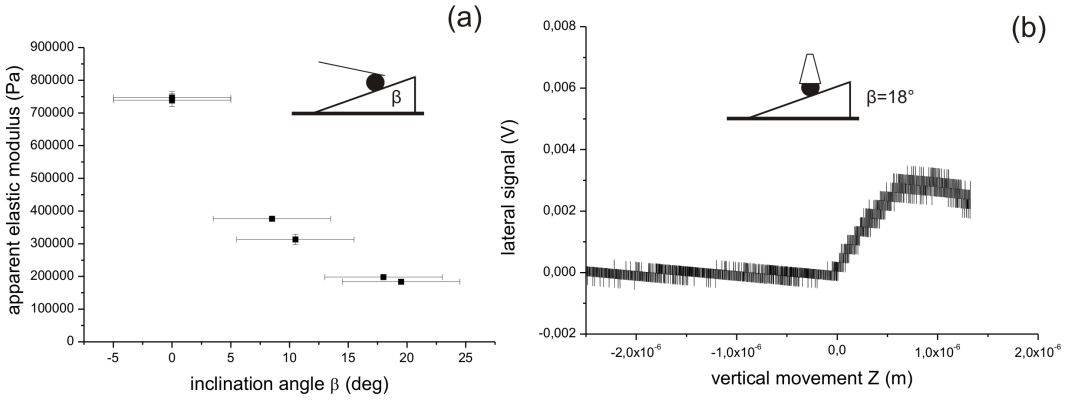

Figure 4.15: (a) Apparent elastic modulus as a function of inclination angle and (b) sliding event at inclination in lateral signal.

the lateral signal, when indenting 90° turned towards the inclination of 18°, which is typical for a sliding event. A continous increase of the lateral signal would be expected for no sliding. However, for the indented thin layer microshapes with an inclination angle of 3° no indenter sliding was observed.

4.6.3 Lateral Forces

During the indentation process, not only normal forces in the z-direction are exerted on the sample but also lateral forces in the xy-plane. Lateral forces originate from torques, which are intrinsic with the bending of the force sensor itself [VanL97, VanL97b]. An angle of the cantilever relative to the normal surface and an assymetry of the tip position will induce additional torques and a rotation of the tip which is transduced to the sample.

Forces due to tip rotation are compensated by friction and, as a result, shear forces act on the sample. If a shear force occurs, the contact area between the sample and indenter is changed due to sample deformation as it has been shown by Toikka et al. [Toi99] (see figure 4.16). In the case of small friction resistance, sliding of the indenter can occur as shown in section 4.6.2.

However, it is assumed that shearing plays a minor role for PDMS indentation experiments, because no significant differences were observed between independent PDMS indentation experiments, where shearing errors should be noted if they were significant.

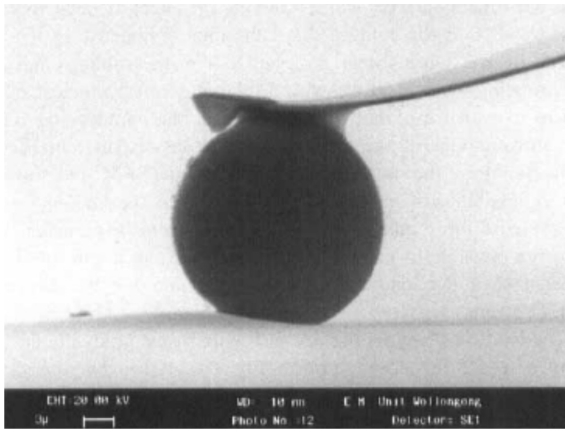

Figure 4.16: SEM Image from Toikka et al. [Toi99] showing material shearing during cantilever retraction.

Chapter 5

Indenting Living Cells and Cellular Fiber Networks

5.1 Introduction

In this chapter, living pancreatic cancer cells (Panc-1) and their keratin intermediate filament network are probed with AFM indentation testing. Both sample types are approximated as thin elastic layers and evaluated with the TLC model, which corrects for substrate effects and was verified for thin elastic PDMS layers in chapter 4.

In contrast to the model material PDMS, living cells are inhomogeneous, very soft and constantly optimizing objects. Several challenges arise when attempting to mechanically characterize cells and will be addressed. Material inhomogeneity on the nano to micro scale leads to averaging effects depending on indenter size, indentation depth and corresponding contact area. The softness induces higher approach point errors and large strains can be quickly reached. However, the main challenge in working with cells is the variation within the living cell ensemble as well as the possible active cell reactions during experiments, because every change in environmental condition or treatment will potentially induce active reactions in the cell over time.

Nonetheless, the elastic approximation of the cell is a useful method for comparing cells or in general materials with each other. The elastic modulus of living pancreatic cancer cells is compared to the elastic modulus of the cellular keratin intermediate network. This gives an estimation of the importance of the keratin network inside living cells and is compared to other previous studies on keratin networks. Further, living cells with different dense keratin network phenotypes are tested.

The chapter will start with the biological motivation and will elucidate the importance of this work in context of biomaterials testing. It is continued with experiments on living cells followed by indentation testing on the keratin networks. Time dependent materials models for cells, such as linear viscoelasticity, power-law behavior and poroelasticity, are discussed in brief. Keratin network stretching is observed in a qualitative way. At the end of the chapter, the importance of the mechanical strength of the keratin network in Panc-1 cells during deformation is discussed.

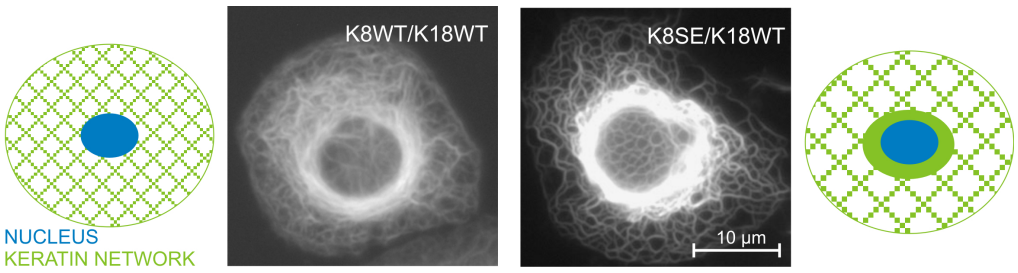

Figure 5.1: Sketch and fluorescently labelled K8WT/K18WT and K8SE/K18WT keratin network inside Panc-1 Cells. The K8SE/K18WT keratin network phenotype is characterised by a high density around the nucleus and a coarse mesh in the cell periphery, while the K8WT/K18WT keratin network phenotype has a medium meshsize throughout the whole cell.

5.2 Biological and Materials Science Objectives

The biological motivation of this study was to clarify the importance of the keratin intermediate filament network inside Panc-1 cells during slow deformation as for cell migration. For keratin network deficient Panc-1 cells, an enhanced migration activity in the cell culture dish and through pores was seen. This effect was first observed with Sphingosylphosphorylcholin (SPC) treated Panc-1 cell. SPC provokes a reorganisation of the keratin at a high density around the nucleus and a lower density in the cell periphery compared to constant distribution for a non treated cell. After excluding other possible explanations, it was hypothesized that less mechanical resistance to deformation is the reason for a higher motility. Cell softening, due to SPC incubation, has already been shown on a whole cell level with a microplate stretching experiment [Mic04].

Further work on the Panc-1 cell system clarified the underlying mechanisms for keratin network reorganisation (see section 2.2). A transient transfection, which mimicks the SPC phenotype (K8SE/K18WT), and a wildtype reference (K8WT/K18WT) were developed (see figure 5.1). Additionally, the keratin network is fluorecently labelled with the transfection. This enables colocalized mechanical testing and keratin network density imaging. The experimental requirements were local large deformations as in cell migration through small pores, which was put into practice in this thesis by using AFM indentation. It was expected that a correlation would be found between the keratin network density and the elastic modulus of the cell. As the interest lies in cell mechanical properties at the timescale and speed of cell migration (0.1-1 μm/min, [Bus08]), slow (so-called quasistatic) indentation tests on the cells are performed. A cantilever driving speed of 0.2 μm/s (=12 μm/min) was used for determining the theoretically time independent elastic modulus while excluding contributions from faster deformations.

The cell can be chemically treated (see section 5.3.3), so that everything is dissolved and removed from the cell leaving only the keratin intermediate filament network. This amazing ability of the keratin filament network to resist detergent treatment makes it possible to independently observe the keratin network properties, without the influences of other cytoskeleton parts as actin filaments and microtubuli. A directly comparable study to living cell indentation was conducted on the extracted keratin networks, using the same methodology with the exact same equipment and the same parameters. This is not trivial, because testing methods induce artifact. A direct comparison of a living cell versus its keratin cytoskeleton has not been reported in literature up to this point. The elastic modulus of the extracted keratin network, gives a first estimation on the impact of the keratin intermediate filament network inside the living cell.

5.3 Experimental Procedures and Preparation Protocols

5.3.1 Cell Culture and Transfection

Panc-1 cells were kept in culture (37°C, 5% CO_2) at a maximum confluency of 70% in DMEM[1] containing 10% FCS[2], 1% Penicillin-Streptavidin[3] and 1% L-glutamine[4]. Keratin wildtype (K8WT/K18WT) and keratin mutant (K8SE/K18WT) Panc-1 cells were transfected with eCFPK8WT/eYFPK18WT DNA and eCFPK8SE/eYFPK18WT DNA[5] respectively, using the reagent Metafectene[6]. Cells were seeded on round glass slides[7] at a density of 5x10^5 cells per petridish[8]. After 24 hours, cells were treated with the transfection reagent[9] and incubated for another 24 hours, followed by 12 hours in cell culture medium. Detailed information on the transfection process can be further found in [Bus08]. Subsequent to the transfection process, cells were starved in FCS free medium for at least 12 hours. This provokes a synchronisation of the cell cycle, e.g. having almost no dividing and proliferating cells that exhibit mitotic spindles. Before probing, cells were washed once with FCS free medium for removal of non-attached cells and cell parts.

5.3.2 AFM sample mounting and Indentation Testing

The glass slide with cells was mounted in the bio heater fluid cell assembly for use with the AFM. During indentation testing, the temperature was held at 37°C (+/-0.5). In the mounting phase, cells are exposed to room temperature for a maximum of 2 minutes. During the measurements, cells were kept in 25 mM Hepes buffered DMEM[10] containing 1% Penicillin-Streptavidin and 1% L-glutamine for a maxium of two hours without a 5% CO_2 atmosphere. Cell survival and fitness was assured by observing the cells optically for half an hour prior to probing and during the indentation testing.

After sample mounting, transfected cells are searched in the range of the 3x3 mm coarse positioning system. Transfected cells with a clear keratin phenotype, of either K8SE/K18WT or K8WT/K18WT, and a large cell area, preferrably single cells, are located via their fluorescently labelled keratin network. Only up to 2 cells per viewed area in the sample fulfilled these conditions. A high magnification fluorescence image is taken, before and after probing as well as brightfield images for every indentation point for later colocalisation. Indentation testing is started with at least 10 reference curves on the hard glass slide and is continued in a line profile on the cell towards the nucleus. The stepsize for the indentation spots was chosen to correspond to 15(+/-5) data points per cell, taking about 15 min time. Afterwards, at least 5 reference curves on the glass were taken to ensure a consistent experiment. Sphere gluing and cantilever spring constant calibration were performed as described in chapter 3.3.2 prior to cell experiments.

For the quasistatic indentation tests on living cells, the indenter driving velocity was 0.2 μm/s, and for fast indentation it was 5 μm/s. The indenter radii were 4 μm $\pm$ 0.5 μm and measured exactly after indentation testing. The maxium force during indentation was calibrated to not

[1] DMEM 11960, Gibco
[2] FCS, PAA Labs
[3] Penicillin-Streptavidin 15140, Gibco
[4] L-glutamine 25030, Gibco
[5] DNA was kindly provided by Prof. Dr. Thomas Seufferlein, Universität Ulm and Martin-Luther-Universität Halle-Wittenberg ([Bei04, Bus08])
[6] Metafectene, Biontex Labs
[7] Round glass slides (⌀ 3.5 cm), Fisher Scientific
[8] Petridish (⌀ 5 cm), Greiner Biotech
[9] 1μg DNA and 4 μl metafectene per 2ml cell culture medium
[10] DMEM 21063, Gibco

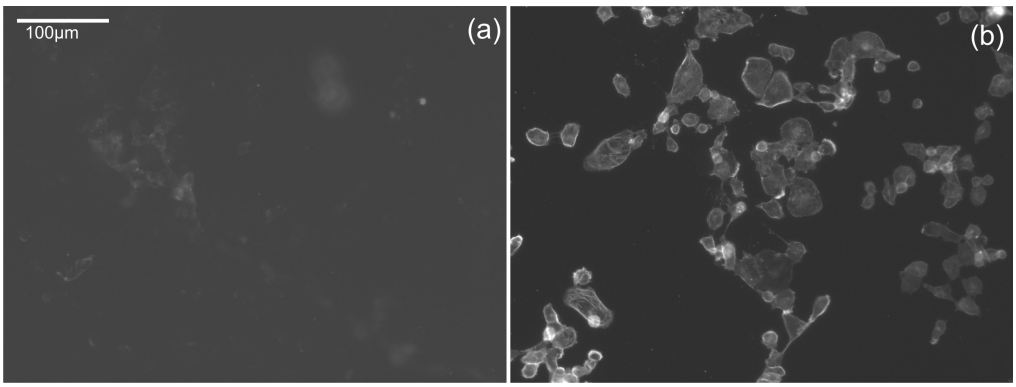

Figure 5.2: Actin fiber staining using phalloidin with (a) and without (b) gelsolin treatment. Through gelsolin treatment, less actin fibers are present and less contrast is visible in the images.

exceed 3 nN. Exact sensitivity calibration and data processing was done afterwards (see section 3.3.1).

5.3.3 Preparation of the Keratin Network

The extraction of the keratin intermediate filament network was done by utilizing a TritonX solution[11] for cell membrane disruption and several washing steps with buffer[12], followed by a gelsolin solution[13] treatment for removing the remaining actin fibers. The protocol from Beil et al. [Bei04] was utilized almost exactly[14]. Beil et al. also showed the remaining keratin after extraction by using immumogoldlabelling. Actin fiber staining with phalloidin[15] confirmed a highly reduced actin fiber occurance after gelsolin treatment (see figure 5.2). No fixation of the remaining keratin network was performed to prevent artificially induced crosslinking and, thus, network stiffening. The extracted keratin is finally transferred into phosphate buffered saline (PBS) and measured by AFM indentation within 48 hours.

For observation in the SEM, the keratin networks were stepwise transferred to a 100% ethanol solution (20% concentration steps, 20 min each), and critical point dried[16]. Afterwards, a layer of 5(+/-2) nm gold was sputtered[17] on top to achieve a conductive sample .

5.4 Quasistatic Indentation of Pancreatic Cancer Cells

5.4.1 The Cell Elastic Profile

Pointwise probing in a straight line pattern from the cell edge towards the nucleus was preferred to whole cell mapping, considering probing time and symmetry of the keratin intermediate fil-

[11] 1% TritonX-100, 2.2% PEG (35kDa), 50 mM imidazole, 50 mM KCl, 0.5 mM $MgCl_2$, 0.1 mM EDTA, 1 mM EGTA

[12] 50 mM imidazole, 50 mM KCl, 0.5 mM $MgCl_2$, 0.1 mM EDTA, 1 mM EGTA

[13] 5 U/ml gelsolin (gelsolin from human plasm, Sigma), 1 mM $CaCl_2$, 150 mM KCl, 0.2 mM ATP and 1 mM DTT

[14] PBS wash, 20 min TritonX solution at room temperature, 2x buffer wash for 4 min, 1 h gelsolin solution at 28°C, buffer wash, PBS wash

[15] Alexa Fluor 647 phalloidin, Invitrogen

[16] Critical point dryer CPD 030, BAL-TEC

[17] Coating System MED 020, BAL-TEC

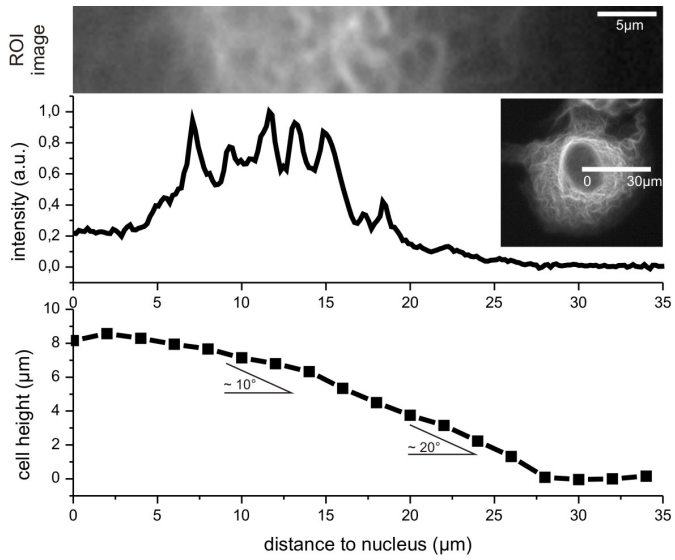

Figure 5.3: Height profile and corresponding keratin network fluorescence intensity of living K8WT/K18WT Panc-1 cell.

ament network. The fluorescent labelling of the keratin network allowed direct observation of the keratin phenotypes of the cells. This enabled measurements of an elastic and height profile coordinated with an image of the keratin network. In the following, the data evaluation of height and elastic moduli of a single wildtype (K8WT/K18WT) cell are shown in detail, before comparing a higher number of cells (see section 5.4.2).

Figure 5.3 shows the cell height profile, the fluorescently labelled keratin network inside the cell as well as the selected region of interest and the corresponding intensity profile. The cell height profile exhibits inclinations of up to 20° in the cell periphery, decreasing to 0° towards the nucleus at a maximum height of 8 μm.

The TLC model (see section 4.3.2) for spherical indentation is used for data evaluation of each force-indentation curve along the profile. The force indentation curves are fitted up to indentation depths of 10, 20 and 40% cell height or, respectively, only up the maximum available data range (see figure 5.4) in order to check for depth dependencies. The TLC model already accounts for indentation depth and layer height dependencies due to substrate effects. It is clearly visible that elastic modulus measurements oscillate for smaller indentation depths and a clear depth effect directionality towards material hardening or softening is not prominent. Towards higher indentation depths, the elastic profile of the cell is smoother. This is due to a decreasing influence in approach point errors with higher indentation depth, which is accompanied by an averaging effect with depth. Both a correct approach point choice and averaging result in a smoothed elastic profile with no outlying data points due to drastic changes in elastic modulus. A clear distinction between the two effects is not possible.

Errors are estimated with fits to the worst case data, revealing a minimal an maximal elastic moodulus (E_{min}, E_{max})(see section 4.3.3), knowing the dependencies on the error inducing input parameters as cantilever spring constant, sensitivity, indenter radius and height. This estimation leads to the result that cells with a difference in elastic modulus of 35 to 20 Pa can be distinguished. This translates to a maximum relative resolution in elastic moduli of 20 to 30%.

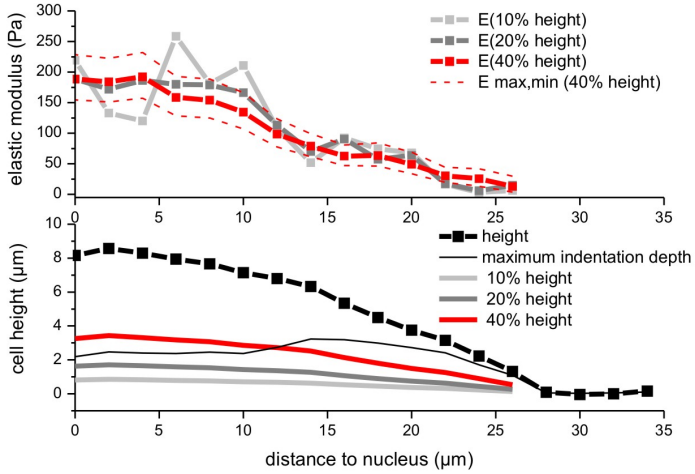

Figure 5.4: Height profile and elastic modulus profile of living K8WT/K18WT Panc-1 cell. The data are fitted up to different indentation depths, which are measured in a percentage of cell height.

The resolution further decreases for smaller heights due to increased influence of height errors. This is still under the assumption of the same cantilever type and the same fitting depth assuring less influence in approach point errors. As a comparison, applying the Hertz model to the data revealed an increase in the elastic modulus of almost 100%.

To summarize, depths effects on the elastic modulus of the cells are not visible due to more prominent effects of approach point errors and averaging. In the best case, elastic moduli with 20% difference can be distinguished due to measurement errors.

5.4.2 Panc-1 Cell Elastic Moduli and Influence of Keratin Network Density

The elastic profiles of a higher number of cells will be compared now. As a standard, the fitting limit of 40% cell height, as described above, is used for the evaluation of cell elastic profiles of K8WT/K18WT and K8SE/K18WT transfected cells. The difficulty of comparing several cell profiles is solved by a graphical comparison. All measured heights and evaluated elastic profiles are plotted versus the normalized cell width, where the nucleus is defined as zero and the cell edge as one. Figure 5.5 shows separate plots for both keratin phenotypes and the merged data.

It is obvious that the cell to cell variation in the elastic moduli is extremely high. The elastic modulus over the nucleus area varies for wildetype K8WT/K18WT cells from 43 to 505 Pa, which is roughly a factor of 100. The merged data do not show two different populations of cells as expected, neither in absolute elastic moduli nor in elastic modulus profile characteristics. Cell heights are similar for both phenotypes, which assures no systematic deviations due to 3D curvature (see section 4.6.2).

It is concluded, that the cell to cell variation of the elastic modulus of one population overrules the absolute effect of the keratin difference between wildtype K8WT/K18WT and mutant K8SE/K18WT keratin phenotypes. Nevertheless, the data give a range for the elastic modulus of Panc-1 cells. Over the nucleus, elastic moduli from 50 to 500 Pa are measured and in

the cell periphery the elastic modulus mostly decreases and measures 5 to 300 Pa. The higher modulus over the nucleus area is, most probably, a result of the much stiffer underlying nucleus itself. In literature, it is reported that the nucleus is 3 to 10 times stiffer than the cell cytoplasm [Gui00, Paj07, Cai02]. The cytoplasm surrounding the nucleus might buffer this effect and the nucleus might just be pressed downwards during indentation.

As no data for elastic moduli of Panc-1 cells exist, a comparison with another epithelial cell type is given. Breast epithelial cells showed in AFM indentation studies elastic moduli from 250 to 750 Pa for MCF-10A cells and 150-500 Pa for cancerous MCF-7 cells [Li08]. Values were obtained only from indentations over the nucleus area and evaluated with the Hertz model.

5.4.3 Biological Artifacts

The possible errors that arise due to biological phenomena are discussed here. This, in principle, unpredictable error source overlaps with the determination of statistical and systematic measurement errors. Two biological error sources are identified, but can only be assessed in a qualitative way.

One error source is the variability of the keratin intermediate filament phenotype expression. Cells are either classified as a K8WT/K18WT or a K8SE/K18WT phenotype upon the transfection with the corresponding DNA. As figure 5.6 shows, the ensemble of cells on the contrary, has a wide distribution and not a clearly defined phenotype. Thus, one can also argue that this variation is overruling the difference between the two examined phenotypes.

Another error source is the active cell response to its environment. After probing cells repeatedly, it was found that cells actively reorganize their keratin network as well as their shape after 1 to 2 hours as shown in figure 5.7. Active reactivity on this timescale is reasonable, considering a keratin filament inward movement velocity of ca. 0.2 μm/min [Bus08]. For this reason, only the first indentation profile on a cell was used for data evaluation in section 5.4.2 to minimise this error source. Findings for the change in elastic modulus over time to a strengthening or weakening were inconsistent and would need further observation. It is assumed that the active cell response is triggered by the mechanical stimulation through indentation testing or even while sample mounting. Mechanotransduction and change in keratin cytoskelelton has already been observed. Shear flow induced an enhanced and more homogenous keratin network in alveolar epithelial cells [Siv08, Siv09]. Cyclic stretching induced compaction and wrinkling in the keratin network of keratinocytes [Rus04]. The fact that mechanotransduction is not limited to keratin, but has great influence to the actin cytoskeleton, adds another errors source, which can not be directly observed during indentation experiments.

5.5 Quasistatic Indentation of the Keratin Network of Pancreatic Cancer Cells

5.5.1 Keratin Network Mesh Characteristics

The SEM is able to resolve structures of several nanometers, which is sufficient for the approximately 10 nm thick keratin intermediate filaments. For tracking transfected cells, etch gridded and numbered glass slides[18] are used which allow for cell observation before and after critical point drying and sputtering in an optical microscope as well as with the SEM (see figure 5.8 (a)-

[18] Gridded glass slides, Science Services

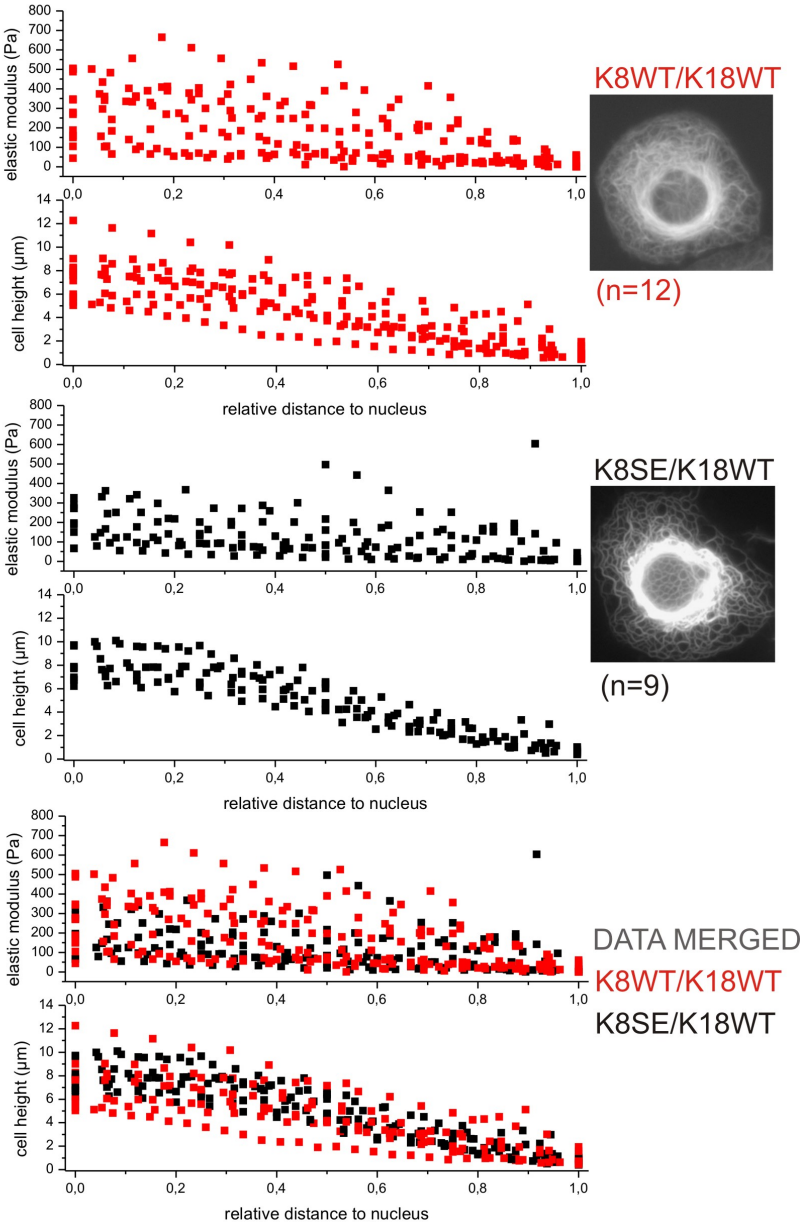

Figure 5.5: Elastic modulus profiles and heights of living K8WT/K18WT and K8SE/K18WT Panc-1 cells. The data are plotted over the normalized cell width. Merged data are shown in the bottom graph. A high cell to cell variation is seen and a difference between populations of K8WT/K18WT and K8SE/K18WT Panc-1 cells is not significant.

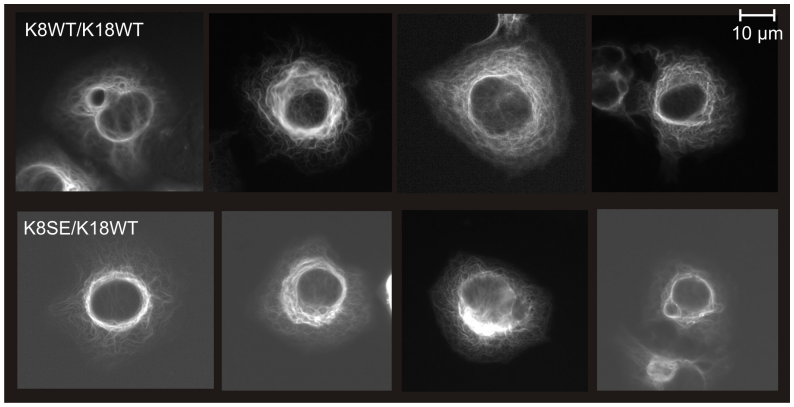

Figure 5.6: Variability of expression of K8SE/K18WT and K8WT/K18WT keratin network phenotypes. The upper row shows samples of K8WT/K18WT transfected cells. The lower row of K8SE/K18WT transfected cells. (compare to figure 5.1)

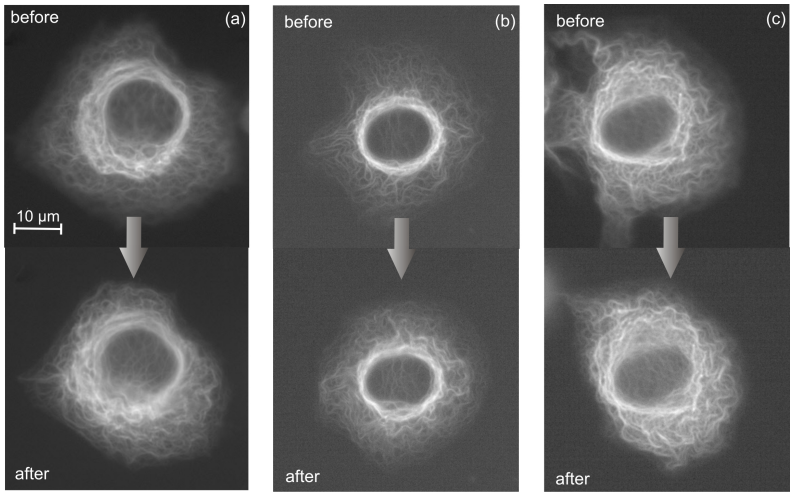

Figure 5.7: Change of the keratin intermediate filament network upon several indentation experiments. The cell actively responds to its environment and changes over time.

(d)). Several cells were observed in low and high magnification with SEM. The fiber thickness was determined to be 15 to maximum 30 nm (see figure 5.9), including the 5 nm gold sputterd on top of the cells. Compared to non-transfected cells, no significant differences in fiber thickness were observed for K8WT/K18WT phenotype cells. The meshsize showed no obvious variation throughout the cell (see figure 5.8 (e)-(i)). Quantitative meshsize determination is difficult because a 3D mesh is displayed in a 2D image. Hence, only the minimum and maxium 2D meshsize areas were determined to be 0.006 and 0.062 μm^2 (see Figure 5.9). This is two to three orders of magnitude smaller than the mean projected circular contact area of approximately 12 μm^2 between the indenter and the keratin network, and assures that the network properties rather than single fiber properties are measured. Optical images of the fluorescently labelled keratin network revealed a much larger apparent meshsize. Presumably, this is a depth effect, where intensities from the depth of the optical image are summed up, while the SEM is only scanning the exposed surface and no underlying structures.

5.5.2 Keratin Network Elastic Moduli and Influence of Keratin Network Density

Indentation testing in a straight line profile, as described for living cells, was performed with keratin networks extracted from living K8WT/K18WT and K8SE/K18WT Panc-1 cells .

For a first comparison between living cells and their keratin network, it is shown how deep the keratin was indented for a certain force compared to a cell, using the same indenter shape and size. Figure 5.10 shows the measured heights and the indentation depths at 250 pN and 500 pN applied force for a K8WT/K18WT keratin network sample and a living K8WT/K18WT Panc-1 cell. The keratin is obviously softer than the cell. It is indented deeper for the same applied force.

Going into a detailed analysis, the quasistatic elastic profile (see figure 5.12) of the keratin intermediate filament network from a wildtype K8WT/K18WT cell was obtained in the same way as described for living cells. The height profile and the corresponding fluorescence image of the keratin network are shown in figure 5.11. The maximum elastic modulus that is measured over the nucleus area is 8 Pa. Compared to the median for living cells at the nucleus region, revealing 275 Pa, this is a factor of 30 smaller, which translates to a percentage of about 3%!

Several K8WT/K18WT keratin network profiles are plotted in figure 5.13, revealing an elastic modulus range on the nucleus from 3 to 40 Pa with a median of 14 Pa, in the area of the cell periphery, the elastic modulus of the keratin network is below 10 Pa. Comparing the median of living cell elastic moduli with the keratin elastic moduli on the nucleus and at 0.6 relative distance to the nucleus in the cell periphery, this reveals a ratio $E_{keratin}/E_{cell}$ of 5% and 2%. For the K8SE/K18WT keratin network, in the nucleus region, elastic moduli from 8 to 32 Pa are measured. In the periphery it is again less than 10 Pa. Additionally, the maximum values are no longer over the nucleus region, but close around the nucleus region and reach up to 65 Pa. This is attributed to the denser network in the ring structure in K8SE/K18WT keratin.

In comparison, the storage modulus of the in-situ keratin intermediate filament network of alveolar epithelial cells has been measured with microrheology particle tracking after removing the cell membrane and other cell components [Siv08]. It was also shown, that the storage modulus increased with network density. Measurements yielded storage moduli at 1Hz ranging from 95 to 335 dyn/cm^2, which translates to an elastic modulus of 30 to 110 Pa. These values are slightly higher, but on the same order of magnitude (see figure 5.13), which confirms the values obtained by AFM indentation testing.

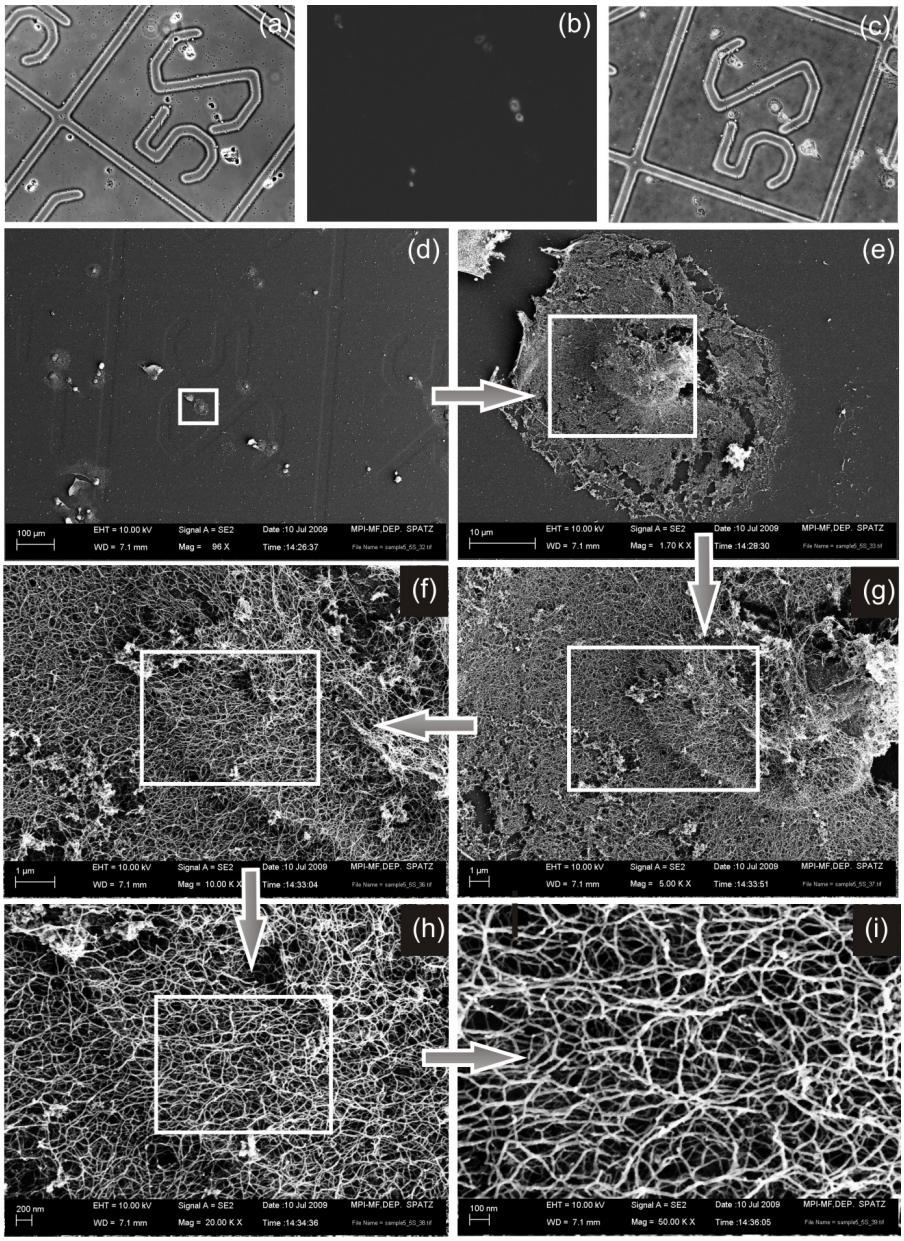

Figure 5.8: SEM images of keratin network of a K8WT/K18WT Panc-1 Cell. (a) Optical image of living cells. (b) Fluorescence image of (a). (c) Optical image of same region as (a) after critical point drying. (d)-(i) SEM images of Keratin from K8WT/K18WT Panc-1 Cell in different magnifications

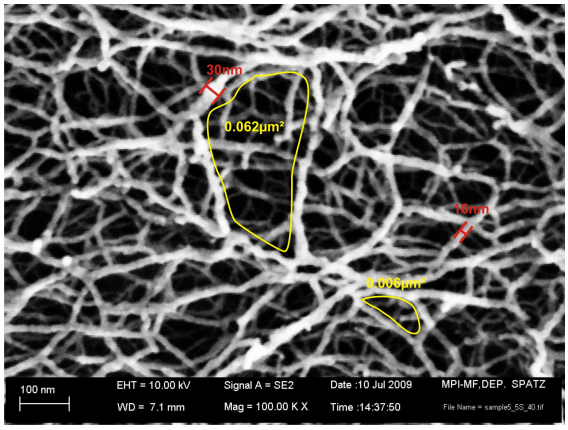

Figure 5.9: High magnification SEM image of keratin network from K8WT/K18WT Panc-1 Cell. The minimum and maxium keratin network meshsize as well as fiber thickness are marked.

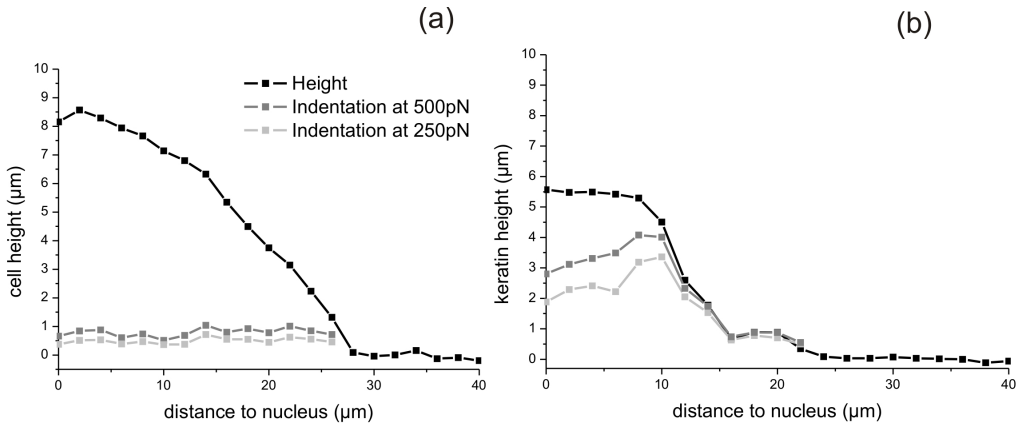

Figure 5.10: Comparison between cell and keratin network via indentation depths at a constant force. (a) Height and indentation depths of living K8WT/K18WT Panc-1 cell. (b) Height and indentation depths of Keratin of K8WT/K18WT Panc-1 cell.

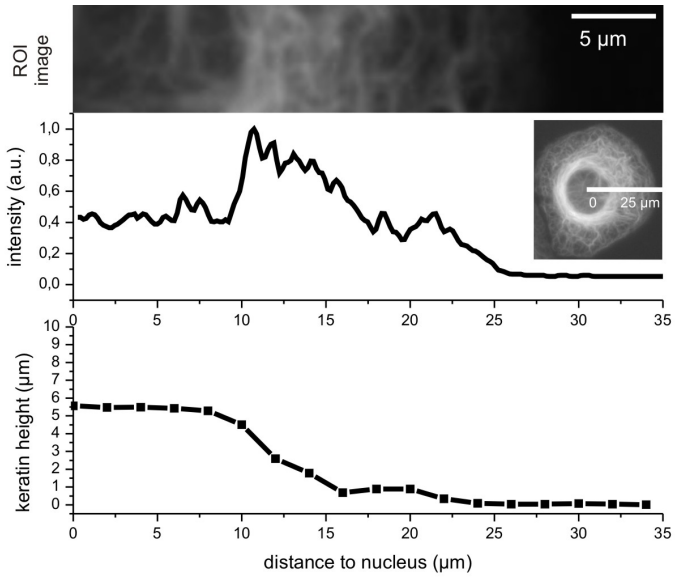

Figure 5.11: Height profile and corresponding fluorescence intensity of extracted keratin of a K8WT/K18WT Panc-1 cell.

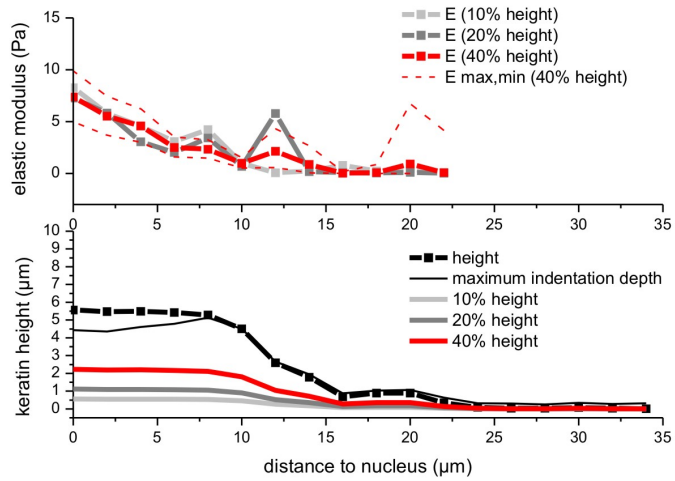

Figure 5.12: Height profile and elastic modulus profile of extracted keratin network of a K8WT/K18WT Panc-1 cell.

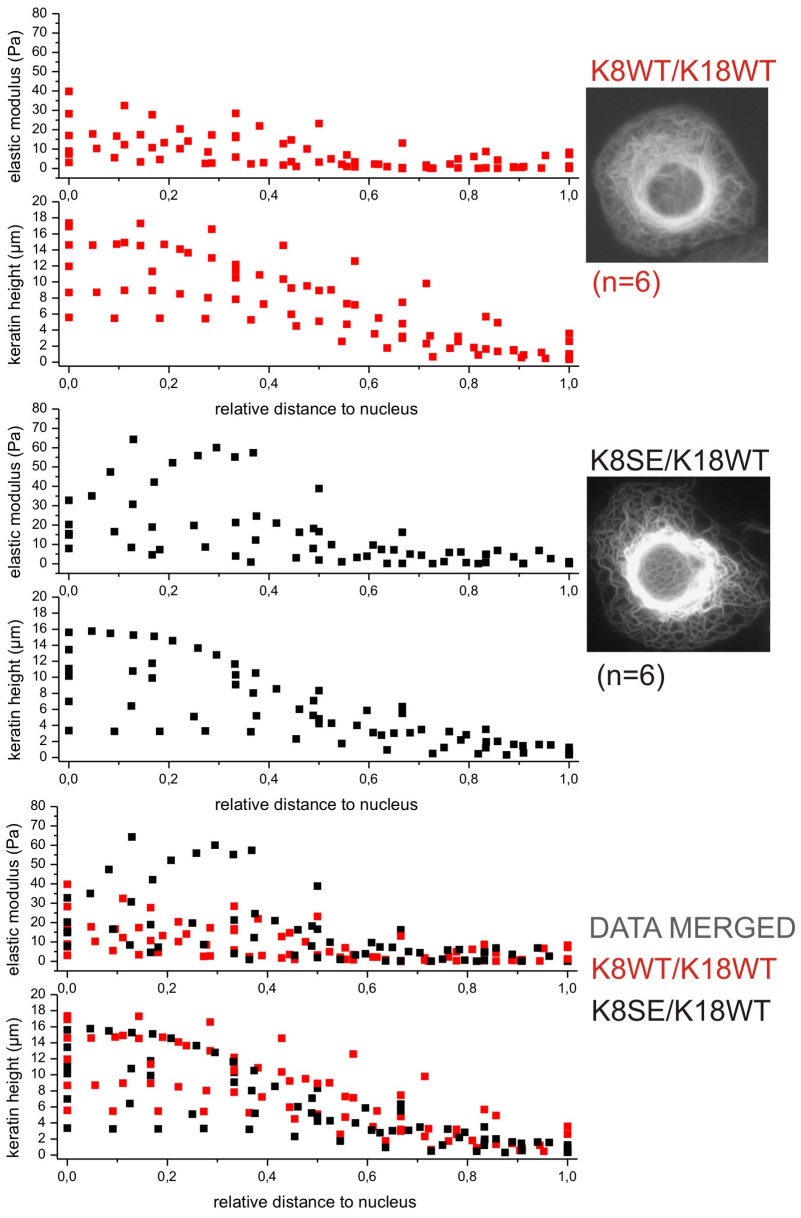

Figure 5.13: Elastic modulus profiles and heights of extracted keratin networks of K8WT/K18WT and K8SE/K18WT Panc-1 cells. The data are plotted over the normalized keratin network width. Merged data are shown in the bottom graph.

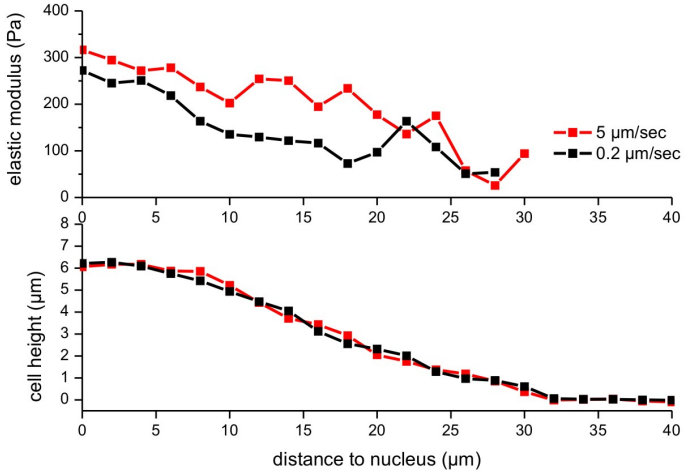

Figure 5.14: Cell height and elastic profile for fast and quasistatic indentation in comparison. The apparent elastic modulus is higher for fast indentations.

5.6 Fast Indentation and Force Relaxation of Pancreatic Cancer Cells

5.6.1 Effective Elastic Modulus and Force Relaxation

The elastic approximation is a useful method for comparing materials with mainly elastic responses. However, time dependent materials properties are specific to living cells and biopolymer networks as the keratin. In this section, it will first be shown that the elastic approximation of cells at low indentation speeds is valid, and, second, time dependent materials models will be presented and discussed. At fast indentations with driving speeds of 5 μm/s, 25x faster than the quasistatic indentation speeds of 0.2 μm/s, shorter time scale phenomena will contribute to the force indentation response. The so-called effective elastic modulus for fast indentation is fitted as well as for the quasistatic indention. Additionally, force relaxation behavior is observed for living cells.

For living cells, the effective elastic moduli are higher for fast indentations as shown in figure 5.14. It is obvious that the difference of quasistatic and fast elastic modulus varies over the cell body. Additionally, a strong force relaxation is seen for fast indentation as shown in figure 5.15. As for the elastic modulus, the force relaxation behavior is a function of specimen height and indentation depth and dependent on the material model.

5.6.2 Time Dependent Material Responses

Several time dependent materials model are proposed for cells (see section 1.3.2). Some decribe the time dependent reactions by an arrangement of springs and dashpots, resulting in an exponential decay and a characteristic time. Others describe cells with a power law which, in turn, suggest a variety of intrinsic timescales. Another model, which has recent attention is to see the cell as a poroelastic material, which has been used for soils earlier. There, the cell is

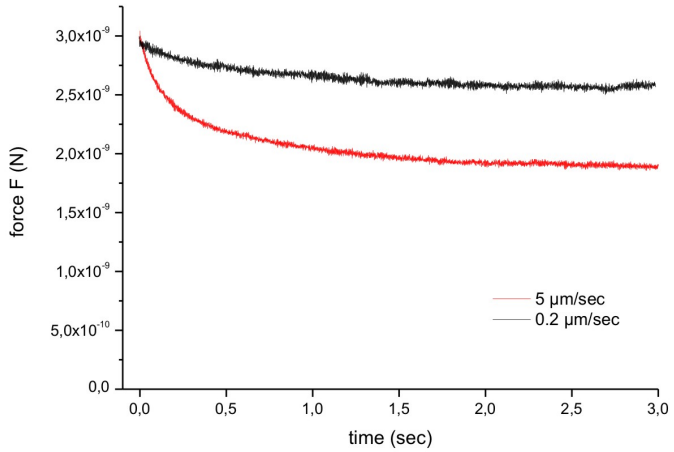

Figure 5.15: Comparison of force relaxation curves for quasistatic and fast indentation at one indentation point on the cell at the same cell height. A stronger force relaxation is seen for higher indentation speeds.

approximated as a fluid filled porous medium, where the hydraulic pore resistance, pore size, network elasticity and fluid vsicosity determine the cell material properties, which seems like a more reasonable approach from the microstructural point of view, than a spring and a dashpot. Unfortunately, no analytical solution for spherical indention and relaxation is available for thin layer poroelastic materials. Thus, in this study, the force relaxation data are first checked for a power law time dependence and further evaluated with the standard linear solid model in order to roughly quantify the elastic fraction distribution over the cell body profile.

Plotting the relaxation curves in a double logarithmic scale, reveals a power law behavior up to approximately 2 seconds, after which a plateau is reached. The relaxation at slow indentations also shows a power law, but with a smaller exponent. Both reveal that there is not only one characteristic time, as assumed for the standard linear solid. Further the power law exponent is varying different point on the cell. This could either be a materials effect or a height effect. For example, the confinement of the underlying substrate will hinder the draining of the viscous liquid through the mesh as in the poroelastic materials picture.

The standard linear solid model, as already described in section 4.3.4 and used for quantifying time dependencies in PDMS, is applied. The standard linear solid model combined with the TLC model describes the force relaxation curves over the cell body. A characteristic time (τ), the associated viscosity (η), the instantaneous and equilibrium elastic moduli (E_∞ and E_0), and the elastic fraction (F_E) are calculated. The elastic fraction of cells is determined to be 70 to 90% and the calculated equilibrium modulus fits well the quasistatic modulus from TLC model fitting as shown in figure 5.17. The cell viscosity is in the range of 15-85 Pa·s and the characteristic times are distributed from 0.7 to 1.5 seconds. Still, it is obvious from the quality of the fit (see figure 5.18) that the standard linear solid is not an exact description of the force relaxation behavior of the cell and can only be seen as an approximation.

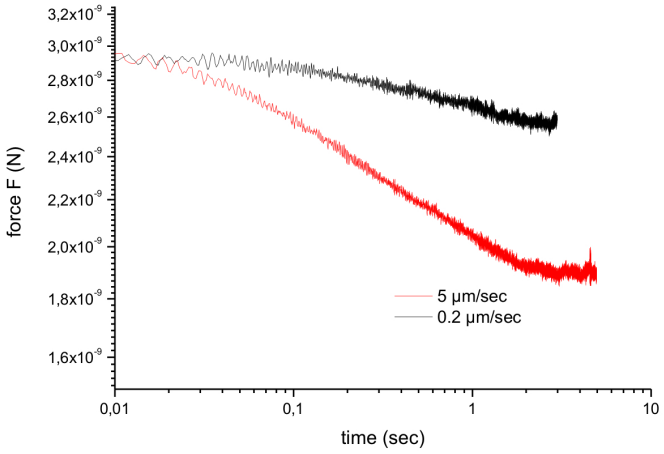

Figure 5.16: Comparison of force relaxation curves for quasistatic and fast indentation at one indentation point on the cell at the same cell height in a double logarithmic scale. The apparent linearity suggest a power law behavior of the cell.

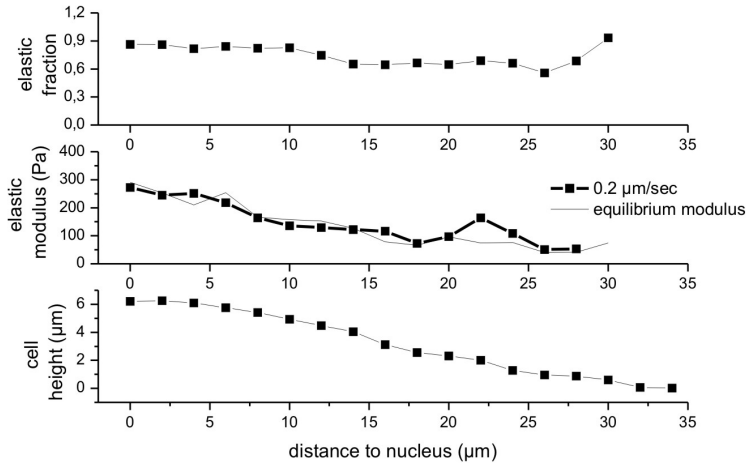

Figure 5.17: Cell height, elastic fraction and equilibrium elastic modulus over the cell profile obtained from the standard linear solid model. An elastic fraction of 70-90% validates the application of the elas´tic approximation for living Panc-1 cells.

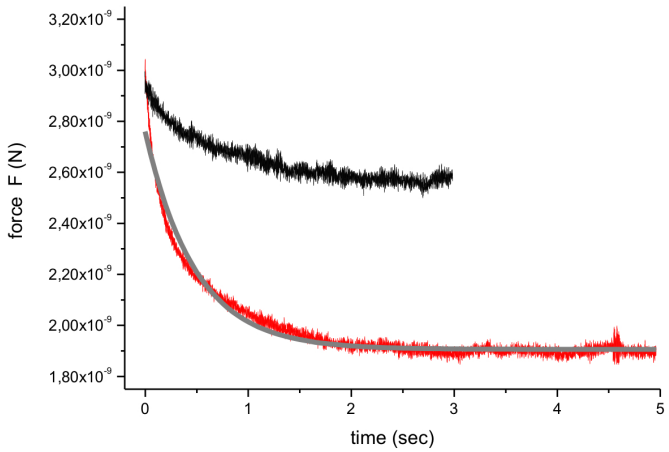

Figure 5.18: Force relaxation curve with the standard linear solid fit..

5.7 Large Strains and Keratin Network Stretching

Intermediate filaments can sustain extremely large strains and show a strain hardening behavior [Kre07, Jan91]. Strains in indentation testing are limited by cell height. Strain in stretching is, in principle, not limited.

Keratin network stretching and rupture events were observed during retraction of the indenter (see figure 5.19) because nonspecific adhesion and fiber anchorage at the contact area occurred. It was observed that mostly the whole network was affected during stretching, where the pulling only occurred at the contact area between the sphere and the network. Rupture events are thus probably detachment of the nonspecific adhesion spots rather than the rupture of filament crosslinks or single fibers.

However, only a semi-quantitative evaluation is possible. A low resistance to stretching is seen up to a retraction distance of 3 μm, followed by a drastic increase in force for larger retraction distances up to 8 μm (see figure 5.19). Approximating the low and high resistance regions with a linear spring, it reveals spring constants of 0.3x10^{-3} N/m and 1x10^{3} N/m. For comparison, indentation testing was only evaluated up to a maximum of 4 μm indentation depth, revealing a spring constant of 0.5x10^{-3} N/m, including the substrate effect.

To summarize, these qualitative findings show the robustness of the keratin network during large scale cell stretching and strain hardening with tensile stress.

5.8 Conclusions to the Importance of the Keratin Intermediate Filament Network in Pancreatic Cancer Cells

A direct comparison between the elastic modulus of living cells and their extracted keratin networks in figure 5.20 shows that the keratin is clearly softer than the living cell. Comparing the medians of living cell elastic moduli profiles with the keratin elastic moduli on the nucleus

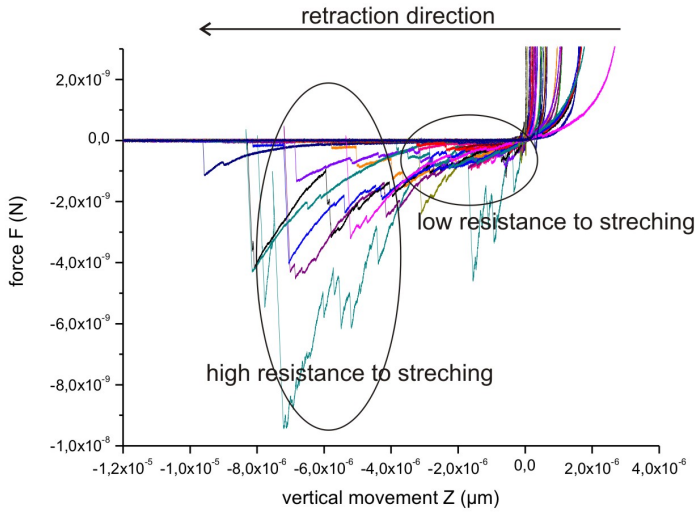

Figure 5.19: Retraction curves after keratin indentation showing network stretching and rupture events. An overproportional increase of force during stretching response is seen.

site and at 0.6 relative distance to nucleus in the cell periphery, reveals elastic moduli ratios of only 5% and 2%. The same methodology of probing was used for the keratin network and for the cells. Thus, artifacts due to different testing equipment and different materials models are excluded and elastic moduli are directly comparable. However, artifacts due to the extraction treatment are possible. On the other hand, an absolute comparison with another study on cellular keratin networks shows good agreement, i.e. values for the keratin elastic modulus are in the same order of magnitude [Siv08], and thus confirms the AFM indentation testing.

The weak mechanical impact of keratin network density inside living cells was supported as a significant difference of the elastic modulus between K8WT/ K18WT and K8SE/ K18WT Panc-1 cells for local indenation is not detected. The elastic moduli were not correlated with the keratin network densities in living cells. Cell to cell variations of the elastic modulus up to a factor of 100 were observed and suggest rather an effect which is not associated with the keratin network.

As the conducted experiments did not lead to a conclusive and positive result about the importance of the keratin in cell mechanincs, as expected from previous publications [Bei04, Mic04, Sur05], the complexity of the problem is examined in the follwing and suggestions for further experiments are made. In addition to indentation testing, during large strain stretching of the keratin network, a strong overproportional response to deformation was seen. This fits very well into the picture of intermediate filament behaviour of being robust to large tensile strains. However, the performed indentation testing was also on a large scale as the deformation was in the micrometer range which is in the order of the cell size. Coming back to the original question of the importance of the keratin network during cell migration, another experimental approach is suggested for further work to clarify the keratin deformation mechanisms. The keratin network deformation during active migration through microchannel restrictions should be observed in high resolution time lapse imaging in order to justify, if there is a passive deformation or an active new formation of the keratin network. The active keratin network reorganisiation upon mechanical stress during indentation on the timescale of cell migration was also observed in this thesis. Further, it would be of interest to directly measure pressures that a migrating cell

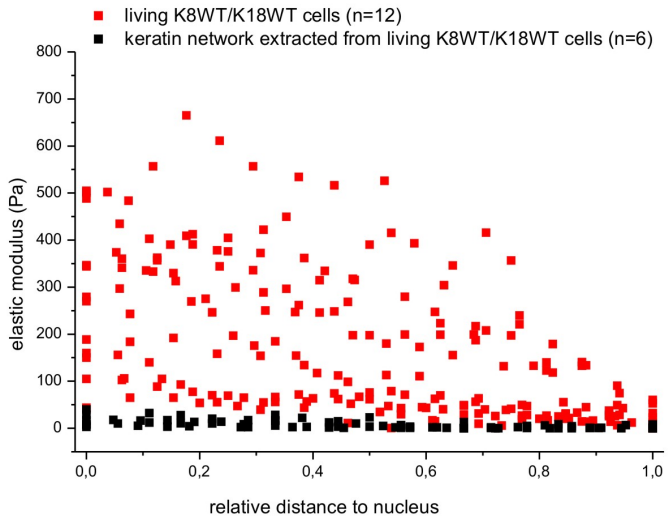

Figure 5.20: Comparison between keratin and living cells of K8WT/K18WT phenotype. The keratin network is clearly softer.

is exerting on the surrounding tissue during active deformation. The microflap restriction technique (see chapter 8), which was originally developed in this thesis for suspended cells, would be suitable for this.

Part III

Compression of Suspended Cells inside Microchannels

Chapter 6

Microfluidic Restrictions as a Tool for Cell Mechanical Testing

6.1 Introduction

This chapter provides an introduction for the next chapters 7 and 8. In particular, the technique of using restrictions in mirofluidic channels for cell mechanical testing is introduced and motivated. The basics on cell mechanics and frictional processes that occur during passive cell deformation in microrestrictions are discussed. Eukaryotic, non-circulating, cells are the main focus here in contrast to, for example, circulating blood cells.

The two different experimental attempts of microchannel restrictions and the novel microflap restrictions are presented. The evolution of the project from microchannel restrictions to cantilever-based force measurement with microflaps, as this is no standard technique for cell mechanical probing, is emphasized. Further, the experimental design and design considerations are described as well as the basic experimental set-up and the production of the utilized flow cell chips.

6.2 Biological and Materials Science Objectives

Two main aspects were motivating Part III of this thesis: (i) the use of microfluidics as a high throughput cell mechanical testing device and (ii) as a device for mimicking cell deformation in vessel systems inside the body.

Mimicking the physiology of e.g. blood vessels is obviously of interest for circulating blood cells. For the deformation of suspended cells, which are normally adherent, it is relevant in transportation of metastasizing tumor cells in the blood circulation or the lymphatic system. The tumor cells get stuck in small capillaries and invade the tissue (see section 2.3). Cell mechanical aspects play a role then and might determine metastatic behavior.

As a biomechanics testing tool, microfluidics is a new field [Van09]. Compared to other techniques, as micropipette aspiration [Hoc00], production is simple, easy to reproduce and cost effective. Further, it has the potential for high throughput performance. As first attempts, the dynamics and deformation of blood cells while passing through narrowing channels have been investigated, where restriction entry time, transit times and shape are indirect measures of cell

mechanics [Ani08]. This revealed for example the fact, that malaria diseased cells get stuck more easily than healthy red blood cells. The maleria causing parasites stiffen the cell and change their adhesion behaviour, which is in turn suggested as the reason why organs are clogged with blood cells and thus maleria is lethal [Ani08, Sur05]. Further, a study on diseased leukemia cells shows increased channel transit times compared to a healthy reference [Ros08b]. These testing concepts have also been used for non-blood cells. It has been shown that metastatic MCF-7 breast cancer cells can enter more easily into restrictions than healthy MCF-10A cells, but slide at the same velocity trough the channels [Hou09]. All examples of using microfluidic restrictions as cell mechanical testing tool give physiological explanation for the disease pattern and further a possibility for disease detection on a cell mechanical basis.

In this project, narrow capillaries are mimicked through PDMS fabricated microchannels and a syringe pump. It is sought to quantify cell mechanics for non-blood cells and to reexamine and improve the known applications of microrestrictions. Sliding behavior of deformed pancreatic cancer cells (Panc-1) squeezing through long microrestrictions is observed, which is indirectly connected to cell mechanics via the normal forces that a cell exerts on the channel walls. However, these data are corrupted by processes such as frictional resistance and driving pressure. Thus, in this work, a new direct method for quantification of cell deformation inside microchannel restrictions is developed. A flexible flap is incorporated in the microrestrictions and serves as a deformation sensor. Cell deformation dynamics during extremely fast cell deformation (μs) in a 2D confinement is observed and forces that the cells exert on the channel walls are directly measured.

6.3 Cell Mechanics and Cell-Wall Friction in Microrestrictions

The process of a cell entering a smaller capillary can be separated into two stages: (i) deformation of the cell in order to fit through the new geometry and (ii) sliding of the cell through the restriction (see figure 6.1). The deformation resistance of the cell is connected to the cells apparent material properties at the timescale of deformation, which is in turn determined by the applied flow in the capillary, and the amount of deformation. These are elastic and time-dependent responses, possibly plastic deformation and actin fluidization. The compression ratio (see section 6.5.1) at which the cell components, e.g. cytosol, membrane and nucleus, are deformed also plays a role for eukaryotic cells. The created contact pressure or normal forces (F_{normal}) reflect the cells materials properties. Further, a rearrangement of subcellular components possibly occurs. Sliding of the cell in a constant geometry, no longer needs energy to deform the cell but rather force relaxation processes will contribute.

For monocytes, a type of white blood cells which have a nucleus, it has been shown by using microchannel restrictions, that actin disruption or stabilisation has a significant influence on the time the cells need to squeeze into a channel as well as on the sliding velocity [Gab09]. This indicated that no complete actin fluidisation was present nor the cell nucleus was the main mechanical resistance during deformation. Additionally, it was found that successive deformation was facilitated because of a slow shape relaxation, which was interstingly not dependent on actin disruption or stabilisation. Micropipette aspiration on neutrophils, another type of white blood cells with a multilobed nucleus, in contrast, suggested a shear thinning or fluidisation behaviour when the shear rate exceeded a certain limit [Dru01]. Further, for epithelial breast cancer in comparison to healthy cells, a difference for the time to squeeze into microchannel restriction was observed, where the cancerous cell line was faster [Hou09]. However, for these cells no difference during cell sliding was observed, which either suggests a fluidization process or a very small difference in frictional resistance.

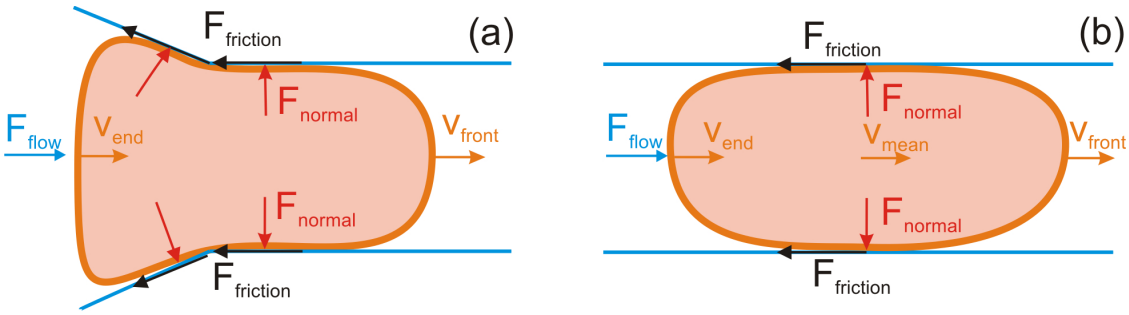

Figure 6.1: Sketch of forces during deformation and sliding. (a) Cell deformation during entrance and squeezing into the the channel restriction. (b) Cell during sliding in constant cross section. The force arrows are not a point force but represent pressure distributions.

It is thus concluded here, that the cell mechanical response and fluidization upon cell shearing, in particular, depends strongly on deformation and shear rate, as well as possibly on cell type. Different actin and other cytoskeletal protein concentrations as well as the nucelus to cytosol dimension proportion might determine the specific cell mechanical response. Further, it needs to be differentiated between the case of dominant driving forces (see equation 6.1) and when friction forces ($F_{friction}$) or differences in friction forces are in the same order of magnitude as driving forces (F_{flow}) (see equation 6.2) and thus are detectable. Only in the latter case, the observation of cell sliding in restriction is relevant for the measurement of cell mechanics or respectively differences in cell mechanics.

$$F_{friction} \ll F_{flow} \ , \ \Delta F_{friction} \ll F_{flow} \tag{6.1}$$

$$F_{friction} = O(F_{flow}) \ , \ \Delta F_{friction} = O(F_{flow}) \tag{6.2}$$

Frictional forces that occur at the contact area during sliding will slow down the cell. The friction force will be dependent on the contact pressure that the cell exerts to the channel wall, the flow that drives the cells through the channels and how the pressure distribution, shear rate and sliding velocity ($v_{sliding}$) is correlated to the frictional resistance (see equatio 6.3]). The functional relationship will differ for specific adhesion, brushlike structures on the cell surface or pure vicous lubrication layers. All cases can be present for cells. The change in frictional forces as a function of normal forces is the important functional relation for indirectly detecting cell mechanics during cell sliding (see equation 6.4).

$$F_{friction} = F_{friction}(F_{normal}, v_{sliding}, ...) \tag{6.3}$$

$$\Delta F_{friction} = \frac{dF_{friction}}{dF_{normal}} \Delta F_{normal} \tag{6.4}$$

6.4 Design of Microchannel Restrictions and Microflap Restrictions

In order to quantify cell deformation of suspended cells during deformation in a narrow restriction, two different studies were designed.

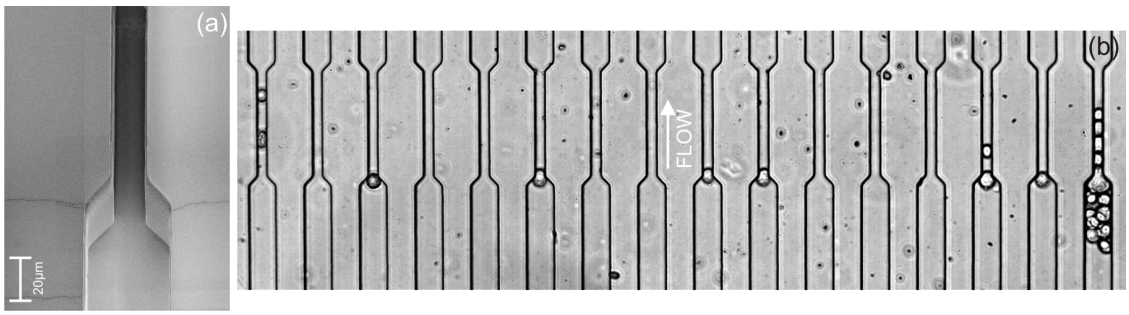

Figure 6.2: Long microrestrictions implememented in PDMS flow cell chip. (a) SEM image of one microchannel.(b) Cells before, during and after passing the long restrictions.

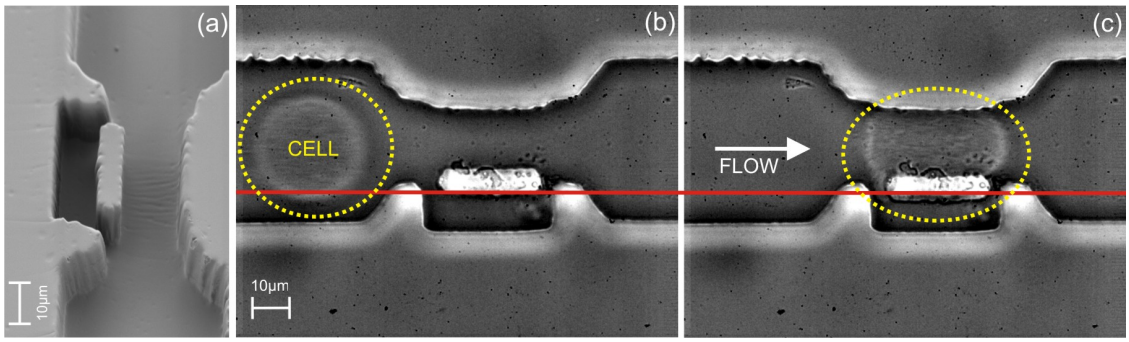

Figure 6.3: Microflap implemented in PDMS flow cell chip. (a) SEM image of one freestanding microflap.(b) Top view of cell approaching restriction with microflap.(c) Cell and microflap deformation during cell transit of restriction.

For studying the deformation and sliding dynamics of cells, long microchannel restrictions (see figure 6.2) are used. This has already been applied for red blood cell studies [Sur05] and breast cancer cells [Hou09]. Entrance time and sliding velocity during cell movement into and through restrictions are observed and used as an indirect measure for mechanical properties. The experiments are presented in chapter 7.

Second, a cantilever-based force sensor is implemented in a flow cell chip for absolute cell deformation force measurement as shown in figure 6.3. When a cell enters the restriction with the flexible flap, the flap bends due to a force and the deflection is recorded (see figure 6.3b and c). Deformable PDMS flaps or walls have been used as a microfluidic diode [Ada05] and flow sensor [Lov07] but never as a cell deformation sensor. The direct assessment of deformation forces is independent of frictional forces and driving forces and thus overcomes experimental uncertainties arising from frictional processes and driving pressure variations (see section 6.3 and 6.6.3).

The two experimental approaches have the same basis and are implemented in a two reservoir flow cell chip (see figure 6.4). Sixteen parallel channels connect the two reservoirs, with each channel having one microflap or one microrestriction. Flow is induced via a syringe pump, which drives the cells through the channels into the restrictions (see section 6.6.3).

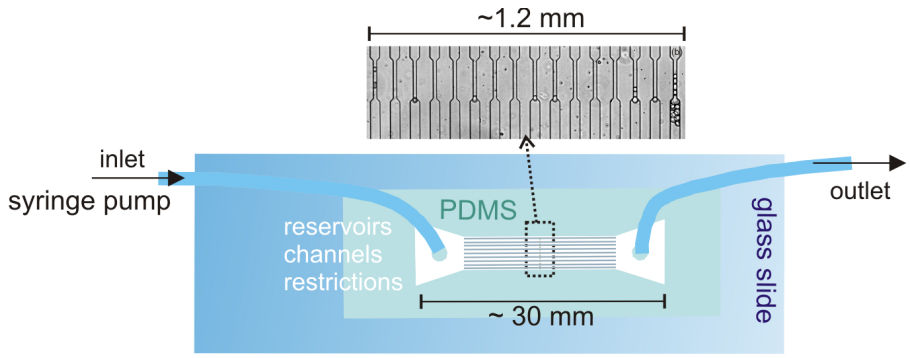

Figure 6.4: Sketch of macroscopic flow cell chip. The PDMS flow cell is bonded on a thin microscopy glass slide and fits on every conventional microscope. Channels are arranged in parralell with common reservoirs as shown in the sketch. Through tubings, the flow from a syringe pump is applied.

6.5 Geometric Considerations on Cells and Microrestrictions

6.5.1 Cell Deformation Ratio

It is obvious that the microrestriction technique is not universal for all cells. Restriction dimensions have to be adjusted for each cell line. In order for the cell to be deformed, the restriction needs to be smaller than the cell. The deformation ratio was defined here as the ratio of the channel width to the round cell diameter. In case of a two dimensional compression, i.e. height and width of the channel restrictions are smaller than the cell diameter, the compression ratio was defined for each dimension. Further, for eukaryotic cells, the compression ratio determines which cell component, e.g. nucleus or cytosol, is compressed and thus probed.

6.5.2 Cell Size Distribution

Suspended cells of normally adherent cell types have an almost round shape, no actin stress fibers and fewer cytoskeletal structures than in the adherent state (see section 1.2.2). The diameter of suspended Panc-1 cells is measured after trypsinisation in solution with brightfield microscopy. The cells have a mean cell diameter of 22.5 μm as shown in figure 6.5.

Restriction sizes have to be adjusted to cell size and the desired amount of deformation. Having a restriction cross-section of 15 μm x 15 μm , a Panc-1 cell with a mean diameter of 22.5 μm will be compressed by 7.5 μm in two dimensions. This translates to 33%. In a size-varying cell population, different compression levels will be imposed.

6.5.3 Number and Size of Nuclei

The nucleus is mechanically more stable than the cytosol [Gui00, Paj07, Cai02] and retains an elliptical shape even in suspended cells (see figure 6.7a). The long and short axes of the nucleus are determined in spread cells. Figure 6.6 shows that the longer axis is in the range of the mean cell diameter (compare figure 6.5). This gives rise to the fact that the long axis of the nucleus determines the cell size and might be the reason for deviation from the round droplet shape of some suspended cells. Nevertheless, one needs to be careful with the data, because the nucleus

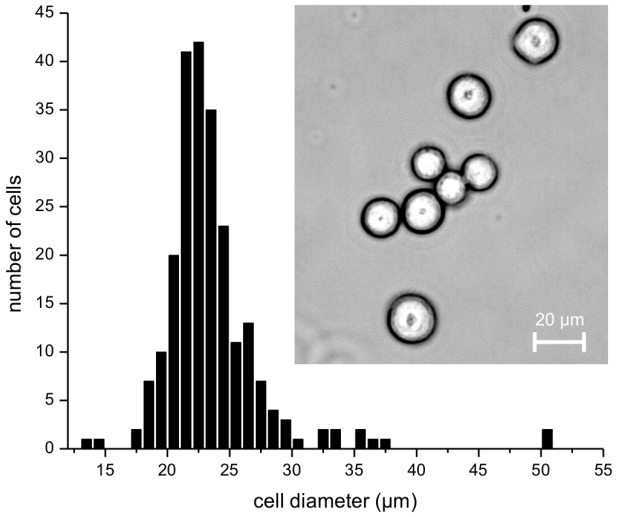

Figure 6.5: Distribution of diameters of suspended Panc-1 cells. The inset shows an image of a suspended round cell sample.

is prestressed by the cytoskeleton in spread cells [Jea04]. This is supported by the finding that nucleus size and spreading area correlate and the nucleus size decreased during trypsinisation. Thus, the obtained nucleus dimensions can be seen as an upper limit. With a restriction cross-section of 15 μm x 15 μm , a Panc-1 cell nucleus with the smallest length dimension (short axis) of approximately 17 μm will be deformed and will contribute to the mechanical response.

Panc-1 cells are multinucleated cells [Lie75], i.e. they can have several nuclei per cell (see figure 6.7). Interestingly, it is known that the pathological appearance of cancer cell cultures are, in certain cancer types, correlated to multinuclear cells [Pad03]. However, during cell squeezing experiments it was not possible to observe the nucleus or the number of the nuclei.

6.5.4 Excess Surface Area

During deformation, the surface to volume ratio of the cell changes and additional membrane area has to be provided. Suspended cells have a membrane reservoir stored as surface wrinkles. The so-called Excess Surface Area (ESA) determines the deformation limit for instantaneous shape change before rupturing occurs. It was defined here as the ratio of surface area of cells swollen in deionized (DI) water ($A_{sph,DI}$) to the surface area of normal cells ($A_{sph,N}$) (see equation 6.5). The cells were approximated as a sphere with a diameter D_{sph}.

$$ESA = \frac{A_{sph,DI}}{A_{sph,N}} = \frac{\pi D_{sph,DI}^2}{\pi D_{sph,N}^2} = \left[\frac{D_{sph,DI}}{D_{sph,N}}\right]^2 \tag{6.5}$$

Figure 6.8 shows the difference in Panc-1 cell diameters for normal and osmotically swollen cells. For Panc-1 cells a mean ESA of 3.34 (+/-4%) was found. The ESA was calculated using the peak values of the cell diameter distributions.

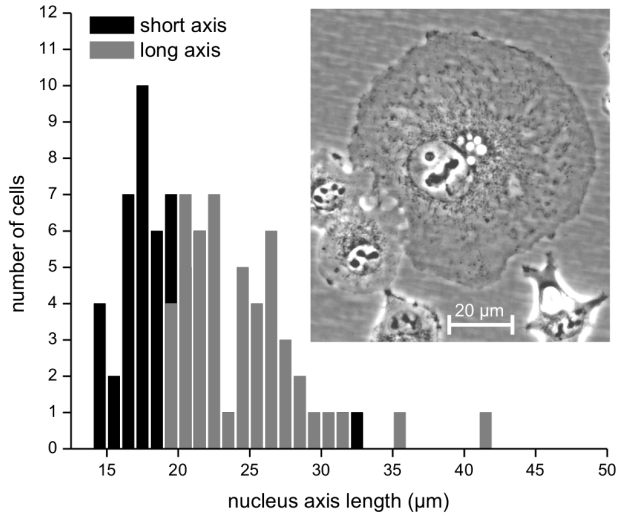

Figure 6.6: The nucleus is approximated as an ellipse. The distribution of the long and short axis length is shown. The inset shows a spread cell with the nucleus situated near the middle of the cell.

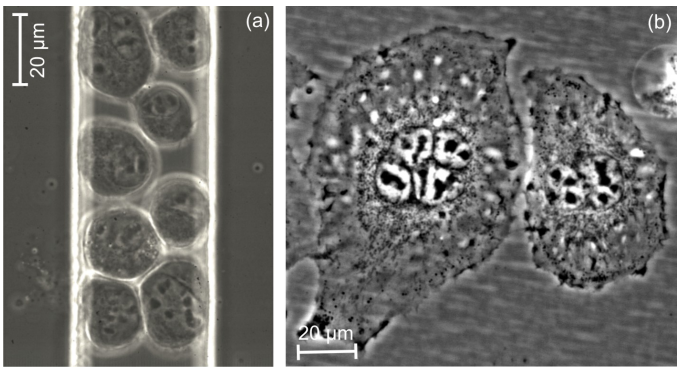

Figure 6.7: Multinucleated Panc-1 cells in suspended and in adherent cells. (a) Suspended Panc-1 cells trapped in microchannel. (b) Spread multinucleated Panc-1 cells.

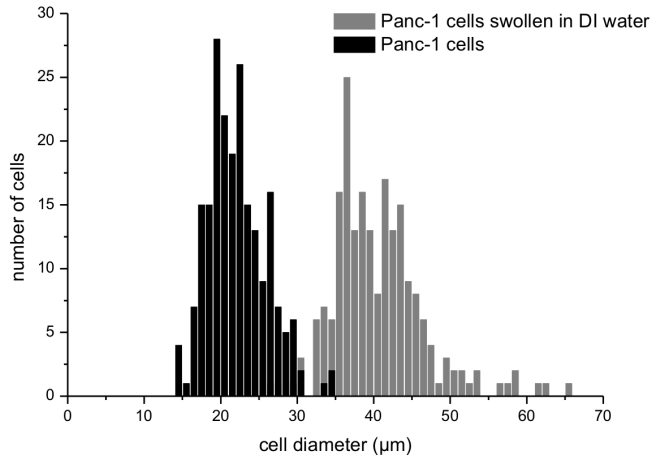

Figure 6.8: Panc-1 cell diameter distribution of normal and osmotically swollen cells.

Knowing the ESA, it was possible to estimate the minimum channel sizes that cells can transit without rupturing for a round and square channel cross-section. The higher the ESA of a cell, the smaller the transited vessels can be. For further calculations, a cell with a representative diameter (D_{sph} = 22.5 μm) is used. Volume conservation (see equation 6.6) during cell deformation from a spherical shape (V_{sph}) to a deformed elongated shape (V_{def}) is assumed for the imcompressible cell. The cell is further assumed to completely adjust its shape to the restriction as a cylinder (V_{cyl}) or cuboid (V_{cub}). The round cross section has a diameter (D_{cyl}) and a squared cross section a width (W_{cub}).

$$V_{sph} = \frac{\pi}{6} D_{sph}^3 \stackrel{!}{=} V_{def} = \begin{cases} V_{cub} = W_{cub}^2 L \\ V_{cyl} = \frac{\pi}{4} D_{cyl}^2 L \end{cases} \tag{6.6}$$

During deformation, the surface area (A_{def}) must be smaller than the maximum surface area available (A_{max}) to prevent membrane rupturing (see equations 6.7).

$$A_{max} = A_{sph} \cdot ESA = \pi D_{sph}^2 \cdot ESA \geq A_{def} \tag{6.7}$$

The surface areas needed for a cell to deform in a cuboid (A_{cub}) or a cylinder (A_{cyl}) as a function of cuboid cross-section width (W_{cub}) and cylinder diameter (D_{cyl}) are given in equation 6.8.

$$A_{def} \begin{cases} A_{cub} = 2W_{cub}^2 + 4W_{cub}L \stackrel{(6.6)}{=} 2W_{cub}^2 + \frac{4V_{sph}}{W_{cub}} \\ A_{cyl} = \frac{\pi}{2} D_{cyl}^2 + \pi D_{cyl} \cdot L \stackrel{(6.6)}{=} \frac{\pi}{2} D_{cyl}^2 + \frac{4V_{sph}}{D_{cyl}} \end{cases} \tag{6.8}$$

The problem of the critical minimum channel size is solved graphically in figure 6.9. The lower limit for a round capillary is a diameter of 4.5 μm and for the cuboid shape it is approximately the same lowest limit of 4.5 μm for the channel width. One deduction from this is that a channel width greater than 4.5 μm will not cause rupture of the cell membrane. In theory, with the lower-limit of cross-section area, the cell would have a length of about 250 μm which is more than 10 times its diameter! On the other hand, if the pressure is high enough to squeeze a cell into a

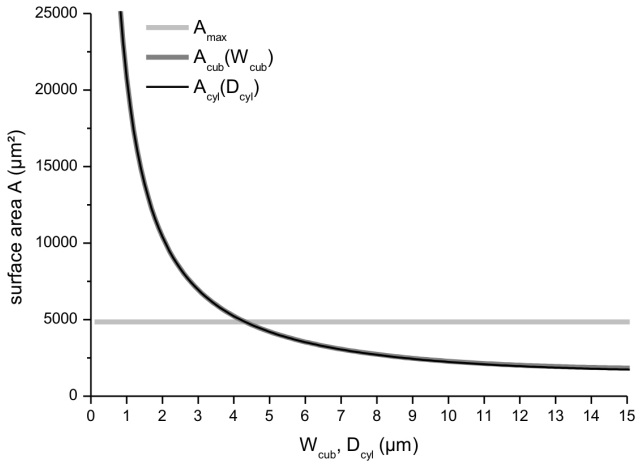

Figure 6.9: Graphical solution for minimum possible channel cross sections. The maximum surface area and the necessary surface areas for deforming in the channel are plotted as a function of channel diameter or channel width. The intersection defines the minimum channel cross section for a representative Panc-1 cell with a diameter of 22.5 μm.

cross-section that is smaller than the calculated limit, the cell will burst and is no longer able to, for example, metastasize. In this context, it would be interesting to observe the ESA of different cell types.

In qualitative compression tests in microchannels and with AFM, it was seen that the membrane does not deform homogenously as for a liquid-filled membrane and as in osmotic swelling, but rather bubble formation is visible (see figure 6.10). Mechanical deformations induce local separation of cytoplasma and membrane, which has been observed in previous studies on cell compression [Kim08]. These local membrane deformations might lead to local rupturing even before the total ESA is fully used.

6.6 Production and Setup of Flow Cell Chip

6.6.1 Production of Flow Cell Chips

The macroscopic set-up of the flow cell chips for microflaps and microrestrictions have the same basis. Both were cast of PDMS (see chapter 4.2) on an SU-8 negative mask, produced with commonly-used photolithographic techniques [Sia03, Mad97]. In brief, the SU-8 resist[1] is spin-coated on a silicon wafer at the desired thickness (15 to 40 μm), followed by a prebake. After illumination through the patterned chromium mask with an i-line spectrum (360 nm) of the maskaligner[2], the UV-crosslinked negative mask is developed after a postbake step. A hardbake is the last step of the master production.

PDMS, in a 15:1 base to crosslinker ratio, was cured on the negative master structures for 2 hours

[1] SU-8 2025, MicroChem Corp.
[2] MJB4, SÜSS Micro Tech

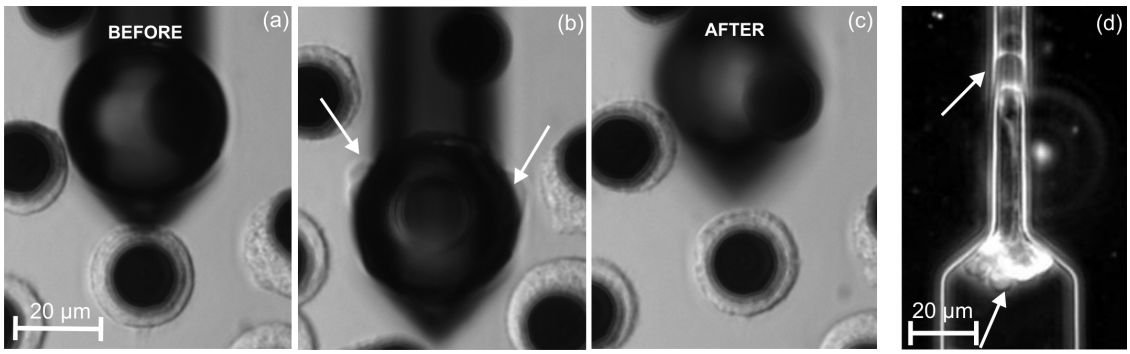

Figure 6.10: Local bulging of membrane (see white arrows) during mechanical cell deformation. (a)-(c) Before, during and after an AFM compression test with a large sphere on a round Panc-1 cell, only attached to a gold circular microstructure. The membrane was only locally deformed. (d) Phase contrast image of a Panc-1 cell squeezing into microchannel. In the front edge membrane was detaching from the cytosol. In the back edge, localized membrane bubbles were formed.

at 80°C and peeled off after cooling down to room temperature. For the microflaps, the peel off was performed in ethanol, which easily wets the PDMS, in order to not destroy the delicate flaps. If the flaps were too thin, the flaps were pulled until failure during separation of the device from the mold. Subsequently, 1 mm wholes were punched into the flow cell reservoirs using a biopsy punch[3]. Now the flow cell was plasma bonded[4] to a glass slide. Although the flap has the same height as the channels, it is not bonded to the glass slide and able to bend, presumably because of a small contact area and small contact pressure. 24 hours later, the tubing[5] is inserted into the holes, sealed with PDMS while the flow cell is heated at 80°C for fast crosslinking. Further, a drop of glue[6] is applied for a final sealing of the tubing connections. For infusing liquid into the flow cell with a syringe, blunt syringe tips[7] were fitted into the tubing.

6.6.2 Restriction Geometries

Channel and flap geometries were determined by optical microscopy and SEM. For channel height determination, the sample was sliced, tilted 90° and observed under the optical microscope.

Microchannel restrictions for cell sliding experiments (see chapter 7) have a cross section of 15x40 μm and a length of 150 μm (see figure 6.2). The delivery channels have a cross- section of 40x40 μm. Thus, the approaching cell is not compressed, while in the restriction the cell is compressed in one dimension. The compression ratio for a representative cell is 33% (see section 6.5).

The cross section in case of the microflap restriction experiments (see chapter 8) is 15x15 μm. The delivery channels have a cross-section of 15x40 μm and thus cells are already compressed in 1 dimension as in case of the microchannel restrictions. The flap itself has the dimensions of 15x25x5 μm (see figure 6.3a)). The cells are two dimensionally compressed in the microflap restrictions.

[3]Biopsy Punch (⌀ 1 mm), Miltex Inc.
[4]TePla 100E PS, PVA TePla AG (0.1 mbar O_2, 100 mW, 5 s)
[5]Tygon medical tubing S54-HL (ID 0.25 mm, OD 0.45 mm), Saint-Gobain
[6]UHU plus schnellfest, UHU
[7]Blunt Syringe Tips (31G), Transcojet

6.6.3 Flow Control with and without Cells

Flow control was appplied for the cell squeezing experiments utilizing a syringe pump[8]. This method is easy to implement and has advantages, as the simultanious injection of cells with inducing the flow, and, second of being insensitive to air bubbles inside the tubing and the reservoirs in contrast to pressure driven flows. The pushing speed and the corresponding syringe[9] diameter enables the total volume flow rate that is pumped into the flow cell to be set. Volume flow rates of 1 to 15 μl/min were applied.

The flow cells have 16 parallel channels, with the same geometry, that connect two reservoirs (see figure 6.4). The usage of the high number of parallel channels originates from the idea of a high throughput device as well as the smaller change in total flow rate in case one channel is blocked with cells or dirt. The microrestrictions or microflaps are siuated in the middle of each channel, equidistant between the reservoirs. With a known total volume flow rate (f_t) (see equation 6.9) through the channel system, and a known geometry with the hydraulic resistance (R_l), the corresponding local flows (f_l) and local pressure drops (Δp_l) in a microrestriction (see equation 6.10), can be calculated using volume conservation and the Navier-Stokes equation for the case of laminar flow, i.e. low Reynolds number flow, and no cells inside the channels [Bro96, Squ05].

$$f_t = \sum_{n=1}^{16} f_{ln} = 16 f_l \;\leftrightarrow\; f_l = \frac{f_t}{16} \tag{6.9}$$

$$\Delta p_l = R_l f_l \tag{6.10}$$

The flow resistance in a rectangular channel is a function of geometry and fluid viscosity [Mor05, Bro96]. The origin of flow resistance is friction between fluid and wall as well as internal fluid shearing. This leads to a characteristic fluid velocity profile (v_l) over the cross-section area ($A_{channel}$) which is pictured in figure 6.11 using a finite element method (FEM[10]) simulation for the microchannel restrictions assuming no-slip boundary conditions, i.e. the fluid velocity at the wall is zero, and a newtonian fluid inside the channels. Knowing the local flow velocity profile, the local flow rate can be calculated by integrating over the cross-section area of the channel and even a mean fluid velocity (v_{mean}) can be defined, which is proportional to the local flow rate.

$$f_l = \int v_l(A) dA \stackrel{!}{=} v_{mean} A_{channel} \tag{6.11}$$

In the following, the hydrodynamics of the microchannel restriction experiments (see chapter 7) are discussed, including the cells inside the channels and restrictions. In the delivery channels with a cross-section of 40x40 μm, the cells, which have a mean diameter of 22.5 μm, have no direct channel wall contact and flow with the medium. The approaching cell itself, before it is deformed, is used here for flow velocity tracking. For three different total flow rates that were set, the approach velocities ($v_{approach}$) for cells were plotted in figure 6.12. As expected from equations 6.9 and 6.11, the cell approach velocity is linear proportional to the set flow rate and can be thus used a measure for the total and local flow rate (see equation 6.12).

$$f_t, f_l \propto v_{approach} \tag{6.12}$$

However, the scatter for the cell appraoch velocities is high. Reason for this, among resolution errors in cell velocity tracking , is the cell wall interaction. As the cell surface can be approximated

[8] PHD 2000 Syringe Pump, Harvard Apparatus
[9] Injekt-F 1ml, Braun
[10] COMSOL Multiphysics

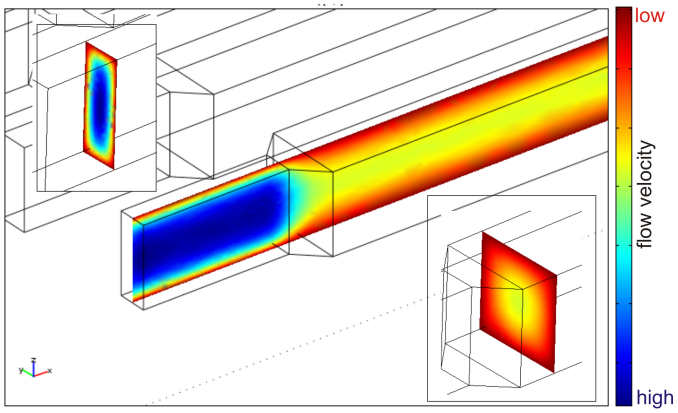

Figure 6.11: FEM simulation of velocity distribution of a laminar flow at constant flow rate in a microchannel narrowing into a restriction. The blue color marks the highest flow velocity.

in this case as a stiff boundary compared to the surrounding medium, interaction between cell surface and channel wall influence the cell velocity. In general, it is, thus, observed that smaller cells are slighly faster.

Additionally, cells that are compressed inside the restrictions distrurb the flow, as they can be regarded as fixed obstacles compared to the medium flow around them. The about 22.5 μm wide cells are compressed in 1 dimension in the 15x40 μm restriction. The cells influence the local flow resistance as depicted in figure 6.13 and thus local and global flow in the channel system. The cell shape is not completely known and furthermore dynamic. A rough estimation can be done, by assuming a total blockage of the channel by the cell. Still, pressure or flow changes can not be measured locally during the experiments. Finite element simulations can estimate variations, but are not sufficient, because it requires certain assumptions as cell shape or, for dynamics, cell material properties, which is the actual goal of the project.

To summarize, variations in driving flows and pressures, which potentially corrupt cell sliding velocities in microrestriction experiments, can not be quantified. Finally, only the direct assessment of cell deformation with the microflaps overcomes the challange of distrurbed flows through the cells themselves.

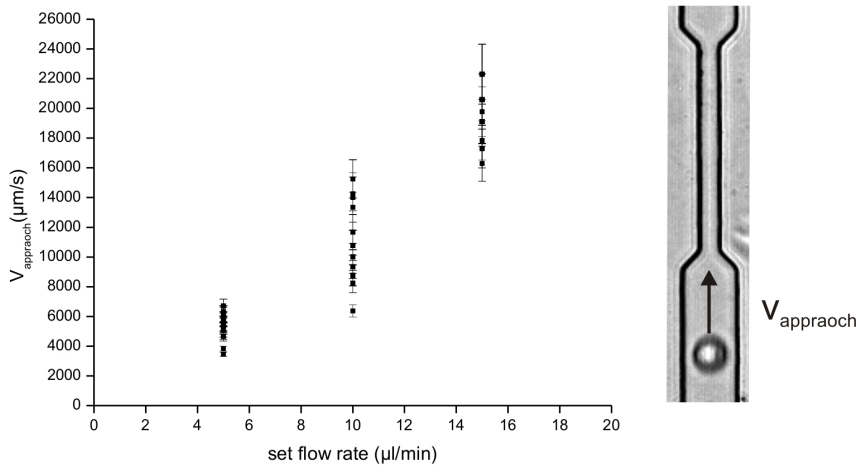

Figure 6.12: Cell approach velocities for different set flowrates. The cell appraoch velocity is linaer proportional to the set flow rate and can thus be used as a measure for the local flow rate.

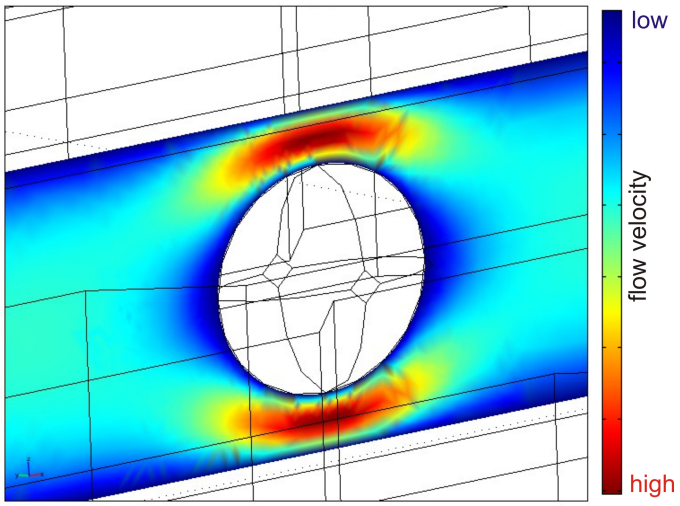

Figure 6.13: FEM simulation of velocity distribution around ellipsoid cell in a channel restriction. Finite element simulation of a 1D compressed cell resting in a channel with a constant flow rate applied. The red color marks the highest flow velocity.

Chapter 7

Indirect Assessment of Cell Mechanics in Microchannel Restrictions

7.1 Introduction

In this chapter, it is described how the cell mechanical resistance to deformation is measured indirectly inside microchannel restrictions. A population of Panc-1 cells is deformed during entering and transiting microchannel restrictions. Cell deformation times and sliding velocities while moving through the restrictions are observed for different applied flows and varying cell size. A data scatter is present, which is attributed to cell size, cell mechanical inhomogeneities and systematic variations. Systematic variations arise mainly from uncertainties of the cell-disturbed flow field and unknown adhesion or lubrication processes at the cell-channel interface, which will be discussed. In order to overcome, the systematic uncertainties and the general dependence on flow rate and frictional processes, which mask the cell mechanical properties, a new method to directly observe cell mechanical resistance to deformation was developed and is presented in the next chapter 8.

7.2 Cell Dynamics in Microchannel Restrictions

7.2.1 Sliding Velocity and Entrance Time

The two indirect quantitative measures of cell deformation resistance in a microchannel restriction are introduced here. A typical data set of the dynamics of a cell entering and transitting a microchannel restriction is shown in figure 7.1. The cell's front and back edge movement over time were tracked via a minimum intensity search utilizing a custom written Matlab[1] routine. The cell's arrival in the prelocated 40x40 μm wide channels, the restriction entrance process, the sliding inside the 15x40 μm wide restrictions as well as the exit was included in the tracking. As a measure for the local flow velocity and thus applied flow rate, the cell itself is used for flow velocity tracking, before entering the restriction (see section 6.6.3). The cell approach velocity

[1] The Mathworks Inc.

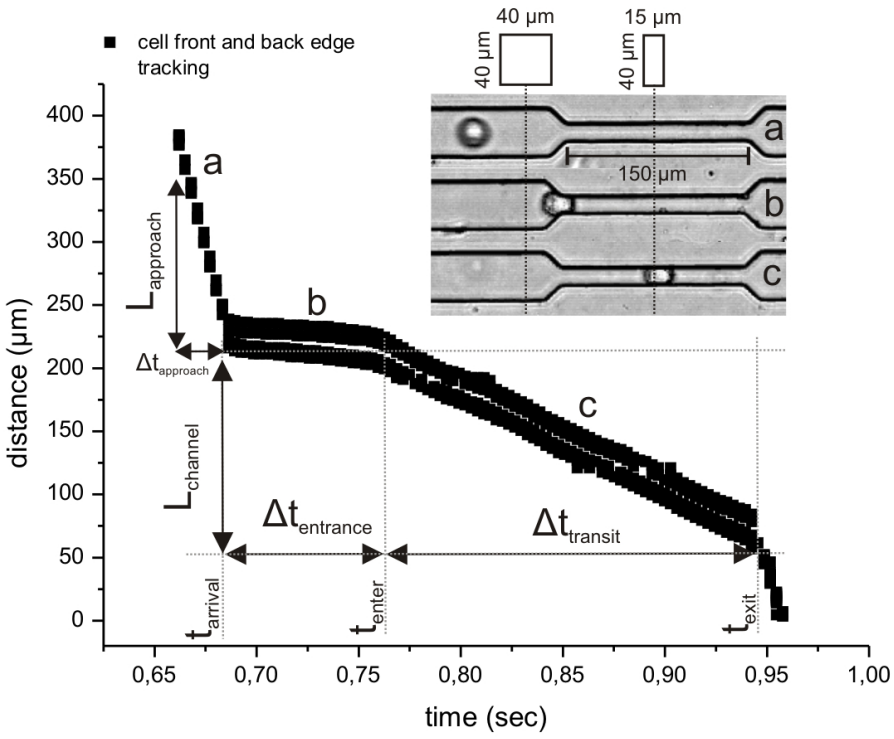

Figure 7.1: Tracking of cell path over time in long microrestriction. The cell is approaching the restriction, enters it and slides through the restriction at constant velocity.

($v_{approach}$ see equation 7.1) is extracted as a certain approch length ($L_{approach}$) devided by the needed appraoch time ($\Delta t_{approach}$).

$$v_{approach} = \frac{L_{approach}}{\Delta t_{approach}} \tag{7.1}$$

For quantifying the deformation during entering the microchannel restriction, the entrance time ($\Delta t_{entrance}$ see equation 7.2) is defined as the time difference between cell arrival ($t_{arrival}$) at the restriction and the time the whole cell has entered the restriction (t_{enter}).

$$\Delta t_{entrance} = t_{arrival} - t_{enter} \tag{7.2}$$

In most cases, the sliding velocity of the cell was found to be constant and used as a measure for quantifying cell mechanics indirectly during sliding. Thus, a mean sliding velocity ($v_{sliding}$ see equation 7.3) was defined as channel length ($L_{channel}$) devided by the transit time ($\Delta t_{transit}$). The transit time is in turn defined as the period of time, during which the cell is situated inside the microchannel restriction, i.e. entrance time and exit are excluded.

$$v_{sliding} = \frac{L_{channel}}{\Delta t_{transit}} \tag{7.3}$$

The constant sliding velocity, as depicted in figure 7.1 reveals an equilibrium of frictional forces and driving forces. It suggests that neither sufficient force relaxation of the cell, nor pressure changes occur during the timescale of transit. For cell mechanical properties this suggests, that either the cell material relaxation time is not in the order of the transit time or possibly fluidisation could be present and the cell thus behaves as a liquid droplet of a certain viscosity. Another explaination would be that the change in friction forces due to force relaxation are very small and thus negligable. In the same way the pressure changes due to the cells disturbing the flow could be assumed to be insignificant.

7.2.2 Experimental Procedure and Protocols

Cell suspension

Panc-1 cells were kept in culture (37°C, 5%CO_2) at a maximum confluency of 70% in DMEM[2] containing 10% FCS[3], 1% Penicillin-Streptavidin[4] and 1% L-glutamine[5]. After trypsinisation, the cells are kept in suspension in a 15 ml tube for a 20 min (37°C, 5%CO_2). Subsequently, cells are resuspended and filled into a preheated 1 ml syringe. The syringe is then fixed on the syringe pump[6]. Inside the syringe a magnetic stir bar is placed and used to manually resuspend the cells if necessary with another magnet.

Equipment Preparation and Experiments

The flow cell chip sits on an optical microscope[7]. Prior to cell injection, the flow cell is filled in 3 different steps, utilizing the syringe pump, in order to prevent air bubbles that would change

[2]DMEM 11960, Gibco
[3]FCS,PAA Labs
[4]Penicillin-Streptavidin 15140, Gibco
[5]L-glutamine 25030, Gibco
[6]PHD 2000 Syringe Pump, Harvard Apparatus
[7]Axiovert200, Zeiss

flow resistance, if they were situated in the channels. First, the channels are filled with a 1:1 mixture of ethanol and deionized water, which has a high wettability. Subsequently, the flow cell is washed for 5 min with deionized water, followed by a PBS wash for 10 min. All liquids are filtered prior to use to remove micrometer sized dust particles. Then the cells are injected with a constant total flow rate of 5, 10 and 15 μl/min, applied by the syringe pump. A highspeed camera[8] records at framerates of 2000 fps to 7000 fps through a 10x long distance objective[9]. The total recording time per experiments only takes several seconds.

7.3 Responses on Flow Rate and Cell Size Variations

The cell sliding velocity and the entrance time are observed as a function of applied flow and as a function of cell size. On the basis of these data the implications for cell material and frictional properties will be discussed in the following.

It is not surprising that an increasing applied flow, will result in a shorter entrance time (see figure 7.2) as well as an increased sliding velocity through the channel restriction (see figure 7.3). However, the functional relationship between flow rate and entrance time or sliding velocity gives certain hints on the cell mechanics and frictional processes during the cell squeezing and sliding. The entrance time shows a strong increase towards smaller applied flow rates. The steplike increase of the entrance time, over 3 oders of magnitude (see figure 7.2), could suggest a shear rate limit for actin fluidisation. However, the steplike increase could also only mark that frictional forces are then in the order of driving forces. Obviously, the entrance time will converge to infinity for a critical flow rate where the cell will get stuck in the entrance of the restriction. Entrance time and sliding velocities are negatively correlated (data not shown). As expected, a cell that has a higher resistance to deformation during channel entrance will slide at a slower velocity. This suggest on the other hand no complete fluidization of the cell. However, for higher flow rates the relation is less strong, supporting the hypothesis of a certain amount of fluidisation during the entrance process.

The scaling of the sliding velocity with the applied flow suggests a more than linear increase (see figure 7.3). Still, in the case of sliding velocities there is no steplike decrease visible as for the entrance time, which would again support the suggested actin fluidization during entering of the channel restrictions. Assuming a mean equal contact pressure of each cell, this, so-called, shear thinning behavior could be explained by the cell-wall surface properties (see section 6.3) as either brushlike surface structure of the cells or specific adhesion. In the first case, an increased sliding velocity would increase steric repulsion of the brushes on the cell towards the channel wall and in turn act as a lubricant. It has been shown that the cell surface, the glycocalix, is composed of a variety of polymerbrushlike structures. In the second case of specific adhesion, a higher number of ruptured adhesion bonds compared to the newly formed ones increases sliding velocities, which also would lead to a lower contact pressure and higher sliding velocities. Specific adhesive bonds are in fact possible, because the cells are suspended in cell culture medium, which contains a number of cell specific proteins, that can adsorb to the channel walls. Still, the obtained data are not a clear indication. For determination of frictional dependencies, further investigations with different channel wall coatings will be needed as well as a larger range of applied flow rates. The vertical scatter in both graphs (figures 7.2 and 7.3) potentially reflects cell size as well as cell mechanical differences and possible flow variations. In order to check the mechanical homogeneity of the cell sample, entrance time and sliding velocity are examined as a function of cell diameter at a constant flow rate (see figure 7.4). A homogeneous

[8] PCO 1200 hs, Pco Imaging
[9] 10x/0.25 Ph1 A-Plan, Zeiss

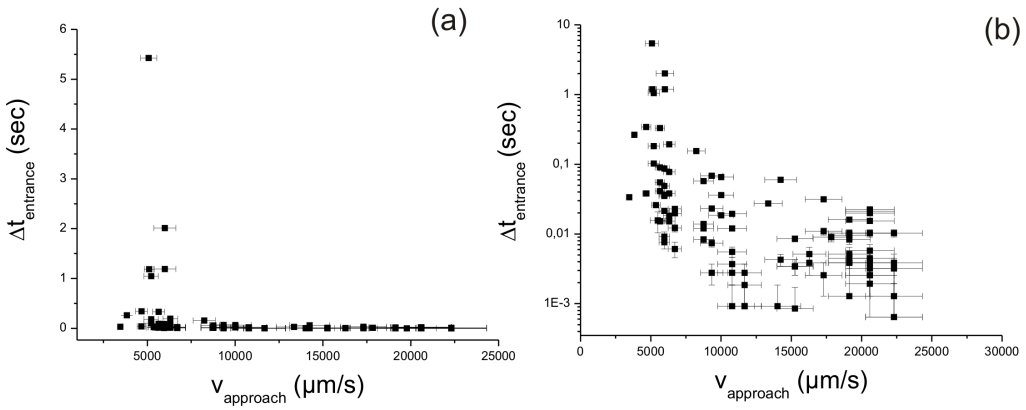

Figure 7.2: Cell entrance times as a function of cell approach velocity. (a) Lin-lin scale. (b) Log-lin scale. The entrance time decreases overproportional with approach velocity.

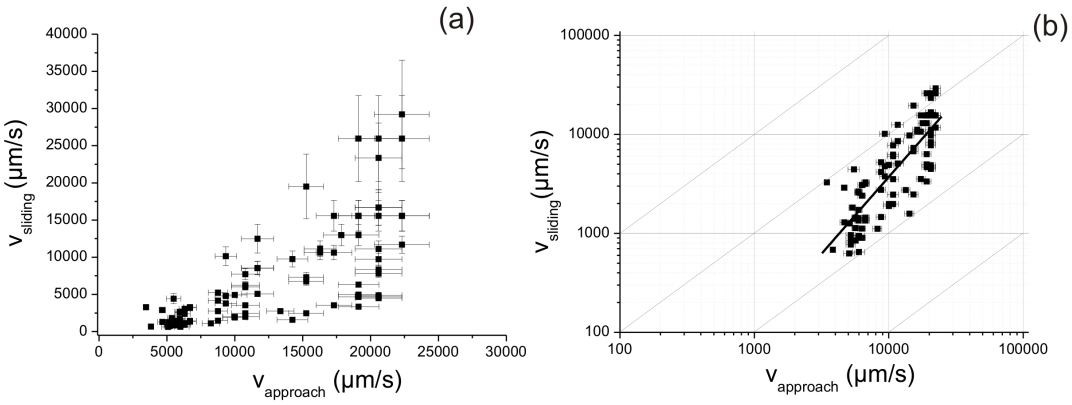

Figure 7.3: Cell sliding velocities as a function of cell approach velocity. (a) Lin-lin scale. (b) Log-log scale. The sliding velocity is suggested to follow a power law with an exponent greater than one.

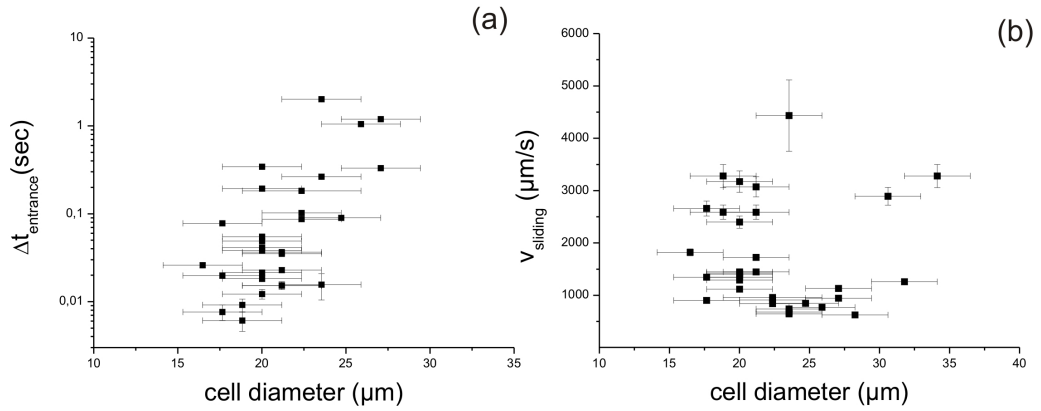

Figure 7.4: (a) Cell entrance time and (b) cell sliding velocities as a function of apparent cell diameter for a constant applied flow rate.

material response, and solely a function of cell size, was a priori expected as there is only one cell line (Panc-1) used. For the cell sliding velocity, no clear dependence on cell size is seen; for the entrance time, a positive correlation is observed. Still, both plots show scatter for a fixed cell diameter, which are attributed to cell inhomogenities and possible inhomogenities in the driving flow. As the microchannel restriction size is in the order of the nucleus size, cell in homogeneity could solely arise from the nucleus size or multiple nuclei.

To summarize, the data suggest a partly fluidization of the cell population as well as a surface effected sliding behavior. Both suggestions will need further experimental proof. However, interestingly, it was found that the scatter of the data are partly a cell size effect, but also suggest cell inhomogenities. Nethertheless, flow variation due to the cells itself can not be excluded to contribute to this. The latter fact, clearly shows the weakness of this attempt to measure cell mechanics with microchannel restrictions.

Chapter 8

Direct Assessment of Cell Mechanics using Microflap Restrictions

8.1 Introduction

In this chapter, the novel method of microflaps for directly assessing cell deformation resistance during dynamic squeezing is presented. The proof of principle and reproducibility is given as well as a critical discussion and suggestions for improvement of the technique. A theoretical estimation for measuring absolute forces is presented.

The dynamics of a cell deforming in a microflap restriction is observed. It is directly shown that the time for squeezing into a narrow restriction is correlated with the amount of flap deflection and thus the cell mechanical properties. Further, the observations suggest that the cells have a rather inhomogeneous deformation resistance in the examined compression regime, as already observed in chapter 7.

8.2 Dynamics of Cells Deformation While Passing the Microflaps

8.2.1 Flap Deformation Tracking

When cells are transiting through the microflap restriction, the flap bends (see figure 6.3). The deformation of the flap is assessed by tracking the movement of the top flap edge.

A customized Matlab[1] routine detects the outer edge of the flap by finding intensity minima in line profiles normal to the flow direction as depicted in figure 8.1. A deflection versus frame graph as shown in figure 8.2 is obtained. The mean and standard deviation of 5 profiles situated in the middle part of the flap are calculated, where each profile is base line corrected. The deflection resolution is, in principle, restricted by the pixel size of the camera and the optical resolution of the objective and the microscope. In this case, the standard deviation of 5 profiles exceeded one pixel during flap bending compared to no bending, suggesting systematic errors during bending. However, bending due to cell transiting can be sufficiently relsoved. The flap showed no significant torsion, during cell deformation and cell passage.

[1] The Mathworks Inc.

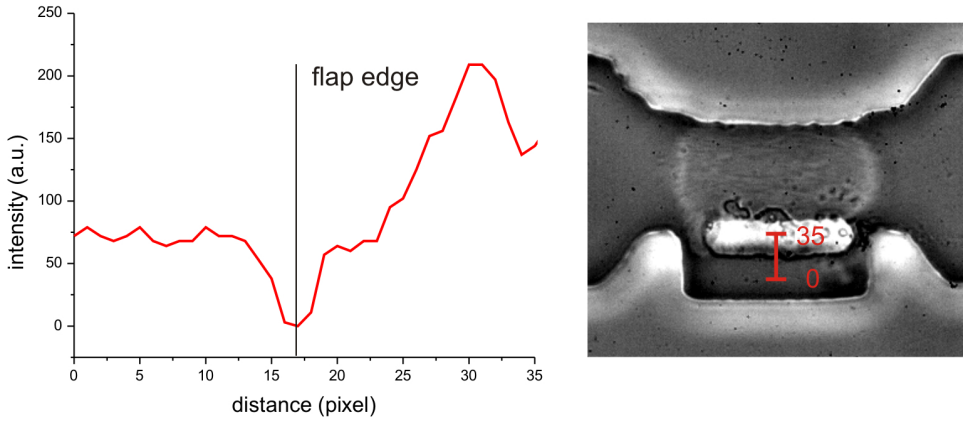

Figure 8.1: Edge detection of microflap. The minimum intensity at the flap edge is detected on intensity profiles perpendicular to the flow direction.

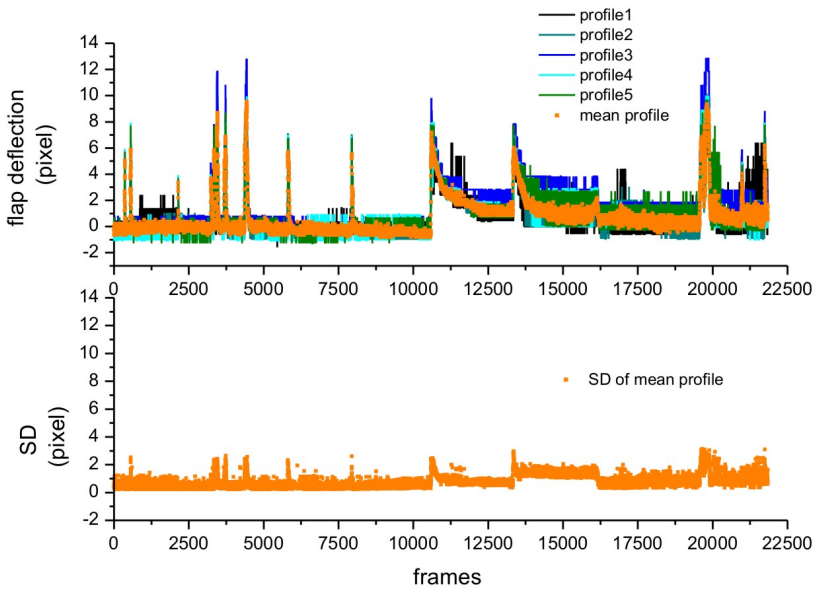

Figure 8.2: Deflections of microflap while cells are transiting. The mean of 5 profiles and the standard deviation is given. The peaks represent one or more cells. A force relaxation event could be observed (starting at frame 10000).

8.2.2 Experimental Procedure and Protocols

Cell suspension

Panc-1 cells were kept in culture (37°C, 5% CO_2) at a maximum confluency of 70% in DMEM[2] containing 10% FCS[3], 1% Penicillin-Streptavidin[4] and 1% L-glutamine[5]. After trypsinisation, the cells are kept in suspension in a 15 ml tube in 25 mM Hepes buffered DMEM[6] containing 1% Penicillin-Streptavidin for 20 min (37°C, 5% CO_2). Subsequently, cells are resuspended and filled into a preheated syringe[7]. The syringe is then fixed on the syringe pump[8] which is situated inside the inbubation chamber (37°C) of the optical microscope[9]. Inside the syringe a magnetic stir bar is placed and used to manually resuspend the cells if necessary with another magnet.

Equipment Preparation and Experiments

The flow cell and the syringe pump are situated inside the incubation chamber on the microscope and are heated to 37°C. Prior to cell injection, the flow cell is filled in 3 different steps, utilizing the syringe pump, in order to prevent air bubbles. First, the channels are filled with a 1:1 mixture of ethanol and deionized water, which has a high wettability. Subsequently, the flow cell is washed for 5 min with deionized water, followed by a PBS wash for 10 min. All liquids are filtered prior to use to remove micrometer sized dust particles. Then the cells are injected with a constant total flow rate of 5 μl/min, applied by the syringe pump. A highspeed camera[10] records at framerates of 2000 fps to 7000 fps through a 100x oil immersion objective[11]. The total recording time per experiment only takes several seconds.

8.2.3 Dynamics of Suspended Cell Deformation

The cell squeezing process of a single cell is recorded at sufficient time resolution to observe flap deformation and cell elongation (see figure 8.3). The cell's front edge and back edge are tracked, where their difference is the cell length. The initial cell diameter is referred to as apparent diameter because the cells are already compressed in the 15 μm tall channel. The cell squeezes from a 15x40 μm cross section channel into a 15x15 μm restriction with a 25 μm long, 15 μm tall and 5 μm thick flap.

As the cell enters the microflap restriction, the flap bends and the cell deforms and elongates. The maximum elongation is observed when the cell is completely deformed and the maximum flap deflection is reached. The cell is slowed down when entering the restriction and accelerated when it leaves the restriction again. The time difference from cell entry until the maximum flap deflection is reached is defined here as entrance time. Exiting the flap takes less time for the cell. The reasons for this can be a not completely elastic, but also time dependent cell response or shear thinning and fluidization effects are present.

[2] DMEM 11960, Gibco
[3] FCS, PAA Labs
[4] Penicillin-Streptavidin 15140, Gibco
[5] L-glutamine 25030, Gibco
[6] DMEM 21063, Gibco
[7] Injekt-F 1 ml, Braun
[8] PHD 2000 Syringe Pump, Harvard Apparatus
[9] Axiovert200, Zeiss
[10] Phantom V, Vision Research Inc.
[11] 100x/1.3oil Ph3 Plan Neofluar, Zeiss

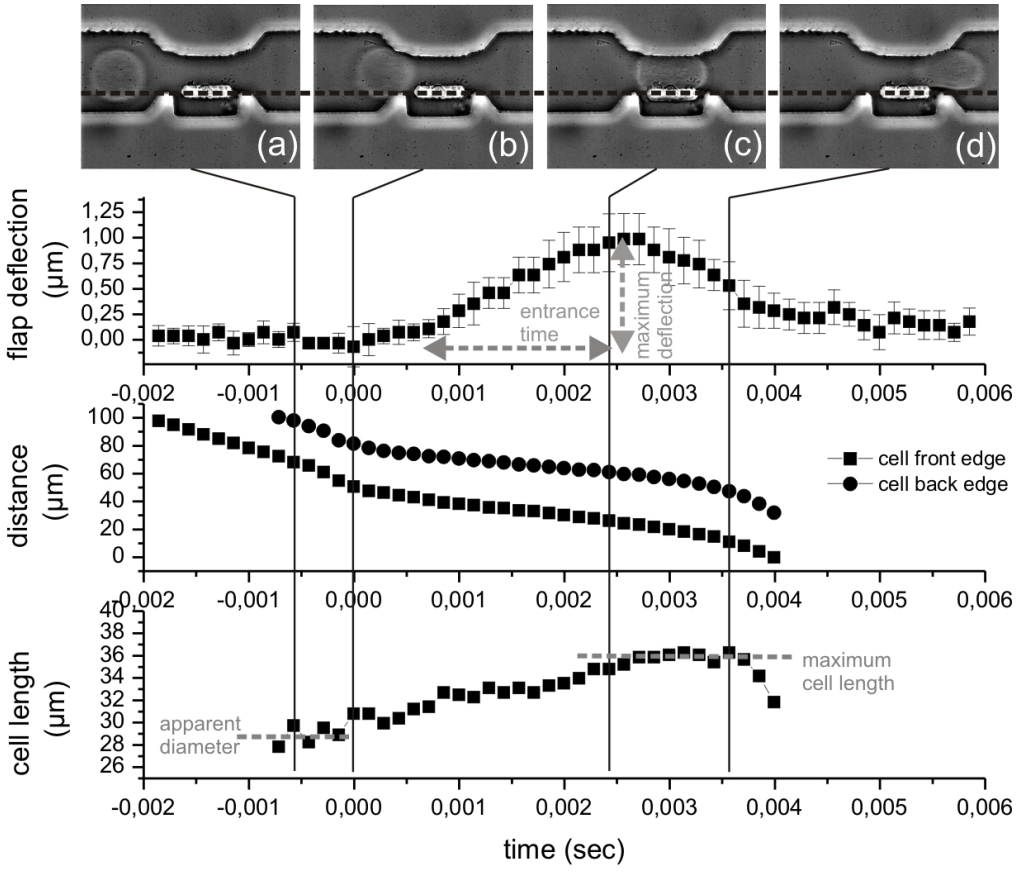

Figure 8.3: Flap deflection, cell front and back edge movement and cell length during Panc-1 cell squeezing through a microflap restriction. (a) The cell is approaching the flap from the delivery channel. (b) The cell is entering the restriction. (c) The cell is almost completely compressed in the restriction and the flap is bent. (d) The cell exits the restriction.

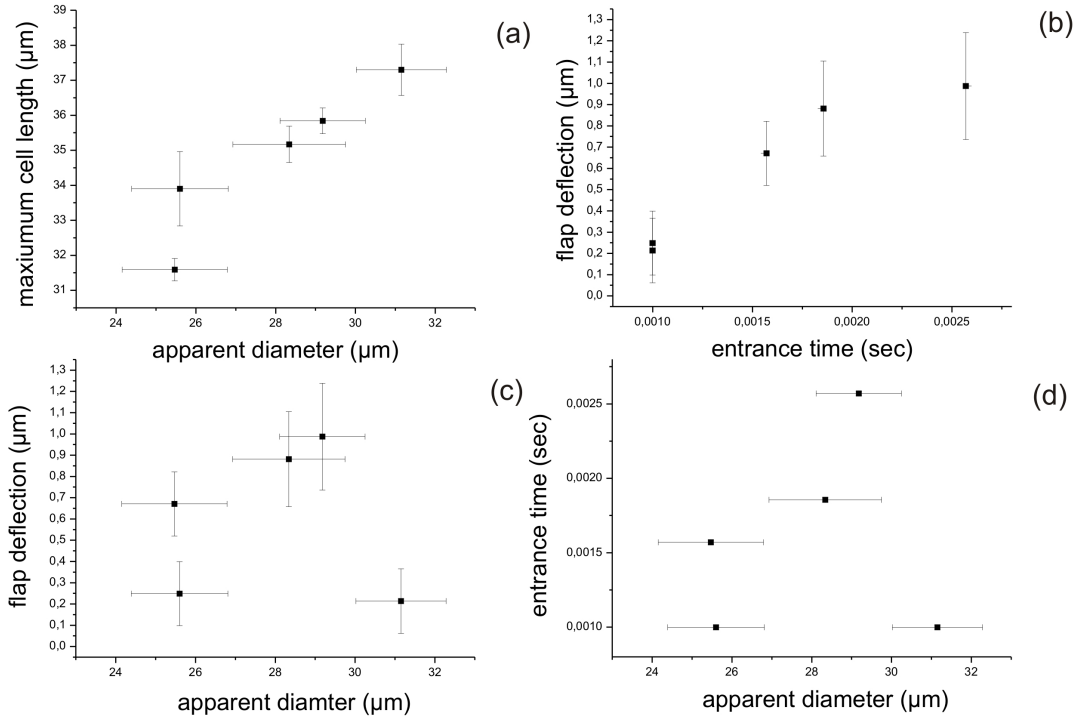

Figure 8.4: Interdependencies between apparent cell diameter, maximum cell length, entrance time and maximum flap deflection.

For 5 single cell events the correlation of apparent cell diameter, maximum cell length, maximum deflection and entrance time is examined. As expected, maximum cell length is dependent on the apparent diameter and thus compression level (see figure 8.4 (a)). Contrary to this, the maximum deflection and the cell entrance time are not clearly correlated with the apparent cell diameter as shown in figure 8.4 (c) and (d). This is suggesting a inhomogeneous material response, arising from an inhomogeneity within a cell or a cell to cell variation which is independent of cell size. The position and the rearrangement of the nucleus within the cell, and multiple nuclei might be responsible for these deviations. However, flap deflection and entrance time are correlated (see figure 8.4 (b)), showing that a mechanically robust cell can enter a restriction only slow and possibly gets stuck more easily. A further study, with different channel sizes and different applied flow rates is necessary to clarify the influence of compression ratio and deformation rate effects.

A drawback of the technique is the occurance of multiple cells in a row or cell agglomerates, where entrance times are difficult measure. Thus, the maxium deflection per cell and its apparent diameter are used to show repeatability on different flow cell chips with better statistics. The experiment is reproducible within the deflection detection resolution limits for 2 different flow cell chips with the same geometry (see figure 8.5). Here, a correlation of maximum deflection with cell size is seen. Nevertheless, the data scatter still indicates a systematic difference for cells of the same apparent diameter.

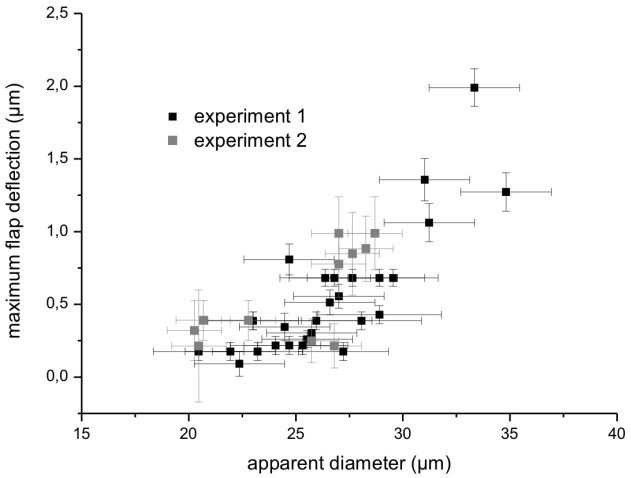

Figure 8.5: Two independent cell experiments with two flow cell chips show reproducibility. The flow rate is kept constant.

8.3 Approximating Absolute Deformation Forces

8.3.1 Elastic Theory for a Uniform Loaded Beam

The absolute force that a cell exerts on the rectangular PDMS flap with length (L), width (W) and thickness (T), is calculated by assuming a constant contact pressure on the flap area (P_{flap} [N/m^2]), and respectively a constant force per length (f[N/m]) (see figure 8.6). This is a reasonable approximation because the cell is completely filling the restriction volume and adjusts to the channel shape, which is different to the end-loaded cantilever in AFM indentation. However, non uniform load as e.g. cell inhomogenities can not be excluded. Thus, the forces calculated in the follwing can only be seen as an approximation.

For a bending beam, the absolut value of the locally applied torque (M) must be balanced by the elastic energy of the beam (see equation 8.1). The stored elastic energy is dependent on elastic modulus of the beam material (E), the area moment of inertia (I_A), and the local beam curvature ($1/R_C$). Further, for small deformations of the end fixed flap, the beam curvature can be described as the second derivative of the beam shape (see eqaution 8.2). [Lan05]

$$M = \frac{EI_A}{R_C} \leftrightarrow \frac{M}{EI_A} = \frac{1}{R_C} \tag{8.1}$$

$$\frac{1}{R_C} = \frac{\frac{d^2y}{dx^2}}{\left[1 + \left(\frac{dy}{dx}\right)^2\right]^{\frac{3}{2}}} \overset{\frac{dy}{dx} \ll 1}{\approx} \frac{d^2y}{dx^2} \tag{8.2}$$

Integration leads to the beam shape and the deflection at length (L) (see equation 8.3). The area moment of inertia (I_A) is given by equation 8.4 and is constant over beam length as well as the elastic modulus (E) is constant. The applied torque (M(x)) at a point on the beam originating

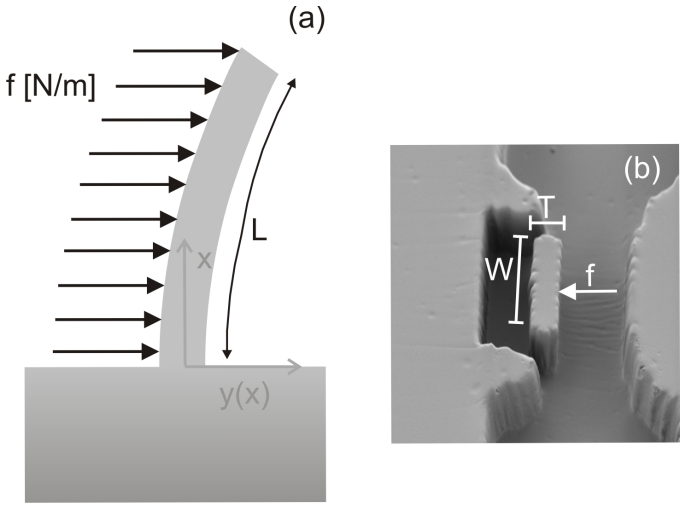

Figure 8.6: Sketch of PDMS microflap. (a) Sketch of a uniform loaded beam. (b) SEM picture of microflap showing geometric parameters and loading direction.

from the uniform load per length (f) is given by equation 8.5. [Lan05]

$$\frac{d^2y}{dx^2} = \frac{M(x)}{EI_A} \rightarrow y(x) = \frac{1}{EI_A}\int\left[\int M(x)dx\right]dx \rightarrow y(L) = \frac{3}{2}\frac{fL^4}{ET^3W} \tag{8.3}$$

$$I_A = \frac{T^3W}{12} \tag{8.4}$$

$$M(x) = \int f(L-x)dx = \frac{1}{2}fx^2 - fLx \tag{8.5}$$

The total force on the flap F_{flap} and the exerted pressure P_{flap} can be now obtained (see equations 8.6 and 8.7).

$$F_{flap} = fL = \frac{2}{3}\frac{y(L)ET^3W}{L^3} \tag{8.6}$$

$$P_{flap} = \frac{f}{W} = \frac{F_{flap}}{WL} = \frac{2}{3}\frac{y(L)ET^3}{L^4} \tag{8.7}$$

8.3.2 Elastic Theory for a Point Loaded Beam

In order to compare, how the loading condition influences the calculated total forces and microflap deflections, a cantilever with a point load in the middle of the beam is considered. This would be the case, if, for example, the nucleus exerts a pointlike force in the middle of the cantilever.

For an endloaded rectangular cantilever (see figure 8.7a), as for AFM indentations, the point loading force (F_{end}) and the deflection at the cantilever end $y_{(end)}(L)$ are given by equations 8.8 and 8.9.

$$y_{end}(x) = \frac{Fx^2(3L-x)}{6EI_A} \rightarrow y_{end}(L) = \frac{4F_{end}L^3}{ET^3W} \tag{8.8}$$

$$F_{end} = \frac{1}{4}\frac{y_{end}(L)ET^3W}{L^3} \tag{8.9}$$

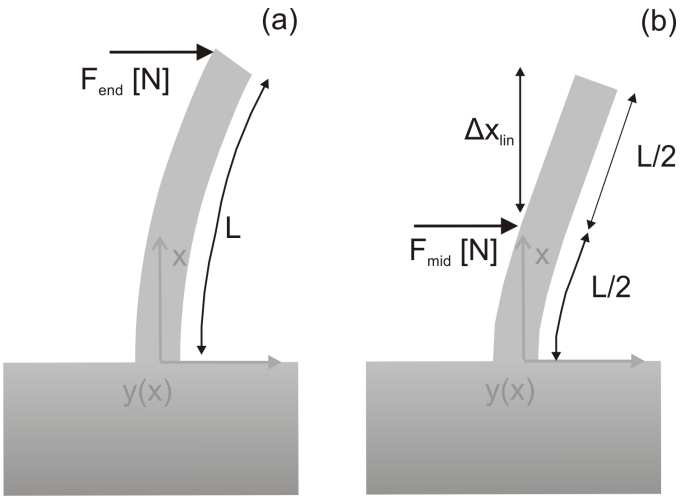

Figure 8.7: Sketch of PDMS microflap. (a) Sketch of a endloaded beam. (b) Sketch of a mid-loaded beam.

If a point load is instead exerted in the middle of a cantilever (F_{mid}) (see figure 8.7b), the end deflection is the sum of the deflection of an endloaded cantilever of length $\frac{L}{2}$ and the linear part of the cantilever which is pointing at an angle determined by the cantilever bending at length $\frac{L}{2}$. Further, small deflections are assumed. The loading force (F_{mid}) and the deflection at the cantilever end $y_{(end)}(L)$ are then given by equations 8.10 and 8.11. [Lan05]

$$y_{mid}(L) = y_{end}(\frac{L}{2}) + \frac{dy_{end}(x)(\frac{L}{2})}{dx}\Delta x_{lin} \overset{\Delta x_{lin}\approx\frac{L}{2}}{\approx} \frac{5}{4}\frac{F_{mid}L^3}{ET^3W} + \frac{9}{4}\frac{F_{mid}L^3}{ET^3W} \tag{8.10}$$

$$F_{mid} = \frac{2}{7}\frac{y_{end}(L)ET^3W}{L^3} \tag{8.11}$$

The total force needed to bend a cantilever with a point load to a certain deflection is only 0.4 times the total force of a uniformly loaded cantilever. It is concludud, that a pointlike force, originating e.g. from the nucleus, can potentially alter the force and microflap deflection measurements.

8.3.3 Forces Exerted by Suspended Cells

Assuming a uniform load, forces of up to 1μN are reached during cell squeezing in a 15x15μm cross section restriction, where a majority of the cells range from 250 to 500 nN (see figure 8.8). Compared to AFM compression of round cells, the forces measured with the microfluidc flap are in the same order of magnitude. The forces correspond to a pressure of 300 to 1000 Pa exerted on the microflap.

In order to calculate the force on the cantilever, the knowledge of elastic modulus of the PDMS and the cantilever geometry is necessary. The PDMS elastic modulus is determined as described in chapter 4.4 on each flow cell before and after the experiments. A higher elastic modulus was found after the experiments, which is probably due to aging effect in the PDMS over time. The microflap geometry is measured with the SEM.

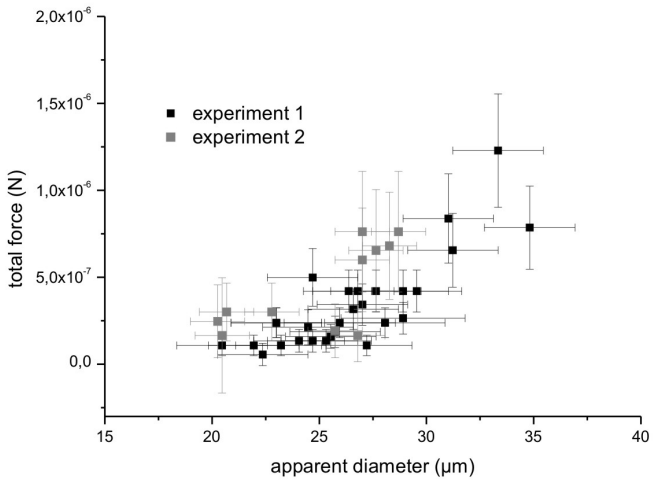

Figure 8.8: Total forces exerted on a microflap by the cells in a 15x15 μm restriction assuming a uniform load. Forces are calculated with equation 8.6. A constant flow rate is applied.

8.3.4 Force Relaxation in 2D confinement

A relaxation event of a cell in 2D confinement was observed, as a cell got stuck in a channel for a longer time, because the channel was partly blocked by the residuum of a preceding cell. This relaxation process is accompanied by a shear process in contrary to the common relaxation experiments as, e.g., with AFM. A fit of a simple exponential decay gives a characteristic time of 0.065(+/-0.001) seconds (see figure 8.9). In comparison to AFM relaxation on adherent cells, this is an order of magnitude smaller. This shows that, in general, relaxation events can be observed with the microflap technique, if time resolution and cell transit time are sufficient.

8.4 Advantages, Limitations and Possible Improvement of the Technique

A new method for directly assessing cell mechanics during cell squeezing is developed. Nevertheless, a drawback of the technique is the fact that it is a contact based mechanical testing system, which induces artifact due to cell trash, where, e.g., the optical stretcher [Guc05] has a clear advantage. Further, agglomerations of cells and multiple cells are not an advantage. Still, this might be solvable by a better mixing of the cell suspension and the application of flow focussing [Huh05].

The microflap is able to measure forces. However, for absolute force measurements, the loading conditions of the microflap need to be know. For the simple case of a uniform load a total force and pressure can be calculated. Microflap deflection and force resolution can be increased with a lower PDMS elastic modulus or replacement of PDMS with another suitable soft material. A smaller thickness and width, as well as an increase in flap length, would increase resolution further. As mentioned in section 6.6 the peel off process of the delicate flaps is the limiting factor in the production of the flaps up to this point. Deflection detection might be changed from

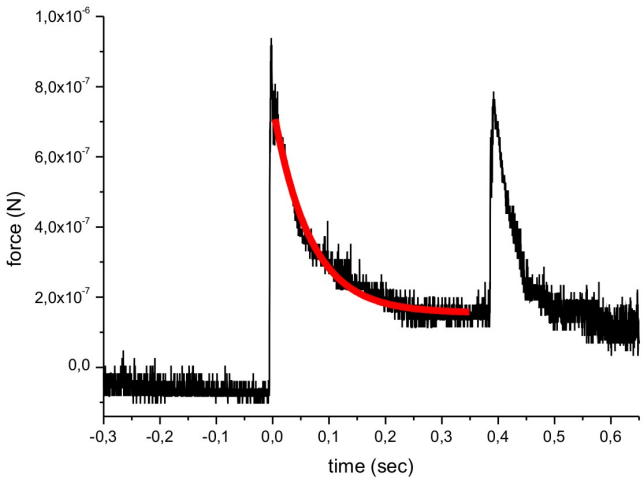

Figure 8.9: Force relaxation process in a microflap restriction and a fit of an exponential decay. The characteristic time is 0.065 seconds.

optical image processing to a laser assisted method, as in AFM, for nm resolution.

Although, for example, micropipette aspiration [Hoc00], in principle, delivers similar information on cell mechanics, the microflap might be suitable for a highthroughput tool. The production is simple, easy to reproduce and cost effective. In principle, the technique is applicable for all types of cells in order to measure abolute deformation forces or for detecting cell mechanical differences. Even beyond cells, for e.g. vesicles and elastic beads, this method might be suitable.

Conclusions and Outlook

Cell mechanical responses are important in the context of physiologically relevant deformations and stresses that cells have to sustain inside the body and are closely related to the time scale, force scale, length scale and geometry of the deformation process, as well as the cell state and the condition of subcelluar components. In this thesis, it was sought to understand and to quantify the cell mechanical response during active cell migration of adherent pancreatic cells (Panc-1) in the tissue, and, on the other hand, the passive transportation of suspended pancreatic cancer cells through the vessel system. In the first part of the thesis, Panc-1 cells were observed in an adherent state and deformed quasistatically and locally, which was intended to resemble the slow process of cell migration through small pores. In particular, the motivating question was the hypothesis that the lack of a dense keratin network inside those cells is correlated with a major lack in mechanical integrity. In turn, this was suggested as the reason for the facilitated cell migration through small pores in earlier studies and further suggested to be one mechanism for enhanced cancer cell migration during metastasis. During metastasis, the cells migrate in an abnormal and aggressive way from the primary tumor through the tissue into the circulation systems, as e.g. blood vessels. By passive transportation, the cancerous cells are shipped throughout the body until they get stuck in a small capillary. From there, the cells invade the tissue again and grow secondary tumors. The passive transportation and deformation of the Panc-1 cells in a suspended round state was observed in the second part of the thesis. Global cell deformation inside vessel-mimicking microrestictions was examined. Further, the use of microfluidic microrestrictions was envisioned as a high throughput cell mechanical testing device.

To quantify cell mechanical responses and the impact of the keratin network during cell migration, the material response of living adherent pancreatic cancer cells and their subcellular keratin network during quasistatic and local deformation was studied. A transient cell transfection made it possible to directly image the fluorescently labelled keratin network inside the living cells and for the extracted keratin network. Indentation testing on thin elastic layers of Polydimethylsiloxane (PDMS) confirmed the applied methodolgy of using the Atomic Force Microscope and an elastic model, which corrects for underlying substrate effects. The experiments revealed no effect of keratin meshsize density on the elastic modulus for living cells. Further, it was found that the cell to cell variation of the elastic modulus is higher than the elastic modulus of the extracted keratin. A contribution from the keratin network to the overall cell mechanics of only 2 to 5% is estimated by comparing living cell elastic moduli with keratin elastic moduli. However, this study showed for the first time a direct comparison of living cells and their keratin intermediate filament network, measured with the same technique.

In addition to indentation testing, during large strain stretching of the keratin network, a strain hardening response to deformation was seen. This fits very well into the picture of intermediate filament behavior of being robust to large tensile strains. However, the performed indentation testing was also on a large scale. Still, for cell migration behavior, it is not exactly clear, if large stretching or large compression or, in general, what stress fields a cell has to sustain during migration. Further, an active keratin network reorganization upon mechanical stress during indentation testing on the timescale of cell migration was observed in this thesis. Hence, it was concluded that the experimental approach taken was too simple for the complex process of cell migration. Another series of experiments is suggested for further work in order to clarify the role of the keratin network during cell migration. The keratin network deformation during active migration through microchannel restrictions needs be observed with high resolution time lapse imaging in order to justify, if there is a passive deformation or an active new formation of the keratin network. Further, it would be of interest to directly measure pressures that a migrating cell is exerting on the surrounding tissue during active deformation. The microflap restriction technique, which was originally developed here in this thesis for suspended cells,

would be suitable for this.

The second part of the thesis assessed the deformation dynamics of the Panc-1 cells, but in a suspended and round state at high deformation rates. Passive cell transportation and squeezing in the circulation system is mimicked. Deformation responses of suspended cells were first observed in microchannel restriction and, second, in microflap restrictions. The latter novel cantilever-based cell deformation detection technique consists of a microscale deformable beam that was implemented in a microrestriction of a flow cell chip. With this, for the first time, the cell mechanical response was assessed directly, and indepently of applied flow and frictional resistance, while the cell was squeezed through microchannel restrictions. Using the approximation of a constant pressure loaded cantilever, the total force and the pressure on the cantilever can be calculated from the microflap deflections. The working principle has been demonstrated. The presented measurements on living cells show the general capability of the technique for measuring forces and pressures. As every technique, the microflaps have advantages and disadvantages, but also potential for further improvements and for the evolution into a high throughput cell probing technique as originally intended.

List of Figures

Bibliography

[Ada05] Adams, M.L., Johnston, M.L., Scherer, A. and Quake,S. (2005). Polydimethylsiloxane based microfluidic diode. Journal of Micromechanics and Microengineering. Vol. 15. p.1517-1521

[Ana06] Ananthakrishnan, R., Guck, J. and Käs, J. (2006). Cell mechanics: recent advances with a theoretical perspective. Recent Res. Devel.Biophys., 5 (2006):36-69 ISBN:81-7895-215-7

[Ani08] Anita, M., Herricks, T. and Rathod, P.K. (2008). Microfluidic approaches to malaria pathogenesis. Cellular Microbiology. Vol.10 p.1968-1974

[Alb02] Alberts, B., Johnson, A., Lewis, J., Raff, M., Roberts, K., Walter, P. (2002). The molecular biology of the cell. 4th edition. Garland Science

[Bao03] Bao, G. and Suresh, S. (2003). Cell and molecular mechanics of biological materials. Nature Materials. Vol.2 p.715-725

[Bei04] Beil, M., Micoulet, A., von Wichert, G., Paschke, S., Walther, P., Omary, M.B., Van Veldhoven, P.P., Gern, U., Wolff-Hieber, E., Eggermann, J., Waltenberg, J., Adler G., Spatz, J. and Seufferlein, T. (2003). Sphingosylphosphorylcholin regulates keratin network architecture and visco-elastic properties of human cancer cells. Nature Cell Biology. Vol.5(9) p.803-811

[Bin86] Binnig, G. and Quate,F. (1986). Atomic force microscope. Physical Review Letters. Vol.56(9) p.930-934

[Bin82] Binnig, G., Rohrer, H., Gerber, C. and Weibel, E. (1982). Surface studies by scanning tunneling microscopy. Physical Review Letters. Vol.49(1) p.57-61

[Bro96] Brody, J.P., Yager, P., Goldstein. R.E. and Austin, R.H. (1996). Biotechnology at low Reynolds numbers.Biophysical Journal. Vol.71 p.3430-3441

[Bur02] Burnham, N., Chen, X., Hodges, C.S., Matei, G.A., Thoreson, E.J., Roberts, C.J., Davies, M.C. and Tendler, S.J.B. (2002). Comparison of calibration methods for atomic-force microscopy cantilevers. Nanotechnology. Vol.14 p.1-6

[Bus08] Busch, T.(2008). Die Rolle von Zytoskelettelementen bei der zellulären Migration und Differenzierung. PhD Thesis, University of Ulm

[But95] Butt, H.J. and Jaschke M. (1995). Calculation of thermal noise in atomic force microscopy. Nanotechnology. Vol.6 p.1-7

[But05] Butt, H. J., Capella, B. and Kappl, M. (2005). Force measurements with the atomic force microscope: technique, interpretation and applications. Surface Science Reports. Vol. 95 p.1-152

[Cai02] Caille, N., Thoumine, O., Tardy, J. and Meister, J.J. (2002). Contribution of the nucleus to the mechanical properties of endothelial cells. Journal of Biomechanics. Vol.35 p.177-187

[Car05] Carillo, F., Gupta, S., Balooch, M., Marshall, S.J., Marshall, G.W., Pruitt, L. and Puttlitz, C.M. (2005) Nanoindentation of polydimethylsiloxane elastomers: Effect of crosslinking, work of adhesion, and fluid environment on elastic modulus. Journal of Materials Research. Vol.20(10) p.2820-2830

[Cos06] Costa, K.D., Sim, A.J. and Yin, F.C.P. (2006). Non-hertzian approach to analysing mechanical properties of endothelial cells probed by atomic force microscopy. Journal of Biomechanical Engineering. Vol.128 p.176-184

[Cro07] Cross, S.E., Jin, Y.-S., Rao, J., Gimzewski, J.K. (2007). Nanomechanical analysis of cells from cancer patients. Nature Nanotechnology. Vol.2 p.780-783

[Dar07] Darling, E.M., Zauscher, S., Block, J.A. and Guilak,F. (2007) . A thin-layer model for viscoelasticity, stress-relaxation testing of cells using Atomic Force Microscopy: Do cell properties reflect metastatic potential? Biophysical Journal. Vol.92 p.1784-1791

[Deu09] Deuschle, J.K., Deuschle, H.M., Enders, S. and Arzt, E. (2009). Contact area determination indentation testing of elstomers. Journal of Materials Research. Vol.24(3) p.736-748

[Des05] Desprat, N., Richert, A., Simeon, J. and Asnacios, A. (2005). Creep function of a single living cell. Biophysical Journal. Vol.88 p.2224-2233

[Dim02] Dimitriades, E. K., Horkay, F., Maresca, J., Kachar, B., Chadwick, S. (2002). Determination of elastic moduli of thin layers of soft material using the Atomic Force Microscope. Biophysical Journal. Vol.82 p.2798-2810

[Dru01] Drury, J.L. and Dembo, M. (2001). Aspiration of human neutrophils: effects of shear thinning and cortical dissipation. Biophysical Journal. Vol.81 p.3166-3177

[Eng04] Engler, A.J., Richert, L., Wong, J.Y., Picart, C. and Discher, D.E. (2004). Surface probe measurements of the elasticity of sectioned tissue, thin gels and polyelectrolyte multilayer films: Correlation between substrate stiffness and cell adhesion. Surface Science. Vol.570 p.142-154

[Fu98] Fuchs, E. and Cleveland D.W. (1998). A structural scaffolding of intermediate filaments in health and disease. Science. Vol.279. p.514-519

[Gab09] Gabriele, S., Benoliel, A.M., Bongrand, P. and Theodoly, O. (2009). Microfluidic Investigation reveals distinct roles of actin cytoskeleton and myosin II activity in capillary leukocyte trafficking. Biophysical Journal. Vol.96 p.4308-4318

[Gal08] Galli, M., Comely, K.S.C., Shean, T.A.V. and Oyen, M.L. (2008). Viscoelastic and poroelastic mechanical characterisation of hydrated gels. Journal of Materials Research. Vol.24/3 p.973-979

[Gas08] Gassmann P. and Haier, J. (2008). The tumor cell-host organ interface in the early onset of metastatic organ colonisation. Clin. Exp. Metastasis. Vol. 25 p.171-181

[Guc05] Guck, J., Schickinger, S., Lincoln, B., Wottawah, B., Ebert, S., Romeyke, M., Lenz, D., Erickson, H.M., Ananthakrishnan, R., Mitchell, D., Käs, J., Ulvick, S. and Bilby, C. (2005). Optical deformability as an inherent cell marker for testing malignent transformation and metastatic competence. Biophysical Journal. Vol.88 p.3689-3698

[Gui00] Guilak, F., Tedrow, J. R. and Burgkart, R. (2000). Viscoelastic properties of the nucleus. Biochemical and biophysical research communications. Vol.269 p.781-786

[Hei04] Heim, L.-O. (2004). Tilt of Atomic Force Microscope Cantilevers: Effect on Spring Constant and Adhesion Measuremts. Langmuir. Vol.20 p.2760-2764

[Her81] Hertz, H. (1881). Über die Berührung fester elastischer Körper. Journal für die reine und angewandte Mathematik. Vol.92 p.156-171

[Hoc00] Hochmuth, R.M. (2000). Micropipette aspiration of living cells. Journal of Biomechanics. Vol.33 p.15-22

[Hou09] Hou, H.W., Li, Q.S., Lee, G.Y.H., Kumar, A.P., Ong, C.N. and Lim, C.T. (2009). Deformability study of breast cancer cells using microfluidics. Biomedical Microdevices. Vol.11 p.557-564

[Huh05] Huh, D., Gu, W., Kamotani, Y., Grotberg, J.B. and Takayama, S. (2005). Microfluidics for flow cytometric analysis of cells and particles. Physiological Measurement. Vol.26 p.R73-R98

[Hut93] Hutter, J.L. and Bechhoefer J. (1993). Calibration of atomic force microscopy tips. Rev. Sci. Instrum. Vol.64(7) p.1868-1873

[Hut05] Hutter, J.L. (2005). Comment on tilt of Atomic Force Microscope cantilevers: Effect on spring constant and adhesion measuremts. Langmuir. Vol.21 p.2630-2632

[Jan91] Janmey, P.A., Euteneuer, U., Traub, P. and Schliwa, M. (1991). Viscoelastic properties of vimentin compared with other filamentous bioploymers. The Journal of Cell Biology. Vol.113 p.155-160

[Jea04] Jean, J.P., Gray, D.S., Spector, A.A. and Chen, C.S. (2004). Characterization of the Nuclear Deformation Caused by Changes in Endothelial Cell Shape. Journal of Biomechnaical Engineering. Vol.126 p.552-558

[Kas07] Kasza, K.E., Rowat, A. C., Liu, J., Angelini, T.E., Brangwynne, C. P., Koenderink, G. H. and Weitz, D. A. (2007). The cell as a material. Current Opinion in Cell Biology. Vol.19 p.101-107

[Kha09] Khanafer,K., Duprey, A., Schlicht, M.and Berguer, R. (2009). Effects of strain rate, mixing ratio, and stress-strain definition on the mechanical behavior of the polydimethylsiloxane (PDMS) material as related to its biological applications. Biomed. Microdevices. Vol.11 p.503-508

[Kim08] Kim, Y.C., Park, S.J. and Park, J.K. (2008). Biomechanical analysis of cancerous and normal cells based on bulge generation in a microfluidic device. Analyst. Vol. 133 p. 1432-1439

[Kre07] Kreplak, L. and Fudge, D. (2006). Biomechanical properties of intermediate filaments. BioEssays. Vol.29 p.26-35

[Kum09] Kumar, S. and Weaver, V. M. (2009) Mechanics, malignancy, and metastasis: The force journey of a tumor cell. Cancer Metastasis Rev. Vol.28 p.113-127

[Lan05] Landau,L.D. and Lifshitz, E.M. (2005). Theory of elasticity. Elsevier Butterworth-Heinemann.

[Lak99] Lakes, R.S. (1999). Viscoelastic Solids. CRC Press.

[Lev02] Levy, R. and Maaloum, M. (2002). Measuring the the spring constant of atomic force microscope cantilevers: thermal fluctuations and other methods. Nanotechnolgy. Vol.13 p.33-37

[Li08] Li, Q.S., Lee, G.Y.H., Ong, C.N. and Lim, C.T. (2008). AFM indentation study of breast cancer cells. Biochemical and Biophysical Research Communications. Vol.374 p.609-613

[Lie75] Lieber, M, Mazetta, J., Nelson-Rees, W., Kaplan, M. and Todaro, G. (1975). Establishment of a continous tumour-cell line (Panc-1) from a human carcinoma of the exocrine pancreas. International Journal of Cancer. Vol.15 p.741-747

[Liu08] Liu, Y. and Yang J. (2008). Coupling effects of refractive index discontinuity, spot size and spot location on the deflection sensitivity of optical-lever based atomic force microscopy. Nanotecnology. Vol.19 235501

[Lov07] Loverich, J., Kanno, I. and Kotera, A. (2007). Single-step replicable microfluidic check valve for rectifying and sensing low Reynolds number flow. Microfluid Nanofluid. Vol.3 p.427-435

[Mad97] Madou, M.J. (1997). Fundamentals in microfabrication. CRC Press

[Mag07] Magin, T.M., Vijayaraj, P. and Leube, R.E. (2007). Structural and regulatory functions of keratins. Experimental Cell Research. Vol.313 p.2021-2032

[Mat06] Mattice, J.M., Lau, A.G., Oyen, M.L. and Kent, R.W. (2006). Spherical indentation load-relaxation of soft biological tissues. Journal of Materials Research. Vol.21:8 p.2003-2010

[Mic04] Micoulet, A. (2004). Uniaxial Mechanical Assays on Adherent Living Single Cells: Animal Embryonic Fibroblast and Human Pancraes Cancer Cell. PhD Thesis, University of Heidelberg

[Mor05] Mortensen, N.A., Okkels, F. and Bruus, H. (2005). Reexamination of Hagen - Poiseuille flow: shape dependence of the hydraulic resistance in microchannels. Physical Review E, Vol.71 057301

[Oma04] Omary, M.B. and Coulombe, P.A. (Editors)(2004).Intermediate filament cytoskeleton. Methods in Cell Biology. Vol.78. Elsevier Academic Press

[Pad03] Padberg, B.C. und Schröder, S. (2003). Diagnostische Relevanz mehrkerniger Riesenzellen bei papillärem Schilddrüsenkarzinom. Der Phathologe. 24 S.382-386

[Paj07] Pajerowski, J.D., Dahl, K.N., Zong, F.L., Sammak, P.J. and Discher D.E. (2007). Physical plasticity of the nucleus in stem cell differentiation. PNAS. Vol.104:40 p.15619-15642

[Pro09] Proksch, R. Reference spring cantilever calibration technique with the MFP-3D AFM. www.asylumresarch.com (June 2009), support@asylumresearch.com

[Pro09b] Proksch, R. Thermal noise spring constant cantilever calibration technique with the MFP-3D AFM. www.asylumresearch.com (June 2009), support@asylumresearch.com

[Ros08] Rosenbluth, M. J., Crow, A., Sheavitz, J.W. and Fletcher, D. A. (2008). Slow stress propagation in adherent cells. Biophysical Journal. Vol.95 p.6052-6059

[Ros08b] Rosenbluth, M. J., Lam, W.A. and Fletcher, D. A. (2008). Analyzing cell mechanics in hematologic diseases with microfluidic biophysical flow cytometry. Lab on Chip. Vol.8 p.1062-1070

[Rot00] Rotsch, C. and Radmacher M. (2000). Drug-induced changes of cytoskeletal structure and mechanics in fibroblasts: An atomic force microscopy study. Biophysical Journal. Vol.78 p.520-535

[Rus04] Russel, D., Andrews, P. D., James, J. and Lane, E.B. (2004). Mechanical stress induces profound remodeling of keratin filaments and cell junctions in epidermolysis bullosa simplex keratinocytes. Journal of Cell Science. Vol.117 p.5233-5243

[Sem06] Semin,B., Guriyavona,S. and Bonaccuruso E. (2006). Nonconstant piezo velocity in highly dynamic atomic force spectroscopy. Review of Scientific Instruments. Vol.77.1161107

[Sia03] Sia, S.K. and Whitesides, G.M. (2003). Microfluidic devices fabricated in poly(dimethylsiloxane)for biological studies. Electrophoresis. Vol.24 p.3563-3576

[Siv08] Sivaramahkrishnan, S., DeGiulio, J.V., Lorand, L., Goldman, R.D. and Ridge, K.M. (2008). Micromechanical properties of keratin intermediate filament networks. PNAS. Vol.105(3) p.889-894

[Siv09] Sivaramahkrishnan, S. Schneider, J.L., Sitikov, A.,L., Goldman, R.D. and Ridge, K.M. (2009). Shear stress induced reorganisation of the keratin intermediate filament network requires phosphorylation by protein kinase C$zeta$. Molecular Biology of the Cell. Vol.20 p.2755-2765

[Sne65] Sneddon, I.N. (1965). The relation between load and penetration iin the axisymmetric boussinesq problem for a punch of arbitrary profile. International Journal of Engineering Science. Vol.3(1) p.47-57

[Squ05] Squires, T.M. and Quake, S.R. (2005). Microfluidics: Fluid physics at the nanoliter scale. Reviews of modern physics. Vol.77 p.977-1026

[Sta01] Stark R. W., Drobek, T. and Heckl, W.M. (2001). Thermomechanical noise of a free v-shaped cantilever. Ultramicroscopy. Vol.86 p.207-215

[Sur07] Suresh, S. (2007). Biomechanics and biophysics of cancer cells. Acta Biomaterialia. Vol.3 p.413-438

[Sur05] Suresh, S., Spatz, J., Mill, J.P., Micoulet, A., Dao, M., Lim, C.T., Beil, M and Seufferlein, T. (2005). Connections between single-cell biomechanics and human disease states: gastrointestinal cancer and malaria. Acta Biomaterialia. Vol.1 p.15-30

[Toi99] Toikka,G., Spinks, G.M. and Brown H.R. (1999). Interactions between micron-sized glass particles and Poly(dimethyl siloxane) in the absence and presence of applied load. Journal of Adhesion. Vol.74:1 p.317-340

[Tor96] Torii, A., Sasaki, M., Hane, K. and Okuma, S. (1996). A method for determining the spring constant of cantilevers for atomic force microscopy. Meas. Sci. Technol. Vol.7 p.179-184

[Tre07] Trepat, X., Deng,L., An, S.S., Navajas, D., Tschumperlin, D.J., Gerthoffer, W.T., Butler, J.P. and Fredberg, J.J. (2007). Universal physical responses to stretch in the living cell. Nature. Vol. 447. p. 592-595

[Van09] Vanapalli, S.A., Duits, M.H.G. and Mugele, F. (2009). Microfluidics as a functional tool for cell mechanics. Biomicrofluidics. Vol.3 012006

[VanL97] VanLandingham, M. (1997). The effect instrumental uncertainties on AFM indentation measurements. Microscopy Today. Vol. 97-10 p.12-15

[VanL97b] VanLandingham, M., McKnight, S.H., Palmese, G.R., Elings, J.R., Huang, X., Bogetti, T.A., Eduljee, R.F., Gillespie, Jr. J.W. (1997). Nanoscale indentation of polymer systems using the atomic force microscope. The Journal of Adhesion. Vol. 64:1 p.31-59

[VanV03] Van Vliet, K.J., Bao, G. and Suresh, S. (2003). The biomechanics toolbox: experimental approaches for living cells and biomolecules. Acta Biomateriala. Vol.51 p.5881-5905

[Vik92] Vikstrom, K.L., Lim, S.S., Goldman, R.D. and Borisy, G.G. (1992). Staedy state dynamics of intermediate filament networks. The Journal of Cell Biology. Vol.118(1) p.121-129

[Wan00] Wang, N. and Stamenovic, D. (2000). Contribution of intermediate filaments to cell stiffness, stiffening, and growth. AJP Cell Physiology. Vol.279 p. 188-194

[Win04] Windoffer, R., Wöll, S., Strnad, P. and Leube, ,R.E. (2004). Identification of novel principles of keratin filament network turnover in living cells. Molecular Biology of the Cell. Vol.15 p.2436-2448

[Woo97] Woodhouse, E.C., Chuaqui, R. F. and Liotta, L.A. (1997). General mechanisms of metastasis. Cancer Supplement.Vol.80:8 p.1529 - 1537

[Yam03] Yamada, S., Wirtz,D. and Coulombe, P.A. (2003). The mechanical properties of simple epithelial keratins 8 and 18: discriminating between interfacial and bulk elasticities. Journal of Structural Biology. Vol.105(4) p.1105-1106

Abbreviations and Symbols

AFM	Atomic Force Microscope, Atomic Force Microscopy
DI	deionized water
ESA	excess surface area
K8SE/K18WT	transfected cells/mutant (see section 2.2)
K8WT/K18WT	transfected cells/wildtype (see section 2.2)
PDMS	Polydimethylsiloxane
PBS	Phosphate Buffered Saline
PSD	Position Sensitive Diode
SD	Standard deviation
SE	Standard error
SEM	Scanning Electron Microscope
SPC	Sphingosylphosphorylcholin
STM	Scanning Tunneling Microscope
TLC	Thin Layer Corrected(model)

α	correction factor (see equation 4.4)
χ	(see equation 4.6)
η	viscosity
τ	characteristic time
a	contact radius
A	area
$A_{channel}$	channel cross section area
A_{def}	surface area after deformation
A_{max}	maximum surface area
A_{sph}	surface area of a sphere
$A_{sph,DI}$	surface area of a spherical cell in DI water
$A_{sph,N}$	surface area of a normal spherical cell
B	bending stiffness
D	deflection
D_{AFM}	AFM deformation
D_{cell}	cell diameter
D_{cyl}	cylinder diameter
D_{sph}	diameter of a sphere
$D_{sph,DI}$	diameter of a spherical cell in DI water
$D_{sph,N}$	diameter of a normal spherical cell

E	elastic modulus
E_0	instantanious elastic modulus
E_∞	equilibrium elastic modulus
E	dashpot associated elastic modulus
E_{Hertz}	Hertz elastic modulus
E_{TLC}	TLC elastic modulus
$E_{min,max}$	mininmum and maximum elastic modulus
F	force
F_{data}	force from data
F_{end}	point force at endloaded cantilever
F_{Hertz}	force used with Hertz model
F_{flap}	total force on flap
F_{flow}	force exerted by a fluid flow
$F_{friction}$	friction force
F_{mid}	point force at middle of cantilever
F_{model}	force used with certain model
F_{normal}	normal force
F_{TLC}	force used with TLC model
F_E	elastic fraction (see equation 4.10)
f	force per length
f_t	total flow rate
f_l	local flow rate
H	height
I	indentation depth
I_0	zero indentation depth, approach point
I_{max}	maximum indentation depth
I_a	area moment of inertia
K	cantilever spring constant
L	length
$L_{channel}$	channel length
$L_{approach}$	approach length (see figure 7.1)
M	torque
P_{flap}	total pressure on flap
p	pressure
r	residual
R	radius
R_C	radius of curvature
R_l	local hydrodynamic resistance
S	sensitivity
S_{corr}	corrected sensitivity
T	thickness
t	time
$\Delta t_{approach}$	(see figure 7.1)
$t_{arrival}$	(see figure 7.1)
t_{enter}	(see figure 7.1)
$\Delta t_{entrance}$	entrance time (see figure 7.1)
t_{exit}	(see figure 7.1)

$\Delta t_{transit}$	transit time (see figure 7.1)
U	deflection voltage
$v_{appraoch}$	cell approach velocity
v_l	local flow velocity
v_{mean}	mean velocity
$v_{sliding}$	mean sliding velocity
V	volume
V_{cub}	volume of a cuboid
V_{cyl}	volume of a cylinder
V_{def}	volume after deformation
V_{sph}	volume of a sphere
W	width
W_{cub}	width of cuboid cross section
Z	vertical movement (z-scanner)

Acknowledgements

First of all, I want to thank Prof. Joachim Spatz who supervised this thesis. He gave me the opportunity to work in a very exciting field of research and in an interdisciplinary group.

Prof. Heinz Horner took on the role of being the second referee of this thesis. I want to thank him for his interest and input in this work.

Prof. Thomas Seufferlein and Dr. Tobias Busch came up with the very interesting project of mechanical properties of the keratin network. Their scientific work, knowledge and input only made this project possible. I especially want to thank Dr. Tobias Busch for teaching me the cell handling and also for preparing numerous cell samples.

I want to thank Prof. Subra Suresh who gave me the great opportunity to work in his lab at MIT in Cambridge as a visting student for 1.5 years. During this stay, the work on the microfluidics progressed a lot as well as my knowledge on materials science. Further, I want to thank Dr. Alexandre Micoulet for help and supervision, and Dr. Ming Dao for interesting discussions. I want to thank all the Suresh group members for their help and support during my stay.

During the last two year of this thesis at the Max-Planck Institute for Metals Research in Stuttgart, numerous colleagues helped with their expertise in their field. I want to thank all of them, but only can name a few: Dr. Tobias Busch, Dr. Kristen Mills, Dr. Iain Dunlop, Linda Purwaningsih, Irina Slizskaia-Boxermann, Dr. Sarah Biela, Tobias Schön, Melih Kalafat, Dr. Stefan Kudera,.... The administrative staff, especially Elisabeth Pfeilmeier and Jutta Heß, were a great help with all the burocracy and organisational problems. Further, I want to thank all the technicians working in the group and especially Ioanis Grigoridis, Henriette Ries and Christine Mollenhauer. For the good atmosphere and the funny times, I thank my office mates, in particular my longterm office mates Dr. Letizia Carramusa and Dr. Eva Bock.

Further, I want to thank the people who helped shaping this thesis. Dr. Kristen Mills, Dr. Letizia Carramusa, Dr. Iain Dunlop, Dr. Tobias Busch, Dr. Alex de Beer and Dr. Stefan Kudera did not only proofread this thesis, but contributed with great ideas on the structuring of the contents and the language. Thanks a lot.

The final thanks is dedicated to my close friends and my family for ...everything.

Ich erläre hiermit, dass ich die vorgelegte Dissertation selbst verfasst und mich keiner anderen als der von mir ausdrücklich bezeichneten Quellen und Hilfen bedient habe.

Heidelberg, den 23.11.2009 .....

Nadine Walter